January 2021

Development Of Metal-Containing Nanoparticles For Chemical Analysis And Bioanalysis

Juan Han

DEVELOPMENT OF METAL-CONTAINING NANOPARTICLES FOR CHEMICAL ANALYSIS AND BIOANALYSIS

by

Juan Han
Master of Science, Northwest University, China, 2015
Bachelor of Science, Hainan University, China, 2011

A Dissertation

Submitted to the Graduate Faculty

of the

University of North Dakota

In partial fulfillment of the requirements

for the degree of

Doctor of Philosophy

Grand Forks, North Dakota
August
2021

Name: Juan Han

Degree: Doctor of Philosophy

This document, submitted in partial fulfillment of the requirements for the degree from the University of North Dakota, has been read by the Faculty Advisory Committee under whom the work has been done and is hereby approved.

DocuSigned by:
David Pierce
5A3AD8735A5C4F9...
David Pierce

DocuSigned by:
Julia Zhao
130DD6CE7E0643D...
Julia Xiaojun Zhao

DocuSigned by:
Alena Kubatova
273804AE0260441...
Alena Kubatova

DocuSigned by:
Guodong Du
0483C7B8D083424...
Guodong Du

DocuSigned by:
Feng Xiao
EC1B2A4CA9CF4CC...
Feng Xiao

This document is being submitted by the appointed advisory committee as having met all the requirements of the School of Graduate Studies at the University of North Dakota and is hereby approved.

DocuSigned by:
Chris Nelson
2E0AF088C733403...
Chris Nelson
Dean of the School of Graduate Studies

7/29/2021
Date

PERMISSION

Title Development of metal-containing nanoparticles for chemical analysis and bioanalysis

Department Chemistry

Degree Doctor of Philosophy

In presenting this document in partial fulfillment of the requirements for a graduate degree from the University of North Dakota, I agree that the library of this University shall make it freely available for inspection. I further agree that permission for extensive copying for scholarly purposes may be granted by the professor who supervised my dissertation work or, in her/his absence, by the Chairperson of the department or the Dean of the Graduate School. It is understood that any copying or publication or other use of this dissertation or part thereof for financial gain shall not be allowed without my written permission. It is also understood that due recognition shall be given to me and to the University of North Dakota in any scholarly use which may be made of any material in my dissertation.

Juan Han
August 2021

Abbreviations

AuNC	Gold nanocluster
AuNP	Gold nanoparticle
AgNP	Silver nanoparticle
APTES	(3-aminopropyl) triethoxysilane
CPN	Conjugated polymer nanoparticle
DLS	Dynamic light scattering
DSPE-PEG-NSH	1,2-distearoyl-sn-glycero-3-phosphoethanolamine conjugated polyethylene glycol with active succinimidyl ester
EDC	1-ethyl-3-(3-dimethylaminopropyl) carboddimide hydrochloride
FRET	Fluorescence resonance energy transfer
GSH	L-glutathione
HEPES	4-(2-hydroxyethyl)-1-piperazineethanesulfonic acid
KED	Kinetic energy discrimination

NSH	N-hydroxysuccinimide
NTA	Nanoparticle tracking analysis
MCP	Metal-containing nanoparticle
PEI	Polyethylenimine
PFO	Polydioctylfluorence
PVK	Poly(9-vinyllcarbazole)
PtNP	Platinum nanoparticle
Ru-SiO_2 NP	Tris(bipyridyl)ruthenium (II)-doped silica nanoparticle
SEM-EDS	Scanning electron microscope coupled with energy desperation spectroscopy
STDS	High sensitivity standard mode
TEM	Transmission electron microscope
TEOS	Tetraethyl orthosilicate
Triton X-100	Polyoxyethylene glycol tert-octylphenyl ether
spICP-MS	Single Particle inductively coupled plasma mass spectrometry

TABLE OF CONTENT

LIST OF FIGURES

Figure Page

LIST OF TABLES

Table Page

LIST OF SCHEMES

Scheme Page

ACKNOWLEDGEMENTS

I have received a lot of support from my advisors, committee members, labmates, faculty, and university financial support, as well as my friends and family in the past five years. Without their tremendous help, encouragement, and love, the journey to this place would not have been possible. At the very beginning of this dissertation, I would like to acknowledge their kindness to me during my Ph.D. program studies.

I would like to express my sincere gratitude to my supervisor, Dr. David T. Pierce for his invaluable advice, patient guidance, and tireless support during my Ph.D. studies. He not only taught me how to perform the scientific research with critical thinking in my research projects, but also provided suggestions on how to teach a laboratory course well as a teaching assistant at the university. I have received a great deal of support from Dr. Pierce and really appreciate everything he has done for me.

I would like to gratefully thank my co-advisor, Dr. Julia Xiaojun Zhao for her guidance and encouragement in both my research studies and personal life. She not only guides me in my adaptation to the American way of work and life, but also helps me to improve my presentation abilities. Many thanks are also given to my committee members: Dr. Alena Kubátová, Dr. Guodong Du, and Dr. Feng Xiao for their help during my graduate studies. Thank Dr. Alena Kubátová for giving me the opportunities to participate in the outreach activities for the local public schools and for providing assistance when I taught the Analytical Chemistry laboratory class. Thank you to Dr. Guodong Du for his

encouragement and understanding as he was always there to listen and to give advice. I would also like to thank Dr. Feng Xiao for his great help in my research and class.

I would like to extend thanks to the current and former members of Dr. David T. Pierce's research group and Dr. Julia Xiaojun Zhao's research group who were here throughout my Ph. D. program studies. They are Mr.Yuqiang Wang, Dr. Xu Wu, Dr. Yuqian Xing, Dr. Xiao Liu, Yingfen Wu, Wen Sun, Le Tang, Di Sun, Rachel Ross, and Sarah Reagen. I would like to send special thanks to my friends for their encouragement.

My gratitude extends to all the faculty members, staff, and graduate students in the Department of Chemistry at University of North Dakota for their great help. I would also like to thank the UND Graduate School for the tuition waiver and the Department of Chemistry for the teaching assistantships. Meanwhile, I appreciate the technical support from the Basic Science Imaging Center for training me on the microscopes and allowing me to use these instruments independently.

Finally, I would like to express my gratitude to my parents, my mother in-law, my father in-law, and my young son, Enoch, for enduring love, encouragement, and great support they provided which enable me to finish this work. Special thanks to my dear husband, Sai Wang. His love, patience, encouragement, and tolerance made me brave and give me confidence to move on and complete this work.

ABSTRACT

Metal-containing nanoparticles (MCPs) have been applied in fields ranging from environmental monitoring to biomedicine. This breadth is due to the outstanding behavior of MCPs as catalysts and imaging agents, and the ease with which nanoparticle morphology, composition, and reactivity (such as agglomeration) can be controlled. The work described in this dissertation will have two fundamentally different foci that are both essential for further development of MCPs as tools for chemical and bioanalysis. The first focus is on particle-by-particle characterization MCPs and the second focus is on creation of new composite MCPs. A total of four projects are included in this dissertation as follows.

The first project shows how to optimize a relatively new analysis method, single-particle inductively-coupled plasma mass spectrometry (spICP-MS), for the particle-by-particle characterization of MCPs. Bulk analysis methods such conventional ICP-MS produce an *aggregate* signal derived from many particles at once, whereas spICP-MS produces a discrete *per-particle* signal that is monitored over time to produce an ensemble of per-particle signals. Bulk analysis is very reliable for obtaining accurate *average* metal content per particle because the signal is inherently an average for many particles. However, all per-particle information is lost with bulk analysis methods. Conversely, spICP-MS provides a very rare window into the per-particle composition of MCPs; however, its method parameters such as particle concentration, ICP ionization efficiency, and dwell time must be carefully optimized for accurate per-particle analysis. This work demonstrates how

to optimize spICP-MSfor large MCPs—a particularly challenging size range—by using standard samples of gold nanoparticles ranging from 30 nm to 150 nm.

The second project uses properly optimized spICP-MS conditions to measure per-particle metal concentration of large-sized (> 100 nm) silica nanoparticles prepared by the water-in-oil microemulsion method and doped with tris(2,2'-bipyridyl)ruthenium(II). This is a well-studied MCP model that provides numerous avenues for bulk analysis (e.g., absorption spectrophotometry) and comparison with spICP-MS findings. Despite excellent correspondence of all methods for *average* Ru content over a wide range in doping levels, the per-particle doping level provided by spICP-MS does not—remarkably—adhere to a simple Gaussian-like distribution but shows a highly unusual geometric distribution. This result means, contrary to common assumption, the per-particle concentration of metal-dopant in silica nanoparticles prepared by the water-in-oil microemulsion method varies significantly per particle. These findings demonstrate that spICP-MS provides an essential per-particle window into MCP composition that is entirely missing with conventional bulk analysis methods. They also show that spICP-MS screening should become a routine characterization for new MCPs.

The third project shows how to prepare and apply a ratiometric and fluorescent MCP for the sensitive and selective *in vitro* imaging of copper ions (Cu^{2+}). This MCP contains conjugated polymer dots prepared from polydioctylfluorene (PFO), doped with a silica nanoparticle (PFO@SiO_2), and assembled with red emissive gold nanoclusters (AuNCs) at the PFO@SiO_2 surface to form a sandwich nanostructure, PFO@SiO_2@AuNCs. This nanostructure exhibits two fluorescence emission peaks associated with the PFO polymers (438 nm) and AuNCs (630 nm). When Cu^{2+} coordinates

with carboxyl groups on the AuNCs, the AuNC emission decreases in contrast to the constant PFO emission. This behavior provides a highly sensitive and selective ratiometric signal that can be applied for *in vitro* imaging and determination of Cu^{2+} in biological samples.

The fourth project develops a turn-off type fluorescence resonance energy transfer (FRET) method based on a MCP composite that is sensitive to cysteine. The composite consists of AuNCs conjugated with polyvinylcarbazole polymer nanoparticles (PVK PNs) that demonstrate a strong FRET between two distinct fluorescence emission peaks under excitation of 342 nm. The MCP composite is highly sensitive to cysteine concentration though a quenching process at 630 nm due to the decomposition of aurophilic bonds consisting of Au(I)-thiolate ligands under high pH value and the etching ability of cysteine toward gold atoms. The MCP composite shows potential for determination of other biomolecules.

CHAPTER I

INTRODUCTION OF METAL-CONTAINING NANOPARTICLES

1.1. Significance of Metal-Containing Nanoparticles

Nanomaterials have at least one dimension between 1 to 100 nm.[1] Generally, nanomaterials can be classified into different groups based on various criteria. Besides their dimensionality, their overall shape, and their chemical composition, among the zero-dimension nanomaterials with spherical shape, nanomaterials can be further categorized into metal-containing nanoparticles and nonmetal-containing nanoparticles. The metal-containing nanoparticles (MCPs) studied or developed for this dissertation comprise a metal nanocluster and its composite, various metallic nanoparticles, and a metal-doped nanoparticle. However, this is small subset of MCPs compared to the numerous types developed in many different areas of research over the past decade and that are still garnering attention at the scientific and commercial level. Compared with a bulk metallic material, MCPs with same metallic composition show unique size-dependent characteristics and have valuable physicochemical characteristics, including excellent electronic properties, high mechanical and thermal stability, good magnetic properties, large surface area, and distinctive optical properties.[2] These enhanced properties have enabled MCPs to be used in different fields including agriculture,[3, 4] industry,[5, 6] and environment.[7, 8] Furthermore, MCPs have been applied in areas of health and medicine such as drug delivery,[9] gene delivery,[10] anticancer activity,[11] bioimaging,[12] biosensing,[13] and tissue engineering.[14] The development of MCPs has made a revolutionary impact in every aspect of human life.

With the demand for these MCPs expanding rapidly, many different types of MCPs

have proposed and developed in both industrial and academic venues. This list introduces the different types of MCPs that are the focus of this dissertation:

1) *Metal nanoclusters and their composites*. Metal nanoclusters have the small size of around 2 nm that typically distinguished them from nanoparticles.[15] Their interesting quantum confinement effects result from a more discrete electronic structure than larger nanomaterials. These effects produce useful molecular-like photophysical and photochemical properties such as strong luminescence and photothermal convention.[16, 17] Metal nanoclusters of gold (AuNC), silver (AgNC), copper (CuNC), and palladium (PdNC), as well as their composites have becoming promising materials as both catalysts for reactions and the signaling agent in sensors.[18-20]

2) *Metallic nanoparticles*. Metallic nanoparticles are nanoscale materials composed of one component that either an elemental metal or a metal oxide. They have unique optical properties and exhibit advantage of high surface area.[21, 22] Elemental metallic nanoparticles, such as gold (AuNP) and silver (AgNP), as well as metal oxide nanoparticles of titanium dioxide (TiO_2NP) are often used in the optical devices and catalytic reactions.[23, 24]

3) *Metal-doped nanoparticles*. These MCPs are inherently multicomponent and are usually composed of a metal oxide matrix as the major component along with a minor amount of some type of metal compound that is intercalated or otherwise 'doped' into the metal oxide matrix. Because the metal oxide provides a scaffolding that can be easily modified with covalent reagents and the metal dopant serves as an optically- or magnetically-active modifier that can be easily interchanged, this type of MCP offers a great deal of synthetic flexibility and the ability to tune the nanomaterial for specific tasks. For example, zinc oxide nanoparticles doped with cobalt have been used to enhance

biomedical and energy applications and silica nanoparticles doped with the well-known chromophore and lumiphore, tris(2,2'-bipyridyl)ruthenium(II) (Ru-SiO_2 NP), have been applied widely in fields of drug delivery, bioimaging, biosensing, and catalysis.[25-29]

1.2. Synthesis of Metal-Containing Nanoparticles

Many strategies, which range from chemical methods to physical approaches, have been developed to prepare the MCPs. In general, these approaches can be classified as either top-down and bottom-up approaches. In the top-down methods, different techniques such as laser ablation[30-32] and ultrasound radiation[33, 34] are used to control the size of MCPs until the desired morphological and dimensional aspects are achieved from the bulk material. In the bottom-up approach, chemical or biological agents are applied to reduce metal salts and stabilize the metal atoms to form the desired MCPs. There are merits and deficiencies to both kinds of synthetic approaches. For instance, toxic solvents and low cost are common features of the bottom-up methods,[35, 36] while the top-down methods are often easier to control and offer high reproducibility but require expensive instruments.[37, 38]

1.3. Characterization of Metal-Containing Nanoparticles

The MCPs have many measurable characteristics, such as optical, electronic, and thermal properties, which differ considerably from those of the bulk metallic materials. To evaluate the synthesis of the MCPs and their suitability for applications in various fields, many well-developed and validated analytical techniques have been adapted to characterize the chemical and physical properties of the MCPs. For example, the morphology (i.e., shape and size) of MCPs is usually studied using the electron microscope,[39] the hydrodynamic size and number concentration measurements of the

MCPs is determined by light scattering,[40] the chemical composition and quantification of the *average* metal mass concentration of the MCPs is often analyzed by atomic spectrometry.[41] The physical and chemical properties of the MCPs that are most useful to know and are often the focus of MCP characterization include composition, size, shape, agglomeration/aggregation state, surface area, size distribution (i.e., how size varies across a large number of NPs), stability, surface chemistry, and surface roughness.[42, 43] Development of new and better methods for the characterization of MCPs plays very important role in the knowledge and development of MCPs.

1.4. Challenges in Studies of Metal-Containing Nanoparticles

Further development of MCPs requires advancement in both their characterization and their application. Among the characterization methods currently used for MCPs, bulk analysis methods such as conventional inductively-coupled plasma mass spectrometry (ICP-MS) and various forms of molecular spectrophotometry (e.g., absorbance and fluorescence) are by far the most common. They have been well-developed to characterize the chemical and physical properties of MCPs and they have been commercially available for decades. However, characterization of MCPs with bulk analysis methods only provides information about average composition and it cannot provide per-particle information. These methods also have limitations in the measurement of potentially complex sample matrices under environmental condition/biological system. To better understand the composition MCPs down to the particle level, better particle-by-particle characterization methods need to be developed. This is especially true for MCPs near the nanoparticle size limits of very small (ca. 1 nm) and very large (ca. 100 nm).

Application is another area driving the development of nanoclusters. Because of

their unique optical and electronic properties, nanoclusters are among the most promising new MCPs for use analysis applications. However, low quantum yield of nanoclusters is a present barrier to their wider application and more development work is clearly needed to take full advantage of their unique behavior.

1.5. Goals of This Dissertation

The work described in this dissertation addresses two main goals. One goal is to improve the single particle analysis of MCPs by using ICP-MS and thereby provide the better particle-level information that can be used to aid the synthesis and application of these materials. This goal is addressed in separate projects described in Chapters 1 and 2. The other goal is to develop better gold nanocluster MCPs and to explore their applications for biosensing and bioimaging. This goal is addressed in separate projects described in Chapters 4 and 5.

The first goal addressed in this dissertation—improving the particle-by-particle characterization of MCPs—utilizes a relatively new method called single-particle ICP-MS (spICP-MS). Chapter 2 is focused on optimizing the operating conditions of spICP-MS, such as dwell time and particle concentration, using gold nanoparticle standards over a wide size range. Chapter 3 is focused on using optimum spICP-MS conditions to characterize metal content of ruthenium-doped silica nanoparticles (Ru-SiO_2 NPs)—a challenging MCP material because of its multicomponent composition.

The second goal addressed in this dissertation—exploring new applications of MCPs—utilizes gold nanoclusters to improve sensitivity for analytes in biological systems. Chapter 4 describes the development of a new sandwich structured ratiometric nanoprobe for accurate and sensitive determination of copper ions and in *vitro* imaging. Chapter 5

describes the development of a new FRET-based ratiometric nanohybrid that enhances the quantum yield of the integrated gold nanoclusters for biomolecule detection.

CHAPTER II

OPTIMIZATION OF SINGLE-PARTICLE ICP-MS AND THE INFLUENCE OF PARTICLE SIZE

2.1. Introduction

The use of metallic nanoparticles has greatly expanded over the last decade in research fields as diverse as catalysis,[44, 45] energy,[46, 47] biology and medicine.[48-50] Much of this expansion is due to their ease of synthesis and functionalization, excellent stability, and good biocompatibility.[51-53] However, the increased use of metallic nanoparticles, especially in consumer products, has also raised concerns about their potential impact on human health and the environment.[54-56] In this regard, it is essential to develop a diverse and robust array of methods to analyze samples containing metallic nanoparticles at environmental concentration. Techniques typically used for metallic colloid nanoparticle characterization such as transmission electron microscopy (TEM),[57] dynamic light scattering (DLS),[58] nanoparticle tracking analysis (NTA),[59] and UV-vis spectroscopy,[57, 58, 60] provide a wealth of information but also suffer from limitations that include drying artifacts, long analysis time period, poor selectivity, and low sensitivity.[59, 61, 62] Moreover, most of these methods only provide *average* properties of the individual nanoparticles contained in the sample and can miss important characteristics or differences at the particle level.

As an emerging analytical technique, single particle inductively-coupled plasma mass spectrometry (spICP-MS) provides valuable merits of high sensitivity and excellent selectivity which make it a promising and maturing method for the rapid quantitative analysis of individual metal-containing nanoparticles (MCPs). Compared to conventional ICP-MS of ionic metal solutions, the single-particle method requires a much shorter

measurement cycle (ms versus s) and a much lower analyte concentration (< 10^8 nanoparticles/L versus > 10^{13} metal ions/L). The low NP concentration improves the likelihood that only one MCP will enter the plasma during the shortened measurement cycle, and the short measurement cycle allows the mass spectrometer to accurately quantify the discrete pulse of a target isotope (in units of counts) generated from the atomization of a single nanoparticle by the plasma.[62-64] Metals are most commonly used as the target isotopes for both sp- and conventional ICP-MS because of their lower ionization energy (compared to most non-metals or metalloids) which usually results in higher sensitivity.[65-67]

To date, spICP-MS has been used most often to measure the concentration individual MCPs based on the number of discrete pulses of the target metal isotope detected relative to the volume of analyte solution entering the plasma. Recent examples of particle concentration analysis include environmental samples to study the fate of metallic nanoparticles from commercial products[68-71] and expanding application in bio-labeling assays.[72-74] A much more challenging spICP-MS analysis is determination of the amount of metal contained within individual metallic nanoparticle, which in-turn provides individual particle size if the particle shape and component density are known. Such analysis requires a calibration to convert the discrete pulse of target isotope (in units of counts per NP) into the number of metal atoms per NP. The metallic nanoparticles (primarily Au and Ag) are most often characterized in this manner because their size and density are well-defined.[62, 75, 76] Accuracy of the isotope pulse calibration cannot be overstated for this type of analysis and a number of method factors, including the efficiencies of particle introduction and ionization by the ICP, dwell time (the millisecond

time period over which counts are integrated for a single MS reading), and introduced particle number concentration must be carefully considered during method validation.[64, 77-80]

So far, spICP-MS has only been used to measure metal concentration within of individual MCPs smaller than 100 nm.[77, 81, 82] The work presented in this chapter provides an assessment whether accurate per-particle analysis can be extended to the challenging large size range (> 100 nm) by optimization of measurement parameters. Gold nanoparticles (AuNPs) were selected for this assessment to simplify the analysis challenge and to take advantage of the ready availability of different particle sizes with consistent geometrical characteristics. To assess the accuracy of quantitation, several affecting parameters including particle number concentration, particle ionization efficiency, and dwell time (integration period) were studied in in-depth across a broad size range (30 – 150 nm diameter) and optimized based on standard protocols and methods. Finally, the spICP-MS results acquired with optimized parameters were compared with analysis results obtained using the bulk method of conventional ICP-MS and the single particle analysis of TEM.

2.2. Experimental Section

2.2.1. Materials

Stock standard solutions of gold nanoparticles suspended in purified water and with diameters of 30 nm (AuNP-30), 60 nm (AuNP-60), and 150 nm (AuNP-150) were obtained from BBI Solutions (Crumlin, UK) and Nanopartz (Loveland, CO, USA). Stock standard solutions of 100 mg/L ionic gold in nitric acid was purchased from Inorganic Ventures (Christiansburg, VA, USA) and used to make working standards between 0.1–

10.0 µg/L (serial dilution with 2 % nitric acid) for ICP-MS calibration. Optima grade nitric acid purchased from VWR (Radnor, PA, USA) and ultrapure (type 1, 18.2 MΩ·cm) reagent water from a Millipore Synergy (Burlington, MA, USA) purification system were used to prepare all ICP-MS solutions and for all analysis work. Gases used for ICP-MS operation included Grade 4.8 liquid argon used for plasma and nebulizer operation and Grade 5 helium used as an inert collision gas for kinetic energy discrimination (KED).

2.2.2. Instruments

All ICP-MS measurements were performed with a Thermo Scientific iCAP Qc inductively coupled plasma mass spectrometer (Waltham, MA, USA) controlled by Qtegra^{TM} software (version 2.8.2944.202). This instrument was equipped with a 4-channel 12-roller peristaltic pump, nickel sample and skimmer cones, a Teledyne CETAC ASX560 autosampler, a microflow perfluoroalkoxy nebulizer, and a Peltier-cooled quartz cyclonic spray chamber. The instrument was tuned daily with THERMO-4AREV for a maximum ^{59}Co, ^{238}U and minimum $^{140}Ce^{16}O/^{140}Ce$ oxide signals. A Hitachi 7500 transmission electron microscope (Tokyo, Japan) was used to obtain TEM images of AuNPs. A Zetasizer Nano (Malvern Panalytical, UK) was applied for the measurement of Zeta potential of AuNPs. Measurement processing and graphing was performed using Microsoft Excel, or OriginPro Lab (Northampton, MA, USA).

2.2.3. Concentration units and conventions used for nanoparticle solutions

Two concentration units were used routinely for characterization of AuNP solutions. These included particle number concentration (P, number of nanoparticles per liter, NP/L) and mass concentration (C_i, mass of metal per liter, µg/L). These concentrations units are related by the nanoparticle size, geometry and composition. For the spherical gold

nanoparticles used in this work, particle number concentration can be converted to mass concentration using the TEM-measured radius (R, cm) and assumed gold density (ρ, 19.3 g/cm^3), as shown in Eq. 2-1.

$$C_i = P \times \frac{4}{3}\pi R^3 \times \rho \times 10^6 \quad (2\text{-}1)$$

The usual convention adopted throughout this work was to use mass concentrations for ionic gold solutions and number concentration for solutions containing whole AuNPs. However, two specific situations favored use of the opposite conventions: (i) Number concentrations were used for solutions of digested AuNPs that contained ionic gold. (ii) Mass concentrations were used for solutions of whole AuNP in conventional ICP-MS measurements of particle ionization efficiency.

2.2.4. Measurement of *average* number of Au atoms per NP

Transmission Electronic Microscope. Samples were prepared for TEM analysis according the generic protocol of the UK National Physical Laboratory.[83] Specifically, AuNP samples were diluted with ultrapure water to a concentration of 1.0×10^9 NP/L and, to prevent the aggregation of AuNPs, the solution was sonicated for 2 min in a bath before depositing a 3.0 µL aliquot onto the surface of a copper TEM grid. The TEM samples were dried in the air for 24 h prior to analysis. The obtained TEM images were processed with Image J software to measure the size of individual AuNPs. A number of Au atoms per NP was calculated (Eq. 2-2) by using the TEM-measured radius, assumed gold density, gold molecular mass (M, 197 g/mol) and Avogadro's number (N_A).

$$N_P = \frac{4}{3}\pi R^3 \times \frac{\rho}{M} \times N_A \quad (2\text{-}2)$$

An *average* number of Au atoms per NP ($\overline{N_P}$) was then determined by averaging numbers obtained from the measurement of 200 individual AuNPs, as shown in Eq. 2-3.

$$\overline{N_P} = \frac{\sum_{i=1}^{200} N_P}{200} \quad (2\text{-}3)$$

Conventional ICP-MS. Instrument operating conditions are listed in Table 2.1. All other instrument parameters were optimized to meet requirements as defined by the manufacturer prior to method calibration and analysis. Calibration and quality-control procedures typically followed EPA method 200.8 (Revision 5.4). Sample analysis was performed in KED mode for all experiments. Solutions containing 1.0 µg/L digested AuNPs in 2 % nitric acid and 10.0 µg/L of Ge and Bi internal standard were combined from separate pump channels and introduced together to the ICP-MS nebulizer. The target isotope, ^{197}Au, was monitored relative to the internal standards (^{74}Ge and ^{209}Bi) and its signal was calibrated using 0.02, 0.1, 1.0, and 10.0 µg/L of ionic Au standards in 2 % nitric acid. Because a long dwell time and a high number of averaged sweeps were used in the conventional ICP-MS configuration (Table 2.1), the concentration determined for the AuNP samples corresponded to a bulk concentration of Au averaged over a large volume of solution. The *average* number of Au atoms per NP ($\overline{N}_P$) was determined by solving for a concentration of AuNPs (C_i, µg/L), multiplying by Avogadro's number (N_A), and dividing by the particle number concentration of the AuNP solution and gold molecular mass (M).

$$\overline{N}_P = \frac{N_A \times C_i}{P \times M \times 10^6} \quad (2\text{-}4)$$

Table 2.1. ICP-MS operating conditions used for conventional and single-particle measurements.

Parameter	Conventional measurement	Single-particle measurement
Sample introduction		
peristaltic pump	4-channel, 12-roller	4-channel, 12-roller
pump speed (rpm)	20	20
sample tubing (mm ID)	0.508	0.508
internal-standard tubing (mm ID)	0.508	not used
waste tubing (mm ID)	1.295	1.295
nebulizer	Microflow PFA-ST	Microflow PFA-ST
nebulizer gas flow (L/min)	1.09	1.05
spray chamber	quartz cyclonic	quartz cyclonic
spray chamber temperature (℃)	2.70	2.70
Plasma		
torch	ICAP Q quartz	ICAP Q quartz
Rf power (W)	1550	1550
coolant gas flow (L/min)	14	14
plasma gas flow (L/min)	0.8	0.8
sample injector	quartz (2.5 mm ID)	quartz (2.5 mm ID)
Mass spectrometer		
sample cone	nickel	nickel
skimmer cone	nickel	nickel
cone insert	3.5 mm	2.8 mm
mode	KED	STDS
KED gas flow (mL/min)	4.6	0
dwell Time (ms)	50	5, 10, 20, and 50
sweeps	10	0
internal standards	^{74}Ge, ^{209}Bi	none

spICP-MS. Instrument operating conditions are listed and compared to conventional ICP-MS conditions in Table 2.1. A conversion to high-sensitivity standard mode (STDS) was required for single-particle measurements with a physical replacement of the cone separator insert and sample probe. All other instrument parameters were optimized to meet requirements as defined by the manufacturer prior to method calibration and analysis. Calibration and quality-control steps typically followed the RIKILT Standard Operating Procedure for counting and sizing of nanoparticles.[84] Time-resolved data acquisition, which included signal calibration, was controlled using the Qtegra™ software plug-in (version 2.8.2944.202). Varied sizes of AuNPs, including 30, 60, and 150 nm, were serially diluted with high purity water to 5.00×10^7, 2.50×10^7, 1.25×10^7, and 5.00×10^6 NP/L. Target ^{197}Au isotope counts were monitored, and a series of ionic Au calibration standards 0.1 to 10.0 µg/L were measured to allow conversion of counts per NP (I_P) to a number of Au atoms per NP (N_P).

To obtain this conversion, the measured counts per dwell time (I) for each ionic metal standard solution were averaged over the entire sampling interval ($\bar{I}$) and Eq. 2-5 was used to transform the solution mass concentration (C_i, µg/L) to a mass of metal reaching the plasma per dwell time (W, µg) with parameters of sample flow rate (u, 0.2 mL/min) and transport efficiency (η_n, see section 2.2.5 below).[64]

$$W = \eta_n \times u \times t_{dwell} \times C_i \tag{2-5}$$

The calibration equation of $\bar{I}$ versus W (with slope m and y-intercept $b_{\text{forced}} = 0$) yielded an expression for mass of metal per NP (W_P, µg) when the isotope count per NP (I_P) occurred within one dwell time and the particle ionization efficiency (η_i, see section 2.2.6 below) was known (Eq. 2-6).[64]

$$W_P = \frac{I_P}{m \times \eta_i} \quad (2\text{-}6)$$

To prevent the false conversion of instrument noise to metal concentrations, only counts greater than a discrete noise threshold (see section 2.2.7 below) were considered NP events. Finally, the number of Au atoms per NP (N_P) was obtained using the molecular weight of the metal (M) and Avogadro constant (N_A) as shown in Eq. 2-7.[64]

$$N_P = \frac{W_P}{M} \times 10^{-6} \times N_A \quad (2\text{-}7)$$

To compare the N_p results of per-particle measurements with the $\overline{N}_P$ results of bulk measurements (TEM and conventional ICP-MS), the n measurements of N_P over one sampling interval were averaged as shown in Eq. 2-8.

$$\overline{N}_P = \frac{\sum_{i=1}^{n} N_P}{n} \quad (2\text{-}8)$$

2.2.5. Measurement of transport efficiency

Transport efficiency is defined as the amount of analyte entering the plasma relative to the amount of analyte delivered to the nebulizer and spray chamber within a defined measurement period. Only a small fraction of liquid sample pumped into the ICP-MS nebulizer enters the plasma because all large microdroplets formed by the nebulizer collide with the walls of the spray chamber and are carried away as waste. Transport efficiencies for AuNP solutions of known number concentration were determined using the particle number method. Here, the number of AuNPs counted by spICP-MS within a certain sampling period is divided by the number of particles contained within the sampled volume of solution and multiplied by 100.[64] A long dwell time of 50 ms and a low particle number concentration of 5.00×10^6 NP/L was used for all transfer efficiency determinations in this work so particle counting errors due to split- and multiple-particle measurements were

minimized. No significant difference was found between the transport efficiencies determined for 30 nm, 60 nm, and 150 nm AuNPs so an averaged value of 8.9 % ± 0.1 % was used for all samples.

2.2.6. Measurement of particle ionization efficiency

Consistent with literature procedures, particle ionization efficiency ($\eta_{i,}$) was measured for all nanoparticle sizes with the ICP-MS instrument operating in conventional mode rather that single-particle mode.[64] An aliquot of 0.5 mL of 50.0 mg/L AuNPs of 30 nm, 60 nm, and 150 nm was digested overnight at room temperature using a 2.0 mL aliquot of aqua regia solution in order completely oxidize and dissolve the AuNPs to ionic Au. Both the individual and digested AuNPs of 30 nm, 60 nm, and 150 nm were diluted to 5×10^7 NP/L and transported into spICP-MS to verify the digestion degree. An aliquot of 10.0 mL of 1.0 μg/L digested and undigested AuNPs were introduced into a conventional ICP-MS, respectively. The ionization efficiency was obtained by using the intensity of undigested AuNPs divided by the intensity of digested AuNPs and multiplying to 100. Ionization efficiencies used for AuNPs in all spICP-MS measurements was 80 % ± 4 %, 76 % ± 5 %, and 65 % ± 2 % corresponding to 30 nm, 60 nm, and 150 nm, respectively.

2.2.7. Number distribution histograms

Because the ^{197}Au counts measured over most dwell times by spICP-MS remain at background levels and do not contain information about AuNPs in the sample, it is more convenient to view these data sets as a number distribution histogram. Using OriginPro Lab, the number of times that ^{197}Au counts per dwell time (I_p in equations above) fall within discreet histogram intervals (usually 5 counts in width and called the histogram bin size) can be readily determined and then plotted as histogram distribution with the number

signals measured for each interval on the y-axis and the initial ^{197}Au signal of the interval on the x-axis. Data presented as these number distribution histograms were often processed further to show number distributions versus mass of metal (W_p using Eq. 2-6) or number of metal atoms (N_p using Eq. 2-7). Moreover, ^{197}Au signal intervals were usually sorted by discrete thresholds to distinguish background detector noise from signals caused by nanoparticles, and also to distinguish signals caused by split-, whole-, and multiple-particles (see section 2.2.8 for a description of these signal thresholds).

2.2.8. Thresholds used for counting nanoparticles

Nanoparticle threshold. The electron multiplier used as the mass spectrometer detector in ICP-MS produces a background shot-noise signal (in counts per dwell time) that combines with any signal generated by the target isotope. A threshold criterion used to distinguish a nanoparticle signal from the shot-noise background (Eq. 2-9) was developed from the shot-noise signal average ($\bar{I}_{blank}$) and standard deviation (σ_{blank}) that was measured for a blank solution. Signals that exceeded this threshold were considered the result of either a split, whole or multiple nanoparticles.

$$\text{Nanoparticle threshold} > \bar{I}_{blank} + 5 \times \sigma_{blank} \tag{2-9}$$

Split- and multiple-particle thresholds. Because nanoparticles enter the plasma in a random manner, there is some finite chance that the signal generated by a single particle is split between two successive dwell-time measurements. This means the signal of one dwell-time measurement is much lower than for one particle (henceforward called a split-particle event). There is also some finite chance that two or more particles enter the plasma simultaneously so the signal of one dwell-time measurement is much higher than for one particle (henceforward called a multiple-particle event). These events can be minimized by

changing dwell time and nanoparticle concentration, but optimization of these conditions requires an objective signal threshold for each type of event. The thresholds applied in this work were based on a Gaussian analysis of the number distribution of nanoparticle signals derived from a spICP-MS data set (see section 2.2.7 for a description of this number distribution). The number distribution was fit with a Gaussian distribution formula to determine a Gaussian mean ($\bar{G}$) and standard deviation (σ_G). Whole, single nanoparticles were assumed to have signals within three standard deviations of the mean ($\bar{G} \pm 3 \times \sigma_G$), split-particle events were assumed to have signals below $\bar{G} - 3 \times \sigma_G$ (Eq. 2-10), and multiple-particle events were assumed to have signals above $\bar{G} + 3 \times \sigma_G$ (Eq. 2-11).

$$\text{Split-particle threshold} < \bar{G} - 3 \times \sigma_G \tag{2-10}$$

$$\text{Multiple-particle threshold} > \bar{G} + 3 \times \sigma_G \tag{2-11}$$

To more easily compare the number of split- and multiple-particle events when optimizing for spICP-MS conditions, each was converted to a percentage by dividing with the total number of nanoparticles detected (based on Eq. 2-9) and multiplying by 100.

2.3. Results and Discussion

2.3.1. Design of MCPs analysis by spICP-MS

To demonstrate the procedure and data processing used for single particle analysis by spICP-MS, a stepwise example is provided in Scheme 2.1. This example was performed with the ICP-MS in single-particle mode (Table 2.1) with a 10 ms dwell time and a sample of 30 nm of AuNPs at a concentration of 2.50×10^7 NP/L. Final results of the analysis include the number of metal atoms for well over 10^4 individual NPs (N_P) and the *average* number of metal atoms per NP ($\overline{N}_P$) for this ensemble. The five fundamental steps of the process are listed below and will be described in detail.

1. Analyze ionic gold standards to calibrate ^{197}Au counts with the amount of gold entering the plasma per dwell time (Scheme 2.1A and 2.1B).

2. Analyze a AuNP solution to acquire ^{197}Au counts for individual NPs over a three-minute sampling period (Scheme 2.1C) and generate a number distribution plot of ^{197}Au counts per NP (Scheme 2.1D).

3. Convert the ^{197}Au counts per NP to Au mass per NP using the calibration provided by ionic gold standards (Scheme 2.1E).

4. Convert Au mass to number of Au atoms per NP (N_P, Scheme 2.1F).

5. Calculate the *average* number of Au atoms per NP ($\bar{N}_P$) for the entire ensemble of sampled NPs.

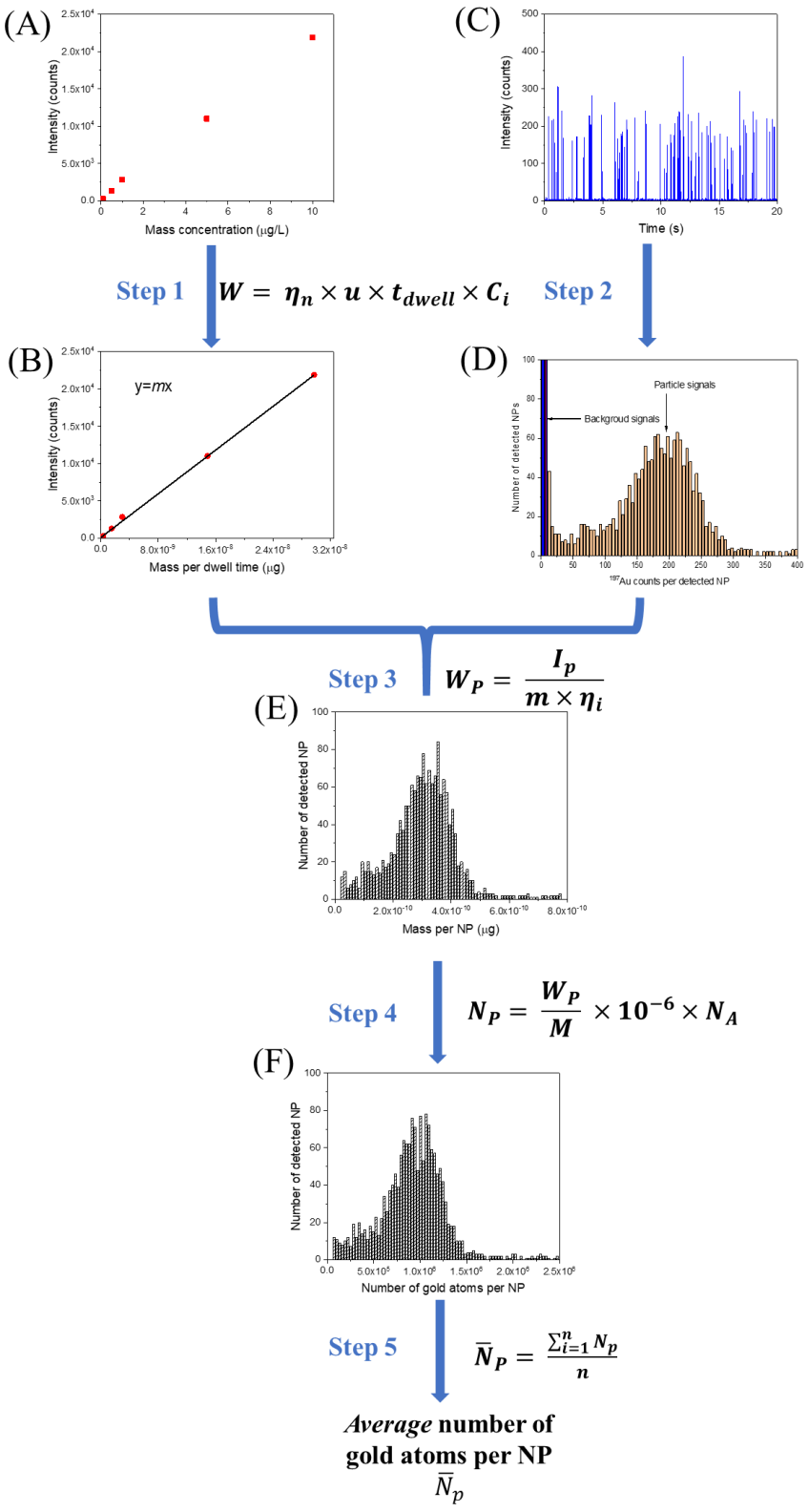

Scheme 2.1. Data process illustration of 30 nm AuNPs with spICP-MS measurement to obtain the *average* number of Au atoms per NP.

Step 1. Before analyzing a AuNP solution, a series of ionic gold standards are introduced and the average ^{197}Au counts per dwell time ($\bar{I}$) must demonstrate direct proportionality to the solution concentration in μg/L (Scheme 2.1A). This proportional concentration is then converted to the mass of Au entering the plasma per dwell time in units of μg (Eq. 2-5) by knowing the nebulizer transfer efficiency (η_n) and flow rate of solution (u), which in this work were 8.9 % and 0.2 mL/min, respectively. The resulting plot (Scheme 2.1B) serves as a calibration of measured ^{197}Au counts to mass of Au entering the plasma per dwell time and is needed to process data obtained with AuNP solutions.

Step 2. A partial spICP-MS data set for 30 nm AuNPs is shown in Scheme 2.1C. The ^{197}Au counts per dwell time remain close to zero for most readings but occasionally and randomly increase (to ca. 200 counts) when a AuNP enters the plasma. Critical assumptions used in this analysis are that ^{197}Au counts for each AuNP occur entirely within one dwell time (i.e., a signal is not split between successive dwell times) and ^{197}Au counts correspond to only one AuNP (i.e., a signal is not generated from multiple particles). Validity of these assumptions and conditions that favor them will be discussed in Section 2.3.3. Because the ^{197}Au counts measured over most dwell times remain at background levels and do not contain information about AuNPs in the sample, it is more convenient to view these data sets as a number distribution plot. Using OriginPro Lab, the number of times that ^{197}Au counts per dwell time fall within a discreet interval can be readily calculated and plotted (Scheme 2.1D). The highest numbers are observed for the lowest ^{197}Au counts per dwell time because these represent background readings. Readings corresponding to individual AuNPs have ^{197}Au counts per dwell time that are significantly higher than background levels, which is usually evaluated as greater that five-times the

measured standard deviation of a blank solution (Eq 2-9). Moreover, these readings show a Gaussian-like distribution centered near 200 ^{197}Au counts per dwell time.

Steps 3. Using the signal calibration obtained Step 1, ^{197}Au counts per dwell time are converted to mass of Au per NP (Eq. 2-6 and Scheme 2.1E). An important factor in this conversion is the particle ionization efficiency (η_i), which indicates how completely the AuNP is atomized and then ionized during the short time it spends within the torch plasma. NP material and size both have an influence on this efficiency. For the 30 nm AuNPs used in this example, the particle ionization efficiency is 81 % ± 5 %.

Steps 4 and 5. Finally, mass per NP is converted to number of Au atoms per NP (N_P, Eq. 2-7 and Scheme 2.1D) and the *average* number of Au atoms per NP is calculated ($\overline{N}_P$, Eq. 2-8) for the entire ensemble of sampled NPs.

2.3.2. Characterization of AuNPs with TEM and Zeta Potential

Figure 2.1(A-C) shows AuNPs of various sizes homogeneously distributed on the surface of copper grid and characterized by TEM. A great majority of the monodispersed AuNPs were spherical in shape with measured sizes of 31 ± 2 nm (AuNP-30), 54 ± 4 nm (AuNP-60), and 125 ± 9 nm (AuNP-150) (Figure 2.1D), although a small percentage of the AuNPs had irregular shapes. These AuNPs had dumbbell or hexagon shapes (Figure 2.2). Zeta potentials of theses AuNP-30, AuNP-60, and AuNP-150 samples were also measured in phosphate buffered saline solution (10 mM, pH=7.4) and found to be -31 ± 1 mV, -27 ± 2 mV, and -30 ± 1.0 mV, respectively. Such negative values favor a high degree of polydispersion in solution and very little (if any) aggregation.

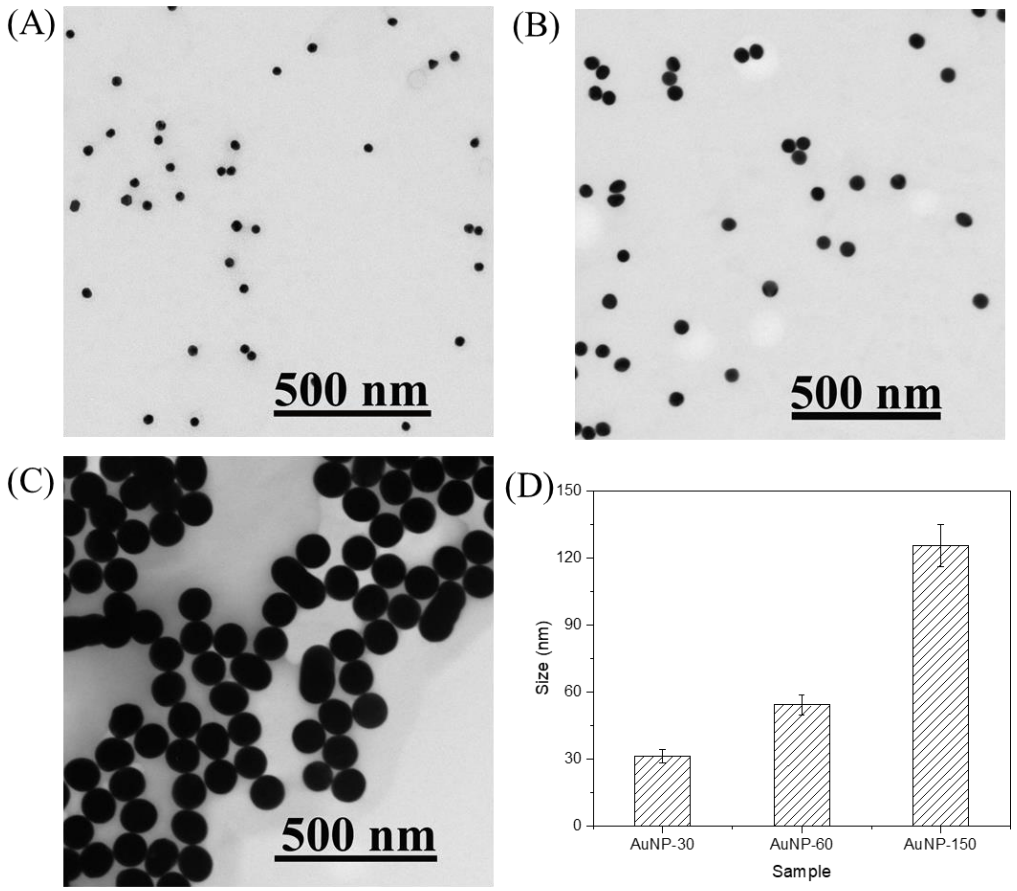

Figure 2.1. TEM images (A-C) of AuNPs with varied sizes. (A), 30 nm. (B), 60 nm. (C),150 nm. (D) Size of AuNPs with varied sizes counted from 200 particles in TEM images.

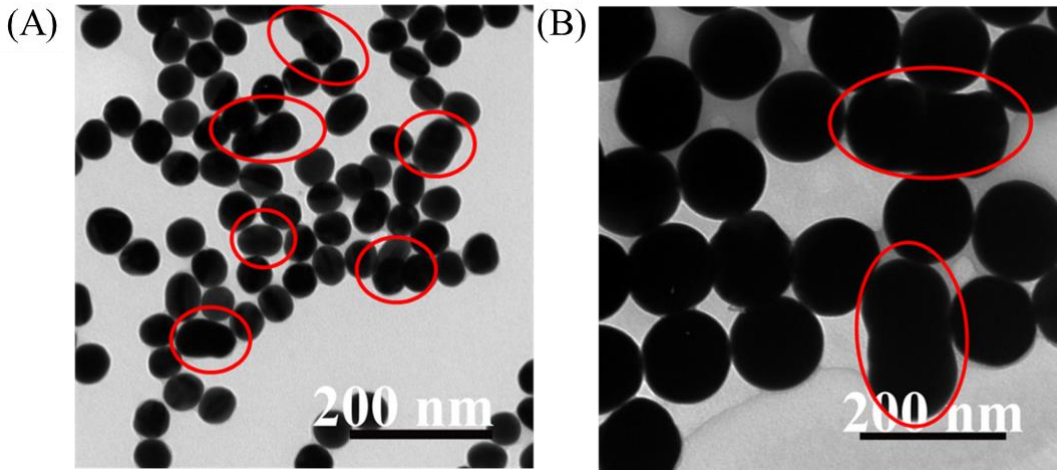

Figure 2.2. TEM images of AuNPs with irregular shapes. (A), 60 nm. (B), 150 nm.

2.3.3. Optimization of spICP-MS conditions

Accuracy of the spICP-MS measurements made in this work depend on the validity of several key assumptions of the method: (i) ^{197}Au counts for each AuNP occur entirely within one dwell time (i.e., a signal is not split between successive dwell times). (ii) ^{197}Au counts correspond to only one AuNP (i.e., a signal is not generated from multiple particles). (iii) Only ^{197}Au counts greater than the average plus five-times the background noise ($5 \times \sigma_{blank}$) of a blank solution are generated by an individual AuNP. Therefore, optimization of the spICP-MS method amounts to finding conditions of dwell time and particle concentration that best meet all three of these assumptions and yields sufficiently high signal-to-noise. This section will demonstrate this optimization strategy for the AuNP-30 sample and present the final optimized spICP-MS conditions for all three particle sizes studied in this work (30, 60, and 150 nm diameter). The parameters selected to optimize spICP-MS dwell time and particle concentration included (a) the percentage of split-particle evens, (b) the percentage of multiple-particle events, (c) the signal-to-noise ratio (S/N), and (d) the percentage of NPs detected. The remainder of this section will describe each optimizing parameter in detail. The next section (2.3.4) will then compare the *average* number of Au atoms per NP measured under optimized spICP-MS conditions for all three AuNP sizes with the same average measured by conventional ICP-MS and by TEM.

Optimizing spICP-MS conditions for minimum split- and multiple-particle events (i.e., assumptions (i) and (ii) above) was performed by fitting the number distribution histograms obtained at different dwell times with a Gaussian distribution function (Figure 2.3). This fitting allowed particle events to be categorized as split, single or multiple so that discreet percentages of split- and multiple-particle events could be determined (see section

2.2.8 for thresholds used for counting nanoparticles). Fewer split-particle events occurred with increasing dwell time in spICP-MS measurements as confirmed by the percentages of measured split-particle events for the AuNP-30 samples, which gradually decreased from 11.8 % to 0.1 % as dwell time increased from 5 ms to 50 ms (Table 2.2). However, increased dwell time also had negative impacts of lengthening the sampling period (from 3 min for a 5 ms dwell time, to 30 min for a 50 ms dwell time) and increasing the number of multiple-particle events. Although no offsetting parameter could remedy the increased sampling period with longer dwell times, it was found that particle concentration could be decreased proportionally to keep the number of multiple particle events essentially constant. The proportionality that seems to offer consistent but low multiple-particle events was a value of 250 000 s NP/L (dwell time × particle number concentration) and it was used thorough this work. Effectiveness of this proportionality is confirmed by the percentages of measured multiple-particle events for the AuNP-30 samples, which remained nearly the same and below 5 % as dwell time increased from 5 to 50 ms (Table 2.2).

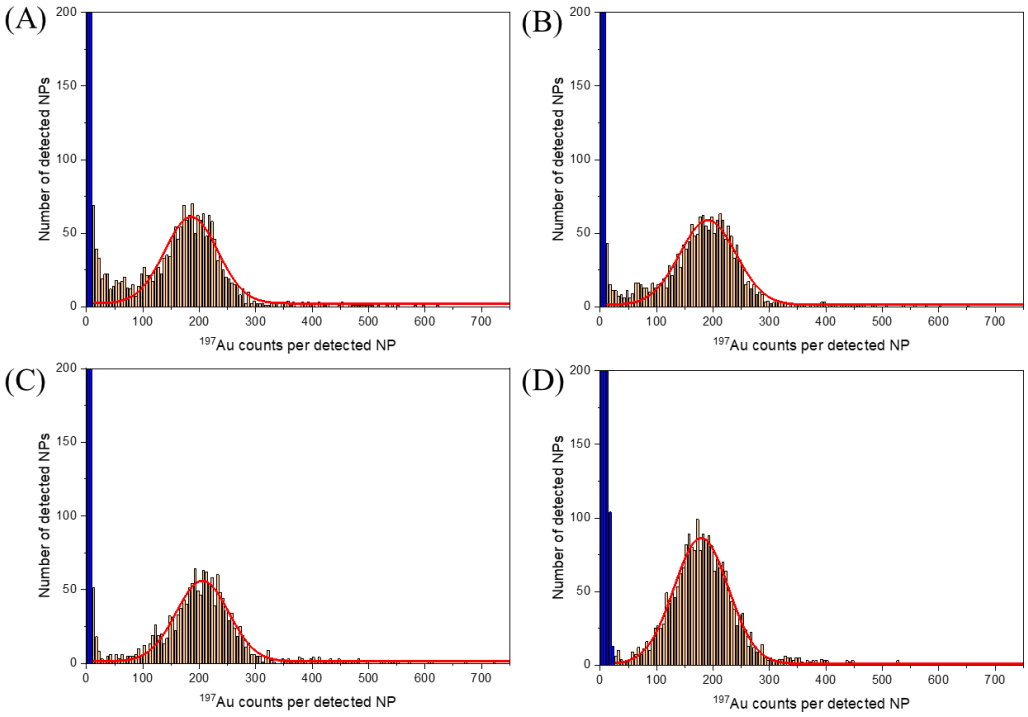

Figure 2.3. Signal histogram of raw data (background signals colored blue, particle signals colored orange) in spICP-MS measurements of AuNP-30 at different dwell times. (A), 5 ms, 5.00×10^7 NP/L. (B), 10 ms, 2.50×10^7 NP/L. (C), 20 ms, 1.25×10^7 NP/L. (D), 50 ms, 5.00×10^6 NP/L. (^{197}Au, 36 000 reading per measurement, Bin size: 5 counts).

Table 2.2. Information on the optimization of spICP-MS conditions for AuNP-30 at dwell time 5, 10, 20, and 50 ms. (^{197}Au, N=3)

Dwell time (ms)	**Particle concentration (NP/L)**	**Sampling period (min)**	**Percent of split particle event (%)**	**Percent of multiple particle event (%)**	**Signal to noise ratio**	**Percent of detected NP (%)**
5	5.00×10^{7}	3	12. ± 1.	3.3 ± 0.1	100. ± 1.	89. ± 6.
10	2.50×10^{7}	6	3. ± 1.	3.1 ± 0.4	75. ± 1.	89.4 ± 0.8
20	1.25×10^{7}	12	2.8 ± 0.4	4.4 ± 0.6	73. ± 2.	81.8 ± 0.7
50	5.00×10^{6}	30	0.1 ± 0.0	3.5 ± 0.3	36.7 ± 0.9	100. ± 2.

In addition to percentages of split- and multiple-particle events, signal-to-noise ratio (S/N) was also used as an optimizing parameter. 'Signal' in these spICP-MS experiments was measured as the *average* ^{197}Au counts per detected NP in a data set and 'noise' was set to the NP detection threshold (Eq. 2-9); i.e., the average ^{197}Au counts plus five-times the standard deviation of ^{197}Au counts obtained from solution without AuNP (i.e., a blank solution). Figure 2.4 (A-D) shows a partial time-base plot of ^{197}Au counts obtained for a blank solution using 5, 10, 20, and 50 ms dwell times, respectively. With increased dwell time, both the average intensity and standard deviation of the ^{197}Au counts increased but the standard deviation increased more. This effect yielded relative standard deviations that increased from 35.2 % with a 5 ms dwell time to 46.1 % with a 50 ms dwell time (Figure 2.4E). The source of noise in these spICP-MS experiments (i.e., ^{197}Au counts without any gold being present within an integration-measurement period defined by the dwell time) was most likely shot-noise from the electron-multiplier detector of the mass spectrometer (i.e., random electron ejections between the high-voltage dynodes of the detector). Because more of this noise is integrated over a longer dwell time measurements in spICP-MS,[85] it was generally observed that longer dwell times yield more noise in the measurements. Table 2.2 shows the S/N determined for AuNP-30 by spICP-MS at different dwell times. The ratios decreased from 100 ± 1 with a 5 ms dwell time to 36.7 ± 0.9 with 50 ms dwell time, confirming that longer dwell times result in poorer S/N.

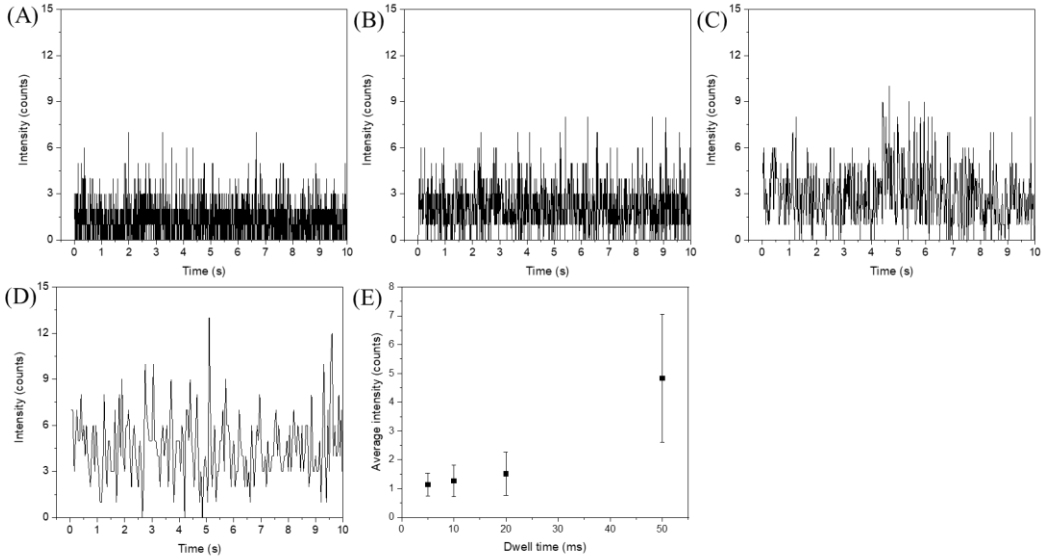

Figure 2.4. spICP-MS spectra (A-D) and average intensity and standard deviation (E) of ^{197}Au counts in blank without AuNP at dwell times. (A), 5 ms. (B),10 ms. (C), 20 ms. (D), 50 ms. (3600 readings per measurement)

The final parameter used for optimization was the percentage of NPs detected (φ) during the sampling period (Eq. 2-12) and a value close to 100 % indicated good adherence to assumption (iii) above. This percentage was calculated as the number of NPs detected during the sampling period (N_D) divided by the number calculated to reach the plasma over the same period (N_C) and multiplied by 100.

$$\varphi = \frac{N_D}{N_C} \times 100\ \% \tag{2-12}$$

The number of NPs calculated to reach the plasma over the same period was determined by using parameters of particle number concentration (P, number of nanoparticles per liter, NP/L), sample flow rate (u, 0.2 mL/min), sampling period (τ, min), and transport efficiency (η_n, see section 2.2.5), as shown in Eq. (2-13).

$$N_C = P \times u \times \eta_n \times \tau \times 10^{-3} \tag{2-13}$$

Table 2.2 shows that the percentage of detected NPs for the AuNP-30 samples did not

change much with dwell time and mostly remained well above 80 % for the conditions tested.

The optimization results given in Table 2.2 for 30 nm AuNPs demonstrate that a 10 ms dwell time and corresponding particle concentration of 2.50×10^7 NP/L yielded the best overall performance of low split- and multiple-particle percentages, high S/N, and a detected particle percentage close to 100 %. Optimization results for 60 and 150 nm AuNPs are given in Tables 2.3 and 2.4, respectively, and they reveal that longer dwell times (with correspondingly lower particle concentrations) were much better suited for these larger particles. This was especially apparent from percentages of detected NPs which significantly exceeded 100 % for shorter dwell times due to high numbers of split-particle events. Overall, a 50 ms dwell time with 5.0×10^6 NP/L yielded the best performance with both the AuNP-60 and AuNP-150 samples.

Table 2.3. Information on the optimization of spICP-MS conditions for AuNP-60 at dwell time 5, 10, 20, and 50 ms. (^{197}Au, N=3)

Dwell time (ms)	Particle concentration (NP/L)	Sampling period (min)	Percent of split particle event (%)	Percent of multiple particle event (%)	Signal to noise ratio (÷ 100)	Percent of detected NP (%)
5	5.00×10^{7}	3	27.4 ± 0.7	12.9 ± 0.5	50.5 ± 0.8	122. ± 3.
10	2.50×10^{7}	6	15. ± 2.	15.5 ± 0.5	4.0 ± 0.2	112. ± 3.
20	1.25×10^{7}	12	10.1 ± 0.4	18.7 ± 0.8	4.0 ± 0.1	112. ± 1.
50	5.00×10^{6}	30	2.7 ± 0.2	11.0 ± 0.9	2.2 ± 0.1	87. ± 2.

Table 2.4. Information on the optimization of spICP-MS conditions for AuNP-150 at dwell time 5, 10, 20, and 50 ms. (^{197}Au, N=3)

Dwell time (ms)	Particle concentration (NP/L)	Sampling period (min)	Percent of split particle event (%)	Percent of multiple particle event (%)	Signal to noise ratio (÷ 100)	Percent of detected NP (%)
5	5.00×10^{7}	3	47.9 ± 0.9	7.5 ± 0.4	48. ± 1.	172. ± 1.
10	2.50×10^{7}	6	31.5 ± 1.1	9.3 ± 0.4	42.7 ± 0.7	154. ± 3.
20	1.25×10^{7}	12	20.1 ± 0.6	11.0 ± 0.9	45.0 ± 0.7	131.3 ± 0.9
50	5.00×10^{6}	30	5.9 ± 0.3	11.7 ± 1.5	26.5 ± 0.2	103. ± 3.

2.3.4. Validation of optimized spICP-MS method by comparing results from other methods

To validate optimized spICP-MS as an accurate method for measurement of metal content across a broad MCP size range (AuNP-30, AuNP-60 and AuNP-150), results were compared with similar metal content measurements provided by TEM and conventional ICP-MS. The transformation of analysis by TEM, conventional ICP-MS, and spICP-MS to the *average* number of Au atoms per NP were described in section 2.2.4. Two parameters including relative error value and *p*-value from Analysis of Variance (one-way ANOVA) were used for statistical analysis to validate the optimized spICP-MS method. A relative error was determined by using the *average* number of Au atoms per NP from spICP-MS ($\overline{N}_{P-sp}$) at different operating conditions and that ($\overline{N}_{P-ti}$) from TEM or conventional ICP-MS (Eq. 2-14). The absolute relative error value close to 0 % indicated a good correspondence between spICP-MS at a certain operating condition and TEM or conventional ICP-MS.

$$\delta = \frac{\overline{N}_{P-sp} - \overline{N}_{P-ti}}{\overline{N}_{P-ti}} \times 100\ \% \qquad (2\text{-}14)$$

Table 2.5 for the comparison of *average* number of Au atoms per NP by TEM and spICP-MS indicates a small absolute relative error value was achieved for 30 nm AuNPs at 10 ms with a concentration of 2.50 $\times 10^7$ NP/L, for 60 nm AuNPs at 20 ms with a concentration of 1.25 $\times 10^7$ NP/L, and for 150 nm AuNPs at 50 ms with a concentration of 5.00 $\times 10^6$ NP/L. Validation results given in Table 2.6 indicate operating conditions in spICP-MS to find a small absolute relative error kept a good agreement with that form Table 2.5 for the 30 and 60 nm AuNPs. However, 150 nm AuNPs at 10 ms dwell time and corresponding particle concentration of 2.50 $\times 10^7$ NP/L had a small absolute relative error between spICP-MS and conventional ICP-MS.

A regular Analysis of Variance (one-way ANOVA) was also performed to statistically compare theses *average* number of Au atoms per NP obtained through three different methods. Table 2.5 shows no significant differences between Au atom averages obtained by spICP-MS and TEM (p-values above 0.05) except when the largest AuNPs (60 and 150 nm) were analyzed with shortest (5 ms) dwell time. The poor correspondence for 60 and 150 nm AuNPs was caused by production of many split-particle events in the spICP-MS measurements. The same type of one-way ANOVA comparison between Au atom averages obtained by spICP-MS and conventional ICP-MS are shown in Table 2.6. Here, no significant differences were indicated between paired results of these two methods (p-values < 0.05).

Table 2.5. Comparison of *average* number of Au atoms per NP with TEM method and spICP-MS at dwell time 5, 10, 20, and 50 ms.

Dwell time	**30 nm**		**60 nm**		**150 nm**	
(min)	**Relative error (%)**	***p*-value (0.05)**	**Relative error (%)**	***p*-value (0.05)**	**Relative error (%)**	***p*-value (0.05)**
5	-11.2	0.48	-59.7	9.5×10^{-5}	-39.2	0.04
10	-2.8	0.86	-20.2	0.19	-10.2	0.59
20	11.4	0.47	-8.9	0.58	11.4	0.56
50	-9.8	0.54	-24.3	0.11	6.6	0.73

Table 2.6. Comparison of *average* number of Au atoms per NP with conventional ICP-MS method and spICP-MS at dwell time 5, 10, 20, and 50 ms.

Dwell time	**30 nm**		**60 nm**		**150 nm**	
(min)	**Relative error (%)**	***p*-value (0.05)**	**Relative error (%)**	***p*-value (0.05)**	**Relative error (%)**	***p*-value (0.05)**
5	-9.0	0.50	-59.4	0.18	-35.9	0.45
10	-0.5	0.96	-19.7	0.30	-5.3	0.87
20	14.2	0.56	-8.4	0.62	17.2	0.58
50	-7.6	0.38	-23.9	0.03	12.5	0.53

2.4. Conclusion

This chapter demonstrated how to optimize spICP-MS measurements of MCPs across a broad size range and to accurately determine metal content on both a per-particle and average basis. Standard samples of AuNPs with diameters of 30 nm, 60 nm, and 150 nm were used throughout this work. Several spICP-MS experimental parameters including particle number concentration, integration period (also called dwell time), and nebulizer transport efficiency, particle ionization efficiency were investigated and the first two conditions were optimized for each particle size to achieve the smallest split- and multiple-particle events, the highest signal-to-noise (S/N), and the percent of detected NPs closest to 100%. To maintain a low but consistent percentage of multiple-particle events, it was generally found that particle concentration had be reduced proportionally if dwell time was increased. The proportionality constant that yielded the best and quickest results with the instrument used in this work was 250 000 s NP/L (e.g., for 30nm AuNPs, (5 ms)·(5 × 10^7 NP/L) = 250 000 s NP/L). It was also generally found that increasing the dwell time with a proportional decrease in particle concentration yielded lower percentage of split-particle events and higher percentage of detected NP, but a poorer S/N. Within these constraints, the optimum dwell time and particle concentration for each particle size were found to be 10 ms dwell time with 2.50 ×10^7 NP/L for 30 nm AuNPs and 50 ms dwell time with 5.0 ×10^6 NP/L for 60 and 150 nm AuNPs. Finally, these optimized spICP-MS conditions for each particle size were validated by comparing values of *average* number of Au atoms per NP with the same parameter determined by TEM (another single-particle method) and conventional ICP-MS (a bulk measurement method). No statistically significant differences were evident between the results determined by these different methods, so it

may be concluded that the spICP-MS method described herein is a promising tool to quantify metal content in MCPs over a wide range of particle size.

CHAPTER III

AN UNPRECEDENTED METAL DISTRIBUTION IN SILICA NANOPARTICLES CHARACTERIZED BY SINGLE-PARTICLE INDUCTIVETLY COUPLED PLASMA MASS SPECTROMETRY

3.1. Introduction

Metal-containing nanoparticles (MCPs) are finding increasing use in fields of catalysis,[86, 87] sensing,[88, 89] and medicine,[48-50] yet this greater use of MCPs raises questions about metal distribution at the nanoparticle level. Typical nanomaterial characterization methods such as UV-Vis spectroscopy and dynamic light scattering only provide bulk concentration of the metal that is an average across many particles. The few traditional methods that provide analysis at the particle level, such as scanning electron microscopy coupled with energy dispersion spectroscopy (SEM-EDS) and nanoparticle tracking analysis (NTA), suffer numerous limitations including drying artifacts, long analysis times (or low number of per-particle analyses), poor selectivity, and low sensitivity.[90, 91]

Single-particle inductively coupled plasma-mass spectrometry (spICP-MS) is a mature method that provides reliable particle-by-particle analysis for large numbers of particles (> 10,0000) in a relatively short period of time (< 3 min). The method combines the high sensitivity and selectivity inherent to the ICP-MS with rapidly timed measurements designed to capture the selected isotope signal of individual nanoparticles. By introducing nanoparticles to the plasma as a low-concentration aqueous solution (< 1 $\times 10^8$ nanoparticles/L), vaporization, atomization and ionization of the individual particles generates an ion cloud that is sampled by the mass spectrometer and detected as a transient signal pulse (< 5 ms) for the selected metal isotope. The intensity of the pulse is proportional to the amount of target metal per nanoparticle, whereas the number of detected

pulses during the ca. 3 min sampling period provides the particle number concentration.

Over the last decade, most applications of spICP-MS have focused on the per-particle analysis of one-component nanoparticles such as gold and silver (AuNPs and AgNPs).[71, 92-94] Montoro Bustos et al. reported that spICP-MS had capability to detect mean size and number size distribution of commercial AuNPs regardless of size or coating.[82] Minelli et al. have synthesized different binding degrees of 80 nm AuNPs and measured their nanoparticle number concentration by using spICP-MS.[95] The measurement with spICP-MS was in close agreement for monodisperse AuNPs within 10 % agreement. Tadjiki et al. demonstrated that the density values of engineered AgNPs calculated from spICP-MS methodology were in reasonable agreement with the results with combination of centrifugal field-flow fractionation and transmission electron microscopy.[96] Meanwhile, our has group reported that AuNPs modified with specialized DNA are able to determine ionic mercury with a detection of limit as low as 0.031 ng/L.[97]

Although there have also been other reported studies and applications utilizing spICP-MS,[98-102] very little research to date has focused on determination of per-particle metal concentration distribution in multicomponent NPs. To date only one study has demonstrated the use of spICP-MS to determine the per-particle metal composition of a multicomponent MCP; in this case, a MCP derived from environmental samples.[103] The present work provides a second example of per-particle metal determination for a model multicomponent MCP; in this case for a very common type of silica nanoparticle composite synthesized using microemulsion conditions. It also demonstrates the benefit of screening per-particle composition by spICP-MS versus bulk methods (UV-visible absorption and conventional ICP-MS), because a highly unusual and unprecedented metal dopant

distribution was found for this common type of silica-based MCP.

3.2. Experimental Section

3.2.1. Materials

Tetraethyl orthosilicate (TEOS, 99.999 %), tris(2,2`-bipyridyl) dichlororuthenium(II) chloride hexahydrate ($[Ru(bpy)_3]Cl_2 \cdot 6H_2O$, 99.95 %), *N*-[(3-trimethoxysilyl)propyl]-ethylenediamine triacetic acid trisodium salt (40 % in water), polyoxyethylene glycol tert-octylphenyl ether (Triton X-100, 2-$(C_8H_{17})C_6H_4(OCH_2CH_3)_{10}OH$, BioXtra), ammonia hydroxide (28.0 % NH_3 in water), *n*-hexanol (>= 99 %), cyclohexane (99.5 %), acetone (>= 99.9 %), and ethanol (>= 99.5 %) were obtained from Sigma-Aldrich (St. Louis, MO, USA). A stock standard suspension of 150 nm gold nanoparticles capped with citrate was purchased from Nanopartz (Loveland, CO, USA). Stock standard solutions of 100,000 $\mu g/L^{-1}$ ionic ruthenium and of 100,000 $\mu g/L^{-1}$ gold in nitric acid were purchased from Inorganic Ventures (Christiansburg, VA, USA) and were each used to make working standards with 2 % optima-grade nitric acid (Radnor, PA, USA) for ICP-MS calibrations. Deionized (DI) water (18.2 MΩ·cm) was produced from a Millipore Synergy (Burlington, MA, USA) purification system and used for all nanoparticle synthesis and all analysis in this work. Grade 4.8 liquid argon was used for plasma and nebulizer operation in all ICP-MS measurements. Grade 5 helium was used as an inert gas in kinetic energy discrimination for all conventional ICP-MS measurements.

3.2.2. Instruments

A Hitachi 7500 transmission electron microscope (Tokyo, Japan) was used to take transmission electron microscope (TEM) images of purchased gold nanoparticles (AuNPs) and synthesized tris(bipyridyl)ruthenium(II)-doped silica nanoparticles (Ru-SiO_2 NPs). A

Zetasizer Nano (Malvern Panalytical, UK) was used for the measurement of Zeta potential and hydrodynamic diameter of Ru-SiO_2 NPs. A PerkinElmer Lambda 1050 UV/VIS/NIR spectrometer (Santa Clara, CA, USA) was used to measure the absorbance spectra of Ru-SiO_2 NPs. A Thermo Scientific iCAP Qc quadrupole ICP-MS (Waltham, MA, USA) controlled with Qtegra^{TM} software (version 2.8.2944.202) was used to perform all ICP-MS measurements. This the sampling interface of this instrument included a Teledyne CETAC ASX560 autosampler operating with a carbon fiber sample probe, a multichannel peristaltic pump operating with PVC tubing, a microflow perfluoroalkoxy nebulizer, a Peltier-cooled quartz cyclonic spray chamber. To evaluate the performance of this instrument, THERMO-4AREV standard solution obtained from Thermo Scientific (Waltham, MA, USA) was checked daily for a maximum ^{59}Co, ^{115}In, ^{238}U and minimum $^{140}Ce^{16}O/^{140}Ce$ signal. All single particle measurement with ICP-MS was performed in high-sensitivity standard mode. Microsoft Excel Spreadsheet and OriginPro Lab (Northampton, MA, USA) were used for data processing and measurement evaluation.

3.2.3. Synthesis of Ru-SiO_2 NPs

The Ru-SiO_2 NP samples were prepared in triplicate by a water-in-oil microemulsion method similar to the literature.[104] For each sample, 7.50 mL of cyclohexane, 1.77 mL of Triton X-100, and 1.60 mL of *n*-hexanol were combined and stirred for 20 min to produce a stable oil-phase solution. A stable microemulsion was formed by adding 240 μL of water solution containing 0.0, 13.3, 26.7, 53.4, to 106.8 mM tris(bipyridyl)ruthenium(II) ($[Ru(bpy)_3]^{2+}$) and stirring for an additional 20 min. After that, 240 μL of TEOS, 100 μL of ammonia hydroxide was added in 20 min intervals and the hydrolysis reaction was allowed to proceed with stirring for 24 h. To prevent aggregation

of nanoparticles in aqueous solution, they were post-coated with carboxyl groups by adding 100 μL of TEOS and 20 μL of N-[(3-trimethoxysilyl)propyl]ethylenediamine triacetic acid into the microemulsion system. After another 24 h, acetone was added to break the microemulsion and the post-coated Ru-SiO_2 NPs were isolated by centrifugation at 11,000 rpm for 15 min. The particles were re-suspended and washed three times with ethanol and three times with deionized water. The Ru-SiO_2 NPs were re-suspended in deionized water. The mass concentration (C_i, μg/L) of Ru-SiO_2 NPs (Eq. 3-1) was determined simply by dividing the mass (m_c, mg) of dried Ru-SiO_2 NPs by the volume (V, 1.5 mL) of these Ru-SiO_2 NPs liquid sample. A 1.5 mL of varied doping level of Ru-SiO_2 NPs suspension was taken into one glass container to dry for 24 h at 120 ℃ and then used to weight to obtain the mass (m_c, mg) of these Ru-SiO_2 NPs.

$$C_i = \frac{m_c}{V} \times 10^3 \tag{3-1}$$

The suspensions containing Ru-SiO_2 NPs with different doping levels were adjusted to 0.4 mg/mL to yield a stock solution.

3.2.4. Concentration unit conventions used for nanoparticle solutions

Two concentration units, particle number concentration (P, number of nanoparticles per liter, NP/L) and mass concentration (C_i, mass of metal per liter, μg/L), were used for measurements of metal-containing nanoparticles (MCPs) solutions by UV-vis, conventional ICP-MS, and spICP-MS. The number concentration was usually used for solutions consisting of whole MCPs, while the mass concentration was typically used for ionic metal solutions. However, three specific situations favored use of the opposite conventions: (i) Number concentrations were used for solutions of digested metal nanoparticles that contained ionic metal. (ii) Mass concentrations were used for solutions

of whole MCPs in conventional ICP-MS measurements of particle ionization efficiency. (iii) Mass concentrations were used with bulk analysis methods (e.g., UV-vis and conventional ICP-MS) for solutions of whole MCPs.

3.2.5. Measurement of mass of metal per NP

spICP-MS. Instrument operating conditions are listed and compared to conventional ICP-MS conditions in Table 3.1. Calibration and quality-control steps typically followed the RIKILT Standard Operating Procedure for counting and sizing of nanoparticles.[25] A 5 ms dwell time (t_{dwell} , ms) and a 180 s sampling interval (corresponding to 36,000 individual measurement) were used in most experiments. Sample flow rate (*u,* 0.20 mL/min) was measured daily in triplicate by weighing 600 s of water uptake. The measurement of nebulizer transport efficiency (η_n) by using standard AuNPs was described Chapter II section 2.2.5 and its value was 8. 9 ± 0.8 %. NP samples were diluted to 5.0×10^7 NP/L with high purity water, target isotope count was monitored (^{197}Au for AuNP and ^{102}Ru for Ru-SiO_2 NP), and a series of ionic metal calibration standards (0.1 – 10.0 µg/L for ionic Au standards and 0.05 –5.0 µg/L for ionic Ru standards) were measured to allow conversion of counts per NP (I_p) to a metal mass per NP (W_p, µg).

To determine the metal mass per NP using the metal isotopes counts per NP in spICP-MS measurement, the transformation of the ionic metal solution concentration (C_i, µg/L) to a mass of ionic metal entering the plasma per dwell time (*W,* µg) was carried out using the sample flow rate (*u,* 0.20 mL/min) and nebulizer transport efficiency (η_n), as shown in Eq. 3-2.[64]

$$W = \eta_n \times u \times t_{dwell} \times C_i \quad (3\text{-}2)$$

The measured counts per dwell time (*I*) for each ionic metal standard solution were

averaged over the entire sampling period ($\bar{I}$). Afterwards, the calibration equation of $\bar{I}$ versus W (with slope m and y-intercept $b_{\text{forced}} = 0$) yielded an expression for mass of metal per NP (W_p, μg) using the isotope count per NP (I_p) occurred within one dwell time and the particle ionization efficiency (η_i, see Chapter II section 2.2.6 for AuNPs and Chapter III section 3.2.7 for Ru-SiO_2 NPs below) in Eq. 3-3.[64]

$$W_P = \frac{I_p \times \eta_i}{m} \tag{3-3}$$

To minimize the contribution of instrument noise to the detected NP signals, only signals greater than a discrete noise threshold (see Chapter II section 2.2.8 for description) were considered NP events. This threshold was determined from signals measured for a blank solution and processed over an entire sampling period 180 s in Microsoft Excel Spreadsheet; specifically, the blank signal average plus five-times the blank signal standard deviation ($\overline{I_{blank}} + 5 \times \sigma_{blank}$).

Table 3.1. Operation parameters for both conventional and single particle ICP-MS measurements.

Parameter	Conventional measurement	Single-particle measurement
Sample introduction		
peristaltic pump	4-channel, 12-roller	4-channel, 12-roller
pump speed (rpm)	20	20
sample tubing (mm ID)	0.508	0.508
internal-standard tubing (mm ID)	0.508	not used
waste tubing (mm ID)	1.295	1.295
nebulizer	Microflow PFA-ST	Microflow PFA-ST
nebulizer gas flow (L/min)	1.09	1.05
spray chamber	quartz cyclonic	quartz cyclonic
spray chamber temperature (℃)	2.70	2.70
Plasma		
torch	ICAP Q quartz	ICAP Q quartz
Rf power (W)	1550	1550
coolant gas flow (L/min)	14	14
plasma gas flow (L/min)	0.8	0.8
sample injector	quartz (2.5 mm ID)	quartz (2.5 mm ID)
Mass spectrometer		
sample cone	nickel	nickel
skimmer cone	nickel	nickel
cone insert	3.5 mm	2.8 mm
mode	KED	STDS
KED gas flow (mL/min)	4.6	0
dwell Time (ms)	50	5
sweeps	10	0
internal standards	^{74}Ge, ^{209}Bi	none

Transmission Electronic Microscope. The characterization of AuNPs by TEM was described in Chapter II 2.2.4. In the Ru-SiO_2 NPs samples, the preparation of TEM samples also followed the instruction from the UK National Physical Laboratory.[83] Briefly, Ru-SiO_2 NPs with varied dopant liquid samples were diluted with DI water to particle concentration of 1.0×10^9 NP/L. Prior to pumping a 3.0 μL aliquot of the solution onto the surface of a copper grid to make the TEM samples, the solutions were sonicated for 2 min in a water bath. The TEM samples were dried at room temperture for 24 h before characterization. The diameter of individual Ru-SiO_2 NP was measured by using the TEM images with Image J software. In the AuNPs, a theoretical metal mass per NP (W_{t-Au}, μg) of AuNPs yielded by using the TEM-measured radius (R, cm) and assumed density of AuNPs (ρ, 19.3 g/cm^3) in Eq. 3-4.

$$W_{t-Au} = \frac{4}{3}\pi R^3 \times \rho \times 10^6 \quad (3\text{-}4)$$

In the Ru-SiO_2 NPs over a broad doping level samples, an assumption which the $[Ru(bpy)_3]^{2+}$ dispersed in an individual nanodroplet was entirely encapsulated by the silica space was established to calculate the theoretical metal mass per NP of Ru-SiO_2 NPs. The theoretical metal mass per NP (W_{t-Ru}, μg) of Ru-SiO_2 NPs was determined (Eq. 3-5) by using the TEM-measured radius (R, cm), the amounts of $[Ru(bpy)_3]^{2+}$ dispersed in single formed nanodroplet (m_r, moles per milliliter, M/mL), and the ruthenium molecular mass (M, 101 g/mol).

$$W_{t-Ru} = \frac{4}{3}\pi R^3 \times m_r \times M \times 10^6 \quad (3\text{-}5)$$

3.2.6. Measurement of number of metal atoms per NP

spICP-MS. The detailed information on characterization of Ru-SiO_2 NPs with varied doping levels by spICP-MS was descripted section 3.2.5 above. To determine the

number of metal atoms per NP (N_P) using the metal isotopes counts per NP in spICP-MS measurement, the metal mass per NP (*W,* μg) was transformed to per-particle metal atoms number by using the metal molecular mass (M, 101 g/mol) and Avogadro constant (N_A) in Eq 3-6. [64]

$$N_P = \frac{W_P}{M} \times 10^{-6} \times N_A \tag{3-6}$$

Finally, to compare the N_p results of per-particle measurement (spICP-MS) with the *average* number of Ru atoms per NP ($\overline{N}_p$) results of bulk measurements (UV-vis and conventional ICP-MS) for the synthesized Ru-SiO_2 NP, the integration of number of metal atoms per NP (N_P) during each sample period was averaged by the *n* measurements over this entire sampling period. as shown in Eq. (3-7).

$$\overline{N}_P = \frac{\sum_{i=1}^{n} N_p}{n} \tag{3-7}$$

UV-vis absorbance. Solutions of Ru-SiO_2 NPs with varied doping levels were serially diluted 1: 2 from 0.4 mg/mL to 0.025 mg/mL with DI water. Meanwhile, calibration standard solutions consisting of $[Ru(bpy)_3]^{2+}$ were prepared by serial dilution for concentrations ranging from 1.0 μM to 40.0 μM. Absorbance of Ru-SiO_2 NPs and $Ru(bpy)_3^{2+}$ solutions were recorded at a wavelength 454 nm using a 1-cm pathlength cell. The particle number concentration of the Ru-SiO_2 NPs solution (*P*, nanoparticles per L, NP/L) was calculated using the mass concentration of Ru-SiO_2 NPs suspension (C_i, μg/mL), assumed Ru-SiO_2 NPs density (same with pure SiO_2 NPs, ρ, 1.92 g/cm^3),[105] and radius of Ru-SiO_2 NP measured by TEM (*R*, cm), as shown in Eq. 3-8.

$$P = \frac{C_i}{\frac{4}{3}\pi R^3 \times \rho \times 10^6} \tag{3-8}$$

The molar concentration of $[Ru(bpy)_3]^{2+}$ (C_m, mol/L) in the measured Ru-SiO_2 NPs liquid

solution was determined by substituting the absorbance of Ru-SiO_2 NPs solution into the calibration equation of the absorbance and molar concentration of $[Ru(bpy)_3]^{2+}$. The *average* number of Ru atoms per NP ($\bar{N}_P$) was then calculated using molar concentration of $[Ru(bpy)_3]^{2+}$, Avogadro's number (N_A), and particle number concentration (P, nanoparticles per L, NP/L) of the Ru-SiO_2 NPs suspension, as shown in Eq. 3-9.

$$\bar{N}_P = \frac{N_A \times C_m}{P} \tag{3-9}$$

Conventional ICP-MS. Instrument operating conditions are listed in Table 3.1. All other instrument parameters were optimized to meet requirements as defined by the manufacturer prior to method calibration and analysis. Calibration and quality-control procedures typically followed EPA method 200.8 (Revision 5.4). Sample analysis was performed in KED mode for all experiments. Samples consisting of 10.0 μg/L of Ru-SiO_2 NPs with different doping levels in 2 % nitric acid and 10 μg/L of Ge and Bi internal standards in 2 % nitric acid were combined from separate pump channels and introduced together to the ICP-MS nebulizer. Integrated isotope ^{102}Ru signal was monitored relative to the internal standards (^{74}Ge and ^{209}Bi) and its signal was calibrated using dissolved Ru standards with 0.05 –5.0 μg/L in 2 % nitric acid. This conventional ICP-MS operation constitutes a bulk analysis method whereby ^{102}Ru signal was integrated and averaged over a large volume of solution because the long dwell time and high sweep averaging number. The *average* number of Ru atoms per NP ($\bar{N}_P$) (Eq. 3-10) was calculated by multiplying a mass concentration of Ru-SiO_2 NPs (C_i, μg/L) by Avogadro's number (N_A) and dividing by the ruthenium molecular mass (M, 101 g/mol) and the particle number concentration of the Ru-SiO_2 NPs solution (P, nanoparticles per L, NP/L, see Eq. 3-9 above).

$$\bar{N}_P = \frac{N_A \times C_i}{P \times M \times 10^6} \tag{3-10}$$

3.2.7. Measurement of particle ionization efficiency

The particle ionization efficiency (η_i) of AuNPs and Ru-SiO_2 NPs with varied doping levels in spICP-MS was performed according to the literature with little change.[64] The measurement of particle ionization efficiency for 150 nm AuNP was described in Chapter II section 2.2.6 and found to be 65 % ± 2 %. For Ru-SiO_2 NPs with varied doping level liquid samples, a 0.5 mL of 400.0 mg/L Ru-SiO_2 NPs suspension was dissolved with 2.0 mL of 1 M sodium hydroxide at room temperature for 24 h. Solutions of both dissolved and undissolved Ru-SiO_2 NPs were first analyzed by spICP-MS at a concentration of 5 × 10^8 NP/L and 5 ms dwell time, and then by conventional ICP-MS. The ionization efficiency was determined by dividing the intensity of undigested Ru-SiO_2 NPs by the intensity of digested Ru-SiO_2 NPs and then multiplying by 100. No significant difference was found between the intensity of digested and undigested Ru-SiO_2 NPs in conventional ICP-MS. Hence, the particle ionization of all the Ru-SiO_2 NPs was 100 %.

3.2.8. Mass per nanoparticle number distribution histogram

In the spICP-MS measurements of Ru-SiO_2 NPs with varied doping levels and of AuNPs, the nanoparticle signals were discriminated from the background noise and converted to mass of metal (Ru or Au) per NP using Eq. 3-3 (see section 3.2.5 above). In the TEM measurements of all Ru-SiO_2 NPs and of AuNPs, a theoretical metal mass per NP yielded in Eq. 3-4 (see section 3.2.5 above). Therefore, A mass of metal per NP number distribution histogram was plotted with a y-axis labeling for number of detected NP and an x-axis labeling for mass per NP or theoretical mass per NP in units of $\mu g \times 10^{12}$ using OriginPro Lab.

3.3. Results and Discussion

3.3.1. Project synopsis—purpose, strategy, and results

The preceding chapter demonstrated how spICP-MS can be optimized for accurate analysis of MCPs that have a simple composition of one metal-containing material. The purpose of this chapter is to extend this spICP-MS analysis to MCPs that have a more complex composition; specifically, to multicomponent materials where the metal analyte is only one part of the NP matrix. For this purpose, we selected silica nanoparticles synthesized by the water-in-oil micro-emulsion method and doped with fixed amounts of $[Ru(bpy)_3]^{2+}$ (Ru-SiO_2 NPs) as the MCP model. Scheme 3.1 summarizes the experimental strategy used along with some basic results that will be discussed later in greater depth.

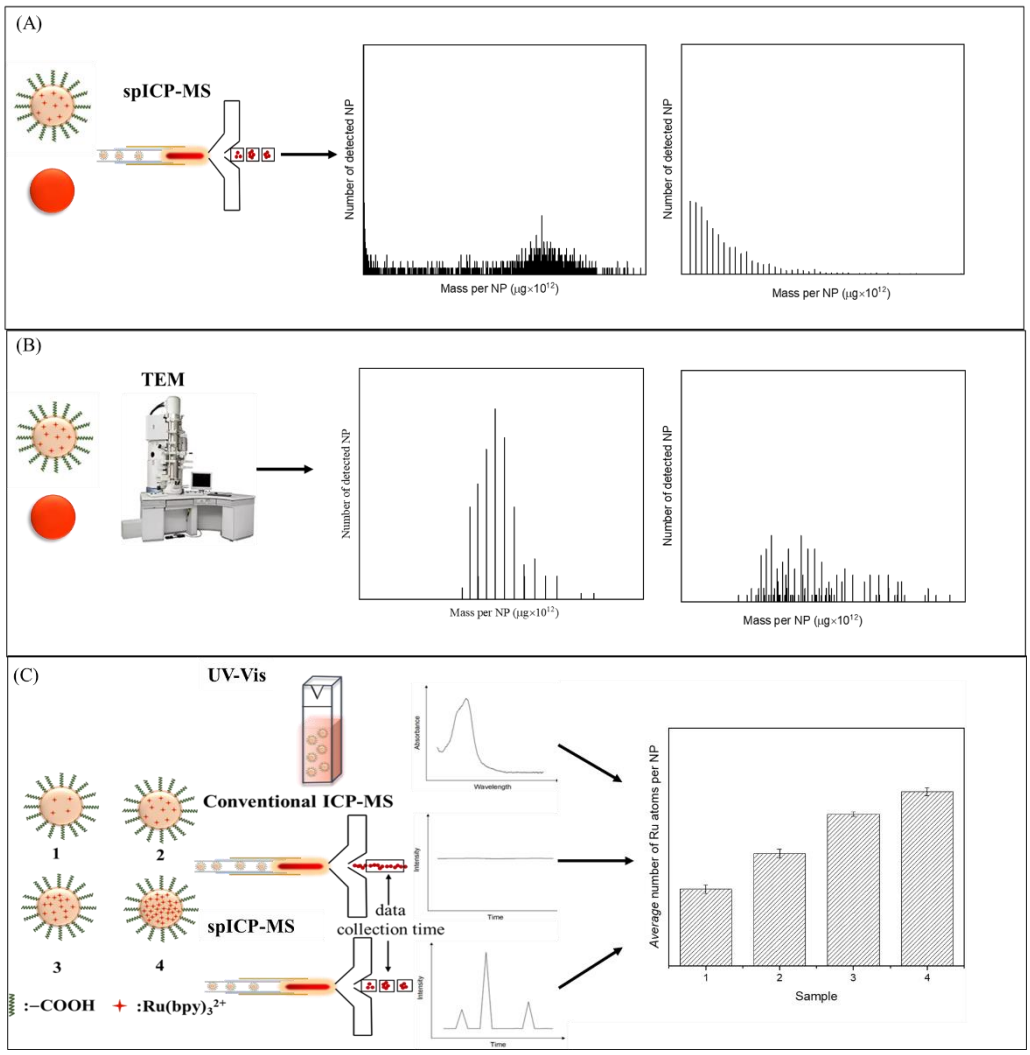

Scheme 3.1. (A) Measured mass per NP number distribution of AuNP and Ru-SiO_2 NPs by spICP-MS. (B) Theoretical mass per NP number distribution of AuNP and Ru-SiO_2 NPs by TEM. (C) *Average* number of Ru atoms per NP of Ru-SiO_2 NPs with varied doping levels by UV-Vis, conventional ICP-MS, and spICP-MS. a, AuNP. b, Ru-SiO_2 NPs.

spICP-MS results of Ru-SiO_2 NPs with varied doping levels were compared to spICP-MS results of standard AuNPs to determine whether their number distribution histograms differed because of the type of MCPs analyzed. The results showed clear and unexpected differences (Scheme 3.1 A). The AuNPs demonstrated a Gaussian-like distribution of metal content typical of a single-component MCP. However, the Ru-SiO_2 NPs demonstrated a consistent yet unexpected geometrical distribution in metal content

(i.e., exponential increasing numbers of particles with lower metal content). Such an odd metal-content distribution could only result from extreme inhomogeneity in either NP size or composition.

To rule out the size variation factor, the Ru-SiO_2 NPs and standard AuNPs were evaluated by TEM, another single-particle analysis method. It was found that both types of MCPs had a consistent spherical shape and a limited variation in NP diameter, so when the TEM size data were converted to number distribution histograms by assuming a spherical and the same per-particle metal content, both types of NPs yielded similar Gaussian-like distributions (Scheme 3.1 B). This finding confirmed that NP size variation did not cause the unusual geometrical distributions of metal-content in the Ru-SiO_2 NPs and that inhomogeneous metal composition was the most likely factor.

To determine whether this unusual, inhomogeneous metal composition of MCPs is evident from bulk-analysis methods—the methods typically used to characterize MCPs—*average* numbers of Ru atoms per NP determined by spICP-MS (Eq. 3-6 and 3-7 in section 3.2.5) were compared to *average* numbers of Ru atoms per NP determined by the bulk methods of UV-vis and conventional ICP-MS (Scheme 3.1 C). Because these comparisons showed very small differences, it is clear bulk methods of MCP characterization are insufficient to understand, much less identify, nanomaterials with inhomogeneous metal composition. Only particle-by-particle analysis by a method like spICP-MS is capable of this type characterization and it should become a routine part of MCP development.

3.3.2. Characterization of Ru-SiO_2 NPs and AuNP with TEM

Preparation of metal-doped silica nanoparticles has typically involved either the

water-in-oil microemulsion method or the Stöber method.[106-109] The former produces NPs that are smaller and with more narrow size distribution, so it was used to synthesize the Ru-SiO_2 NP samples in this work. Another benefit of this method is the relative ease with which doping levels can be varied by changing the concentration of dopant in the water used to form the microemulsion. The concentration of $[Ru(bpy)_3]^{2+}$ in the water addition was varied from 0.0 (control) to 13.3, 26.7, 53.4, and 106.8 mM. The nascent samples were also post-coated with –COOH groups to inhibit aggregation in aqueous suspension. TEM images of these samples (Figure 3.1 A-E) showed the clean, well-defined, and spherical NPs. And these nanoparticles were in very good contrast to the grid substrate, which was important to obtain accurate and reliable measurement of nanoparticle's diameter. The average size of Ru-SiO_2 NPs was 148 nm ± 9 nm, 139 nm ± 8 nm, 128 nm ± 7 nm, 127 nm ± 8 nm, and 151 nm ± 16 nm corresponding to 0.0, 13.3, 26.7, 53.4, and 106.8 mM of dopant. The TEM images also indicated these NPs were spherical in shape and monodispersed at varied doping levels. Similarly, the morphology and diameter of AuNP were characterized by TEM. Figure 3.1F shows AuNPs with average size of 126 nm had an extremely narrow deviation with 9 nm over 200 individual particles. These monodispersed AuNPs were also spherical in geometry.

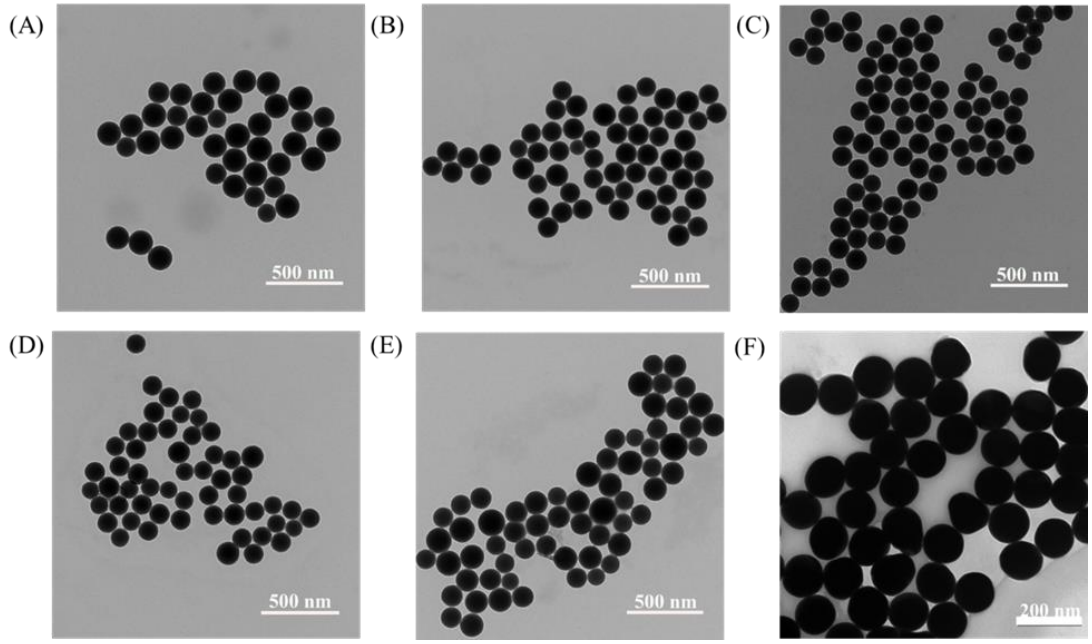

Figure 3.1. TEM images of (A) AuNP and (A-E) Ru-SiO_2 NPs with different doping levels and (F) AuNP. (A), 0.0 Mm. (B), 13.3 mM. (C), 26.7 mM. (D), 53.4 mM. and (E), 106.8 mM.

3.3.3. Initial characterization of Ru-SiO_2 NPs and AuNPs using spICP-MS

The capacity of spICP-MS to accurately quantify the number of Ru-SiO_2 NPs in solution is demonstrated in Figure 3.2. As the knowledge from Chapter II, results of MCPs with a size close to 126 nm by the spICP-MS at 50 ms dwell time yielded accurate measurement, while the S/N was poor. Therefore, a short dwell time at 5 ms was used for the spICP-MS analysis of Ru-SiO_2 NPs. Ru-SiO_2 NPs samples with particle number concentrations increasing from 1×10^7 to 1×10^8 NP/L were analyzed and a 5 ms dwell time was used in all cases. The number of detected NP events over the sampling period is expected to be proportional to the particle number concentration of Ru-SiO_2 NPs entering the plasma. This correlation was demonstrated by the linear increase in number of detected NP with the particle concentration increasing from 1×10^7 to 1×10^8 NP/L and it was consistent for Ru-SiO_2 NPs with different Ru contents.

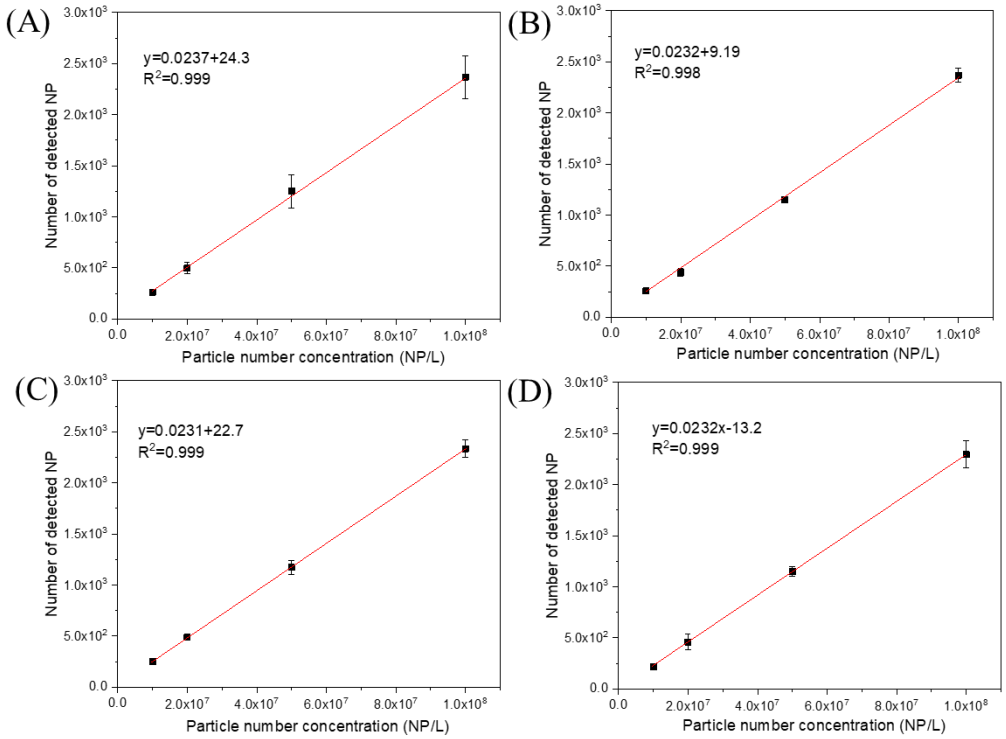

Figure 3.2. Plots of number of detected NP and particle number concentration of Ru-SiO_2 NPs with varied doping levels from 1×10^7 to 1×10^8 NP/L entering the plasma in spICP-MS measurements. (A), 13.3 mM. (B), 26.7 mM. (C), 53.4 mM. (D), 106.8 mM. (^{102}Ru, dwell time 5 ms, sampling period 180 s)

Control measurements for spICP-MS analysis of Ru-SiO_2 NPs were carried out using blank solutions or NP solutions containing 5.0×10^7 NP/L (Figure 3.3). Compared with blank samples without nanoparticles and solutions with nanoparticles in the absence of $[Ru(bpy)_3]^{2+}$, increasing the concentration of dopant from 13.3 mM to 106.8 mM resulted in the increase of the averaged intensity of detected NP from 2.1 ± 0.3 to 16.0 ± 0.4 counts, indicating more $[Ru(bpy)_3]^{2+}$ successfully doped into the SiO_2 NPs when increasing the dopant concentration in the water-in-oil microemulsion method.

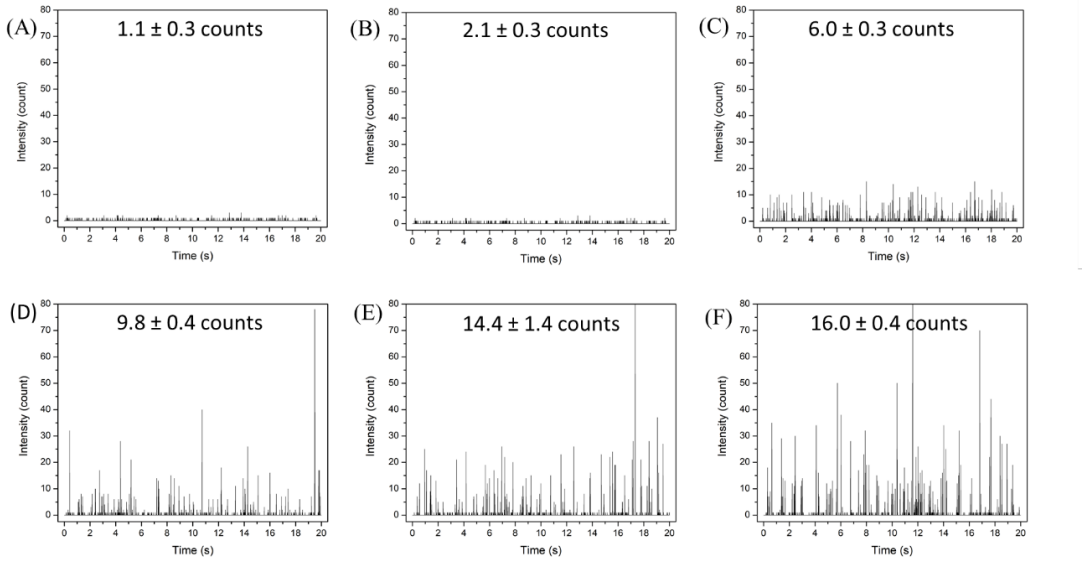

Figure 3.3. Partial spICP-MS raw spectrum of ^{102}Ru isotope events in Blank solution and Ru-SiO_2 NPs with different doping degrees liquid samples. (A). Blank without NP. (B), 0.0 mM. (C), 13.3 mM. (D), 26.7 mM. (E), 53.4 mM. (F), 106.8 mM. (^{102}Ru, dwell time 5 ms, sampling period 180 s)

Similarly, control measurements for spICP-MS analysis of 150 nm AuNPs were carried out using blank solutions or NP solutions containing 5.0 ×10^7 NP/L at a 5 ms dwell time (Figure 3.4). The ^{197}Au signal from a AuNPs solution (average intensity of $60_{46.4}$ ± $2_{62.8}$ counts) was much higher than that from the blank solution without NPs (average intensity of 1.2 ± 0.4 counts), indicating a high signal-to-noise ratio under these spICP-MS conditions. As also demonstrated by optimizations of Chapter II, the short dwell time for such a large particle diameter resulted in a larger number of detected NP events was found in the spICP-MS measurement in comparison to the known particle concentration during the 180 s sampling period, indicative of a high percentage of split-particle events in these conditions.

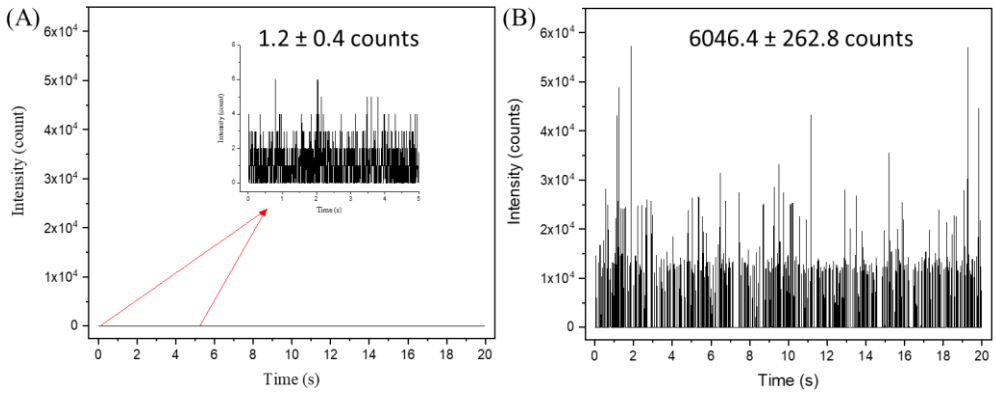

Figure 3.4. Partial spICP-MS raw spectrum of ^{197}Au isotope events in Blank without NPs solutions and AuNPs liquid samples. (A), Blank without AuNPs. Insert is enlarging the spICP-MS spectra of Blank without any AuNPs within 5s. (B), AuNPs. (^{197}Au, dwell time 5 ms, sampling period 180 s)

3.3.4. Metal mass per NP distributions of Ru-SiO_2 NPs and AuNPs

Metal isotope intensity per NP event was converted to metal mass per-particle metal mass per NP using Eq. 3-2 and 3-3 (see section 3.2.5) in order to compare number distributions of metal content for these two types of MCPs. The measured per-particle Ru dopant distribution across 2,500 number individual Ru-SiO_2 NPs was plotted with the number of detected NP and mass per NP (Figure 3.5). The most striking and unusual aspect of these distributions was the lack of a Gaussian-like peak that would indicate a consistent concentration of $[Ru(bpy)_3]^{2+}$ per NP. Instead, the observed distributions consistently showed the highest number of detected NP with the smallest mass of Ru and exponential smaller numbers of NPs with higher measured Ru masses. This pattern matches a geometric distribution and has never been reported previously for MCPs. Increasing the amount of $[Ru(bpy)_3]^{2+}$ dopant in the formation of Ru-SiO_2 NPs increased the number of NPs with high Ru mass while also decreased the number of events with small Ru mass per NP. This effect effectively broadened and flattened the distribution and resulted overall in a higher

Ru mass per NP when averaged over all NP detected in the data set.

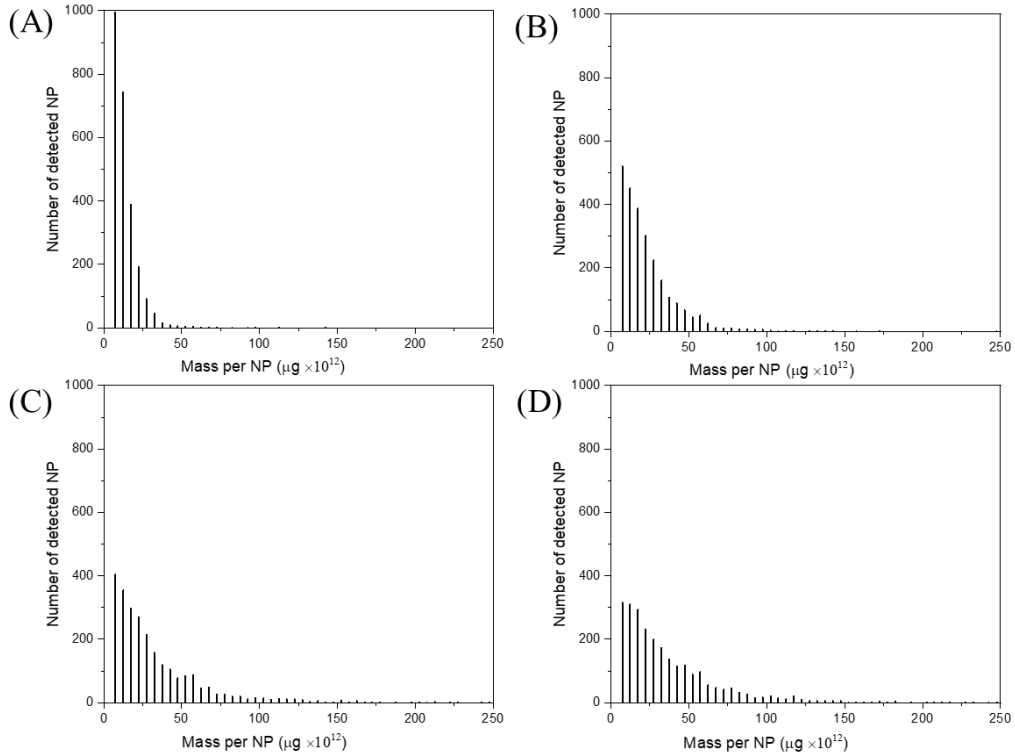

Figure 3.5. Distribution of measured Ru mass per NP generated by Ru-SiO_2 NPs with various doping levels in spICP-MS measurements. (A), 13.3 mM. (B), 26.7 mM. (C), 53.4 mM. (D), 106.8 mM. Bin size: 5. (^{102}Ru, dwell time 5 ms, 2500 individual nanoparticles)

For comparison, the measured per-particle Au mass distribution over 2500 number individual AuNPs was also obtained (Figure 3.6). Although there were significant numbers of split-particle events because of the short 5 ms dwell time used for these large 150 nm AuNPs, the broad Gaussian-like distribution of measured per-particle Au mass indicated a consistent concentration of Au per NP. This is the expected result for single-component MCPs with consistent size because metal concentration per particle is simply governed by the physical density (mass per unit volume) of the metal component, which is constant from particle-to-particle.

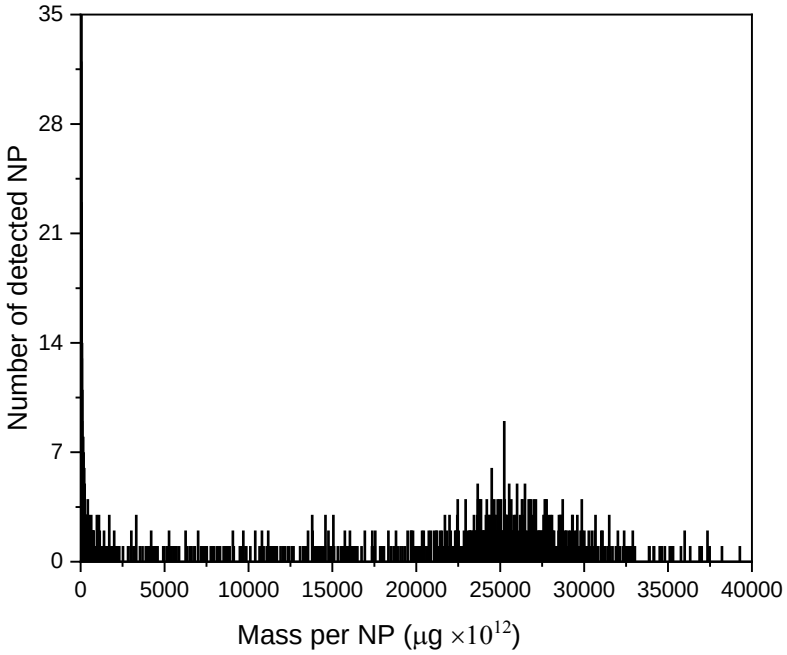

Figure 3.6. Distribution of measured Au mass per NP generated by AuNPs in spICP-MS measurements. Bin size: 5. (^{197}Au, dwell time 5 ms, 2500 individual nanoparticles)

The unusual geometric distribution of Ru mass per NP for the Ru-SiO_2 NPs and lack of any Gaussian-like feature could only occur from inhomogeneity of the NP size or inhomogeneity of Ru content per NP. To probe whether inhomogeneity in NP size was the cause, distribution histograms of theoretical metal mass per NP were determined from actual TEM measurements of NP diameter for both AuNP and Ru-SiO_2 NP samples (see section 3.2.5). The distribution of measured Au NP sizes (Figure 3.7A), when converted to theoretical Au mass per NP by assuming a gold density of [19.3 g/cm^3] per NP (Figure 3.7B), shows an obvious Gaussian-like feature that is a good match to the Gaussian distribution measured by spICP-MS (Figure 3.6). Likewise, the distributions of measured Ru-SiO_2 NP sizes (Figure 3.8A-D), when converted to theoretical Ru mass per NP by assuming the given Ru doping concentration per NP (Figure 3.8E-H), also show a

Gaussian-like feature for all Ru doping levels. However, these size-based Gaussian distribution clearly do not match to the geometric distributions measured by spICP-MS (Figure 3.5A-D) and clearly demonstrate that geometric distributions of Ru mass measured by spICP-MS are not the result of NP size variation.

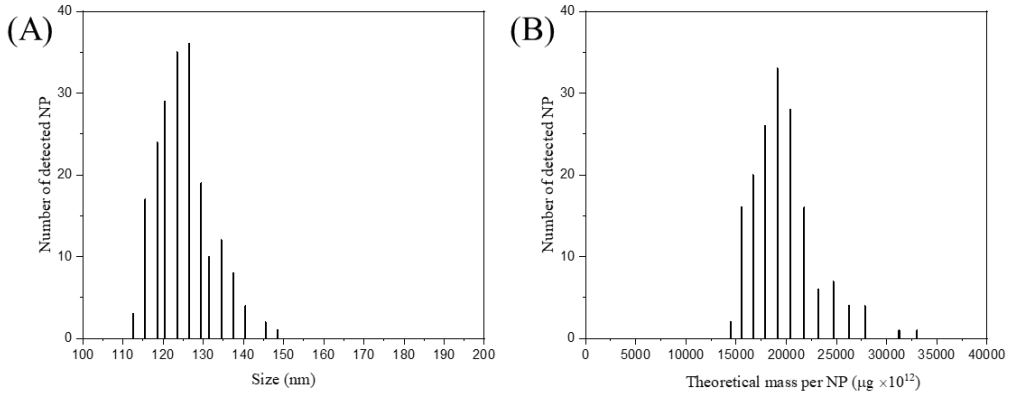

Figure 3.7. Distribution of size (A, bin size:1) and theoretical per-particle Au mass (B, bin size: 5) of AuNPs by TEM. (200 number individual particles)

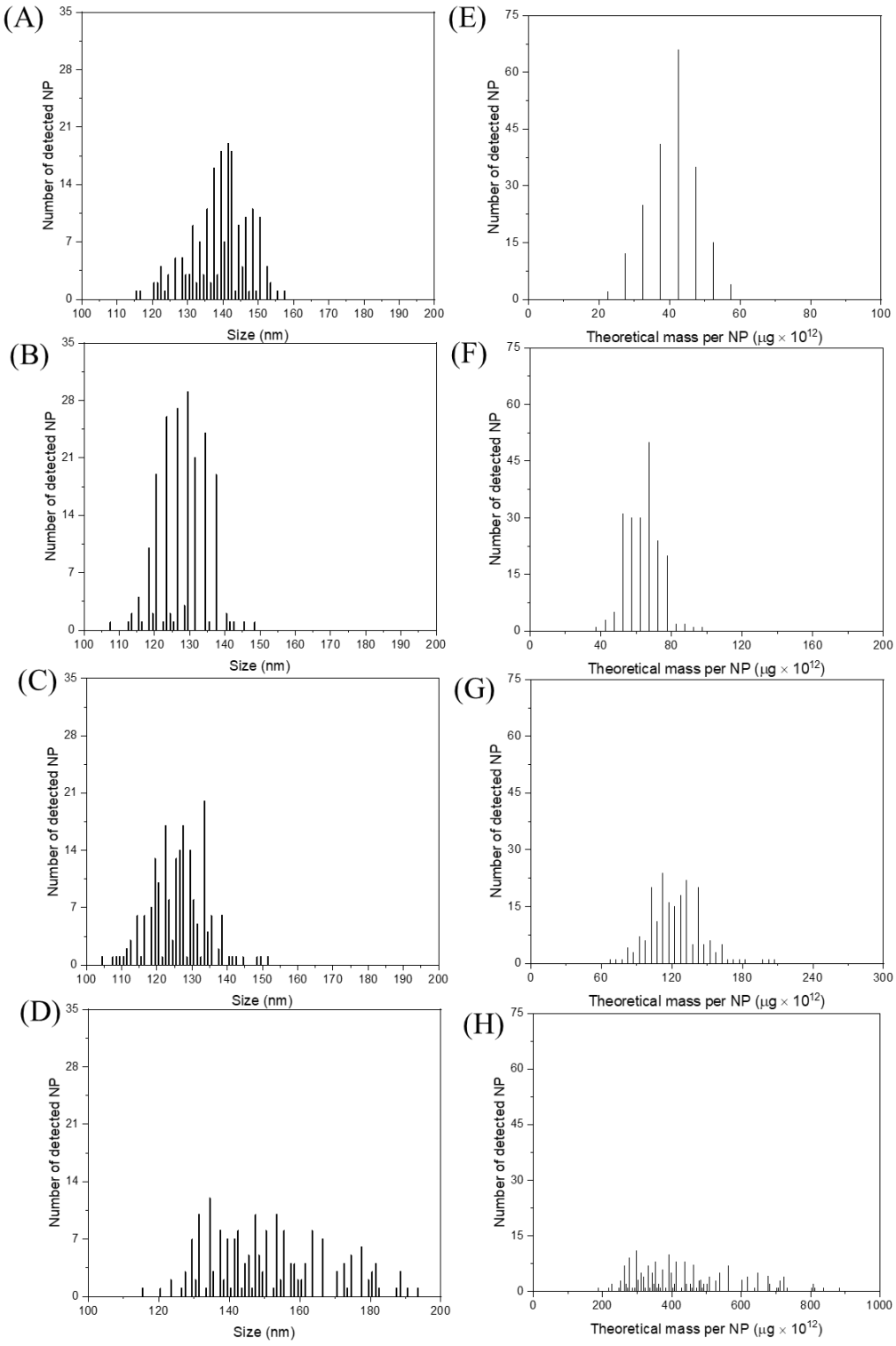

Figure 3.8. Distribution of size (A-D, bin size:1) and theoretical per-particle Ru mass (E-H, bin size: 5) of Ru-SiO_2 NPs with varied doping levels by TEM. (A) and (E), 13.3 mM. (B) and (F), 26.7 mM. (C) and (G), 53.4 mM. (D) and (H), 106.8 mM. (200 number

individual particles)

By eliminating NP size variation as a factor in the unusual geometric distribution of Ru mass measured by spICP-MS, the most likely cause appears to be Ru doping variations. Up to now, the synthesis of metal-doped SiO_2 NPs using the water-in-oil microemulsion method is usually assumed to produce NPs with a consistent metal-doping concentration per particle. This is because the water solution used to form the microemulsion has a homogenous concentration of metal dopant and it is assumed that this same homogenous concentration is carried into the dynamic nanodroplet micelles that comprise microemulsion prior to addition of the silica-forming reagent, TEOS. However, some literature has suggested that the rapid intermicellar exchange of dopant in dynamic nanodroplet micelles can lead to inhomogeneous distributions if the dopant undergoes precipitation.[109, 110] Factors that favor the formation inhomogeneous distributions of dopant within particular micelles are kinetic in nature; specifically, fast intermicellar exchange of dissolved dopant paired with relatively slow precipitate nucleation compared to growth. Under these conditions, the few micelles that manage to nucleate a dopant precipitate tend to accumulate even more dopant from the many adjacent micelles that have no precipitate. This mechanism leads to many micelles with much less dopant than the initial concentration and a small number with a large amount of accumulated dopant precipitate. Because the dopant distribution predicted for this mechanism is a same geometric distribution of Ru mass measured by spICP-MS, this mechanism is probably active in the synthesis of Ru-SiO_2 NPs. This conclusion is supported by additional observations that relatively high concentrations of $[Ru(bpy)_3]^{2+}$ dopant solution were used to make these NPs (10–100 mM), the $[Ru(bpy)_3]Cl_2$ dopant has a limited solubility of 1 %

(0.013 moles/L) in water solutions to begin with. And the dopant solubility is probably even lower within the nanodroplet micelles because of the water-in-oil environment.

3.3.5. Comparison of spICP-MS analysis results of Ru-SiO_2 NPs with bulk methods

Routine characterization of multicomponent MCPs has traditionally been carried out by bulk-analysis methods such as UV-visible absorption or fluorescence spectroscopy measurements or by conventional ICP-MS measurements. These are considered 'bulk-analysis' methods because the measurement signals are produced by many NPs at the same time. They also produce a signal that is an average for all of the individual NPs sampled in the measurement cycle. Although this work has demonstrated that a particle-by-particle analysis method like spICP-MS provides a powerful new and useful prospective to MCP characterization, it was also important to see whether the unusual, inhomogeneous metal composition of Ru-SiO_2 NPs was somehow evident at all from the traditional bulk-analysis methods or whether averaging the particle-by-particle measurements simply produces the same analysis results as the bulk methods.

To make these comparisons, the *average* number of Ru atoms per NP of Ru-SiO_2 NPs were determined for each $[Ru(bpy)_3]^{2+}$ doping level and for each type of method; spICP-MS and the bulk analysis methods of UV-vis absorbance spectroscopy and conventional ICP-MS (see section 3.2.6). Figure 3.9 compares these averages for the dopant concentrations of 13.3 mM to 106.8 mM. The *average* number of Ru atoms per NP of Ru-SiO_2 NPs determined by spICP-MS and bulk analysis methods kept a good agreement, indicating an accurate measurement of spICP-MS in the per-particle metal content over a sufficiently population of particles. Moreover, the red line plotted in Figure 3.9 shows a linear relationship between the *average* Ru content per NP of Ru-SiO_2 NPs by

all three of the methods and the amounts of $[Ru(bpy)_3]^{2+}$ added in the synthesis was observed, when the concentration of added $[Ru(bpy)_3]^{2+}$ was below 26.7 mM. When the amounts of $[Ru(bpy)_3]^{2+}$ mixed in the synthesis increased from 26.7 mM to 106.8 mM, the falling off *average* Ru content per NP of Ru-SiO_2 NPs indicates the per-particle metal content of Ru-SiO_2 NPs increased disproportionately with the increase of $[Ru(bpy)_3]^{2+}$ addition concentration and more $[Ru(bpy)_3]^{2+}$ molecules were left in the solution.

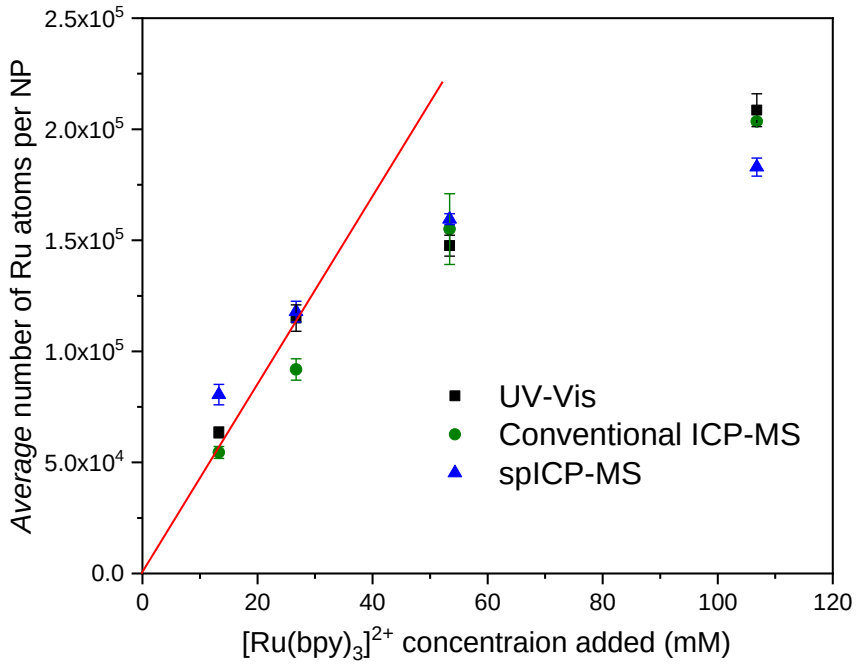

Figure 3.9. Relationship between the *average* number of Ru atoms per NP in the Ru-SiO_2 NPs and the concentration of $[Ru(bpy)_3]^{2+}$ solution added in the nanoparticle synthesis by spICP-MS (Blue color with triangle shape), UV-Vis (Black color with rectangle shape), and conventional ICP-MS (Green color with circle shape).

3.4. Conclusions

This chapter has demonstrated the use of spICP-MS to determine the per-particle metal composition of a model MCP that possesses a challenging multicomponent matrix. This MCP—silica nanoparticles doped with varying amounts of $[Ru(bpy)_3]^{2+}$ (Ru-SiO_2

NPs) and prepared by the water-in-oil micro-emulsion method—has been standard NP model used in many studies and up to now has been considered a very well-understood nanomaterial. However, the most important finding of this work is the highly unusual and inhomogeneous distribution of metal content identified in these Ru-SiO_2 NPs—which up to now was assumed to be homogeneous. One reason why these MCPs have been considered so normal and homogeneous in metal content was a built-in bias of the bulk-analysis methods used for their characterization—methods such as UV-visible absorbance or fluorescent spectroscopy or conventional ICP-MS. These bulk methods, by their nature, can only determine an *average* metal content for the many individual NPs that produce the measurement signal. Only a particle-by-particle analysis method such as spICP-MS can identify inhomogeneity in NP metal content and this work clearly demonstrates that such as method should be added to the routine screening of any new MCP, especially one with more than one component. It may seem strange that a similar rationale has been applied for decades to justify the use of SEM and TEM for routine characterization of nanomaterials; i.e., use a particle-by-particle imaging method like TEM to identify inhomogeneity in NP size. However, it is only recently that sufficiently fast and sensitive analytical methods, such as spICP-MS, have become readily available for routine nanomaterial screening and characterization.

Another important finding in this work is the close correspondence observed between *average* metal content per NP determined by all three of the methods used to characterize various samples of Ru-SiO_2 NPs. This correspondence indicates that the spICP-MS method provides sufficiently accurate per-particle results that, when averaged for a sufficiently large number of particles, the result corresponds closely to the inherent

averages determined by the bulk-analysis methods of UV-visible absorption and conventional ICP-MS. These types of bulk-analysis methods should clearly still be part of any routine characterization of MCPs because their results are more easily measured than spICP-MS and their averages can still provide useful information about sample-to-sample reproducibility. However, their value to understanding metal content in MCPs should be confirmed using per-particle results provided by spICP-MS.

CHAPTER IV

A SANDWICH STRUCTURED (POLYMER DOTS-SILICA-GOLD NANOCLUSTERS) RATIOMETRIC FLUORESCENT NANOPROBE FOR ACCURATE AND SENSITIVE DETECTION OF COPPER IONS

4.1. Introduction

Gold nanoclusters (AuNCs) are ultra-small gold nanoparticles consisting of several to hundreds of Au atoms. Instead of the traditional light absorption of gold nanoparticles that is based on surface plasmon-resonance, AuNCs exhibit unique fluorescence emission in the visible/infrared regions due to their small size of ≤ 2 nm.[111-113] Owing to their favorable properties of low toxicity, good biocompatibility, and wide optical signaling range (from blue to near infrared),[114-116] AuNCs have been identified as a promising fluorescent probe for biosensing and bioimaging over other luminescent materials such as fluorescent proteins and semiconductor quantum dots.[117] Many different synthetic strategies for fluorescent AuNCs have been developed with different approaches so these materials can be utilized in biosensing and bioimaging. For instance, Luo et al. reported luminescent AuNCs prepared by chemical reduction using bovine serum albumin and sodium hydroxide. These AuNCs showed fluorescence "turn-off" signals for the detection of copper ions (Cu^{2+}).[118] In another example, Chen and co-workers synthesized AuNCs using cysteine as an etching agent through a "nanoparticle to cluster" route. The obtained AuNCs were used for the determination of Cu^{2+}, pyrophosphate, and alkaline phosphatase with quenching and recovering of fluorescence emission.[119]

A notable drawback to most AuNCs prepared to date is that fluorescence quantum yield is typically lower than 1 %.[120-122] This limitation has restricted their further applications in biosensing and bioimaging. Moreover, AuNCs provide only a single emission signal, which makes quantifications of a target analyte uncertain whenever

analyte-independent interferences occur, such as instrumental parameter variation, changes of microenvironment around the probe, and photobleaching[123, 124]. One way to overcome these problems and improve analysis reliability is to develop ratiometric fluorescent probes based on AuNCs that provide a second internal correction signal. Such a ratiometric fluorescence probe would greatly increase the sensitivity and accuracy for the quantification of analytes, especially for *in situ* biological sample matrixes that present calibration challenges.

To date, several efforts have been made to develop ratiometric fluorescent probes based on AuNCs, and these methods typically combine AuNCs by with a second luminescent nanomaterial such as carbon dots and organic dyes.[125-127] However, the toxicity of organic dyes and limited stability of carbon dots have restrained their performance for biosensing and bioimaging. To overcome these drawbacks, a better second fluorophore is needed to make ratiometric fluorescent probes based on AuNCs. One promising candidate is fluorescent conjugated polymer nanoparticles (CPNs) owing to their extraordinary brightness, low toxicity, and good stability.[128-130] For example, Feng and his co-workers[131] as well as Xu et al.[66] have provided overviews for the preparation, optical properties, functionalization, and biological applications of CPNs, but so far no literature has reported the combination of CPNs with AuNCs to make ratiometric fluorescent nanoproboes.

The nanoprobe assembled with AuNCs and CPNs in this study has a sandwich nanostructure that has two distinct fluorescence emission peaks at 438 nm and 630 nm. The shorter-wavelength fluorescence emission of the CPNs was designed as the internal calibration and correction signal, and the longer-wavelength fluorescence emission of the

AuNCs was designed to be responsive to target analyte, Cu^{2+}. Upon the addition of Cu^{2+}, the fluorescence emission at 630 nm is quenched because Cu^{2+} chelates with the carboxyl groups on the surface of AuNCs, while the emission of CPNs at 438 nm remains nearly constant. Thus, highly sensitive and selective ratiometric fluorescence determination of Cu^{2+} was successfully accomplished using the sandwich nanostructure. Furthermore, the feasibility of the nanostructure for *in vitro* imaging of Cu^{2+} was investigated. The results showed that the designed sandwich nanostructure endows their capability for sensing Cu^{2+} in both living cells and microenvironment.

4.2. Experimental Section

4.2.1. Materials

L-glutathione in the reduced form (GSH, >= 98.0 %), tetraethyl orthosilicate (TEOS, 99.999 %), ammonia hydroxide (28.0 % NH_3 in water), (3-aminopropyl) triethoxysilane (APTES, 99.0 %), polyoxyethylene glycol tert-octylphenyl ether (Triton X-100, BioXtra), *n*-hexanol (>= 99 %), cyclohexane (99.5 %), acetone (>= 99.9 %), ethanol (>= 99.5 %), polyethylenimine (PEI, MW 10,000, <=1 % in water,) , and 4-(2-hydroxyethyl)-1-piperazineethanesulfonic acid (HEPES, >=99.5 %), and penicillin-streptomycin (Bioreagent) were obtained from Sigma-Aldrich (St. Louis, MO, USA). Hydrogen tetrachloroaurate trihydrate ($HAuCl_4$, 99.99 %) was purchased from Alfa Aesar (Tewksbury, MA, USA). Polydioctylfluorence (PFO) was provided by Polymer Source Inc. (Quebec, Canada). 1,2-distearoyl-sn-glycero-3-phosphoethanolamine conjugated polyethylene glycol with active succinimidyl ester (DSPE-PEG-NHS, MW 3500) was obtained from Nanocs Inc. (New York, NY, USA). The HeLa cell line was provided by American Type Culture Collection (Manassas, VA, USA). Dulbecco's Modified Eagle

Medium and 8-well Chambered Coverglass w/ non-removable wells were purchased from Thermo Fisher Scientific (Waltham, MA, USA). Fetal bovine serum was purchased from Peak Serum (Wellington, CO, USA). Fluoromount-G® mounting medium was purchased from SouthernBiotech (Birmingham, AL, USA). CytoTox 96® Non-Radioactive Cytotoxicity Assay kit was purchased from Promega (Madison, WI, USA). Ultrapure Millipore water (18.2 MΩ•cm) was used for all experiments.

4.2.2. Instruments

A Hitachi 7500 Transmission Electron Microscope (Hitachi, Tokyo, Japan) was used at 80 kV to take images of the developed PFO@SiO_2@AuNCs. Confocal fluorescence imaging was conducted with an Olympus FV3000 Laser Scanning Confocal Microscope (Olympus, Tokyo, Japan). The Zeta potentials of the PFO@SiO_2, AuNCs, and PFO@SiO_2@AuNCs were measured using a Zetasizer Nano ZS (Marlwen, Worcestershire, UK). A PerkinElmer Lambda 1050 UV/VIS/NIR spectrometer (PerkinElmer, Santa Clara, CA, USA) was used to obtain absorption spectra of PFO@SiO_2, AuNCs, and PFO@SiO_2@AuNCs nanocomposites.

Time-resolved luminescence decay measurements were conducted using a Jobin Yvon Horiba Fluorolog-3 spectrofluorometer (Horiba, NJ, USA). Fluorescence signal and quantum yield measurements were performed on a RF-6000 fluorophotometer (SHIMADZU, Kyoto, Japan). The excitation wavelength was set to be 380 nm, and the fluorescence emission spectra were recorded from 405 nm to 720 nm. Both the width of excitation and emission slits were 10.0 nm. The fluorescence intensities at 438 nm and 630 nm were measured to evaluate sensitivity to the Cu^{2+} analyte concentration. Rhodamine 101 in ethanol with 0.01 % HCl was selected as the standard material (quantum yield=1.0

at 597 nm) in the relative quantum yield measurement of AuNCs. The refractive index of ethanol with 0.01 % HCl and HEPES solution is 1.36 and 1.33.[132]

4.2.3. Synthesis of PFO CPNs

Polydioctylfluorene conjugated polymers nanoparticles (PFO CPNs) were synthesized by a nanoprecipitation process. Briefly, 5.0 mg of PFO polymer was dispersed in 5.00 mL of THF to make a 1.0 mg/mL PFO stock solution. Meanwhile, a copolymer polyethylenimine was conjugated to 1,2-distearoyl-sn-glycero-3-phosphoethanolamine-N-[amino(polyethylene glycol)] (DSPE-PEG-PEI, 1.0 mg/mL) by addition of polyethylenimine (800 μL of 10 mg/mL) and 1,2-distearoyl-sn-glycero-3-phosphoethanolamine-N-[amino(polyethylene glycol)] (200 μL of 5.0 mg/mL) under constantly shaking for 12 h at room temperature. Then, 20 μL of 1.0 mg/mL of PFO stock solution and 200 μL of 1.0 mg/mL DSPE-PEG-PEI solution were mixed in 780 μL of THF solution. Afterwards, the mixture was quickly injected into 5.00 mL of ultrapure Millipore contained in an ice-bath and subjected to vigorous sonication for 2 min. Then, the THF was removed by heating the mixture at 80 ℃ under a flow of nitrogen gas for 15 min. The resultant aqueous solution PFO CPNs with a concentration of 3.5 μg/mL was used directly for subsequent preparations and characterization.

4.2.4. Synthesis of PFO@SiO_2

The composite nanoprobe platform, PFO@SiO_2, was prepared by the water-in-oil reverse-microemulsion method, but with a slight change from the literature procedure.[104] A 7.50 mL aliquot of cyclohexene, 1.80 mL of *n*-hexane, and 1.77 mL of Triton X-100 were mixed and stirred for 20 min to form the initial microemulsion. Addition of 480 μL of 3.5 μg/mL of PFO CPNs under stirring for 20 min doped the reference fluorophore into

the nanodroplets of the microemulsion. Subsequent additions of 100 μL TEOS and 100 μL NH_4OH with stirring over a 20 min periodinitiated formation the silica nanoparticle matrix. After a 24 h reaction period under stirring, the PFO@SiO_2 nanoparticles were post-coated with -NH_2 groups on their surface by adding 4.0 μL of APTES to the stirred solution. After an additional 3 h reaction period, the amine functionalized PFO@SiO_2 nanoparticles were recovered by adding acetone to break the microemulsion and centrifuging at 10,000 rpm for 20 min. The as-prepared material was re-dispersed, washed three times with ethanol and three times with deionized water, and finally resuspended in water to a concentration of 7.5 mg/mL.

4.2.5. Synthesis of gold nanoclusters (AuNCs)

The synthesis of AuNCs was based on a reported method.[133] In a typical synthesis, $HAuCl_4$ (20 mM, 0.50 mL) and GSH (20 mM, 0.75 mL) were mixed with 3.75 mL of ultrapure water under vigorous stirring at 70 °C for 24 h. The AuNCs was formed and stored at 4 °C for the following experiments. The concentration of AuNCs stock solution was 1.5 mg/mL.

4.2.6. Sandwich nanostructure of PFO@SiO_2@AuNCs

The preparation of PFO@SiO_2@AuNCs sandwich nanocomposites was based on the electrostatic interaction of -NH_2 on the PFO@SiO_2 surface and -COOH on the Au NCs surface.[134] In general, 200 μL of 7.5 mg/mL of PFO@SiO_2 stock solution and 800 μL of 1.5 mg/mL of AuNCs solution were mixed overnight with vigorous stirring for. The PFO@SiO_2@AuNCs nanocomposites were formed and then collected by centrifugation at 10,000 rpm for 20 min. The PFO@SiO_2@AuNCs nanocomposites were washed with deionized water twice and re-dispersed in 1.00 mL of deionized water to a concentration

of 3.0 mg/mL.

4.2.7. Determination of Cu^{2+} in solution using PFO@SiO_2@AuNCs

To determine Cu^{2+} in solution, a 8.3 μL aliquot of 3.0 mg/mL PFO@SiO_2@AuNCs was added into 500 μL HEPES solution (10 mM, pH 7.0) containing different concentrations of Cu^{2+} ranging from 0.0 nM to 3000 nM. The mixture was incubated at room temperatures for 5 min. The fluorescence spectra were recorded from 405 nm to 720 nm with an excitation wavelength at 380 nm. The fluorescence intensity at 630 nm was recorded for detection of Cu^{2+}. Both the slits of excitation and emission were 10.0 nm.

4.2.8. *In vitro* monitoring of Cu^{2+} using PFO@SiO_2@AuNCs

HeLa cells were cultured in Dulbecco's Modified Eagle Medium with 10 % fetal bovine serum and 1 % penicillin-streptomycin, which were incubated in a cell incubator at 37 ℃ under 5 % CO_2. Cell viability in the presence of PFO@SiO_2@AuNCs was evaluated by using the CytoTox96® Non-Radioactive Cytotoxicity Assay. Briefly, aliquots of 50 μL of supernatant cells were placed in a 96-well plate and incubated overnight. Aliquots of 50 μL PFO@SiO_2@AuNCs solutions of varied concentration were added to make final concentrations of PFO@SiO_2@AuNCs (0-500 μg/mL) in the wells. After 24 h of incubation, aliquots of 50 μL of supernatant were transferred from wells to a new 96-well plate, followed by addition of 50 μL of CytoTox96® reagent. After further incubation for 30 min, 50 μL of Stop Solution was added in the mixture. The UV-Vis absorbance of the solution at 490 nm was measured using a multimode plate reader. The cell culture medium background was subtracted from absorbance values of all experimental wells. The cell viability was calculated through a serial data process in Microsoft Excel.

To monitor Cu^{2+} in living cells using PFO@SiO_2@AuNCs, HeLa cells were placed

in an 8-well cell culture slide. After incubation overnight at 37 ℃, a 200 μL aliquot of 1000 μM of Cu^{2+} solution was added to the wells and incubated for 4 h. Afterwards the cells were washed with 1 ×PBS to remove excess Cu^{2+} remaining in solution. Then 200 μL of 50 μg/mL of PFO@SiO_2@AuNCs sandwich nanoprobes were added into wells. After 3 h of incubation, the cells were washed with 1 ×PBS. The fluorescence confocal imaging was processed using an Olympus FV3000 Laser Scanning Confocal Microscope with an excitation wavelength of 405 nm and emission wavelength ranges of 400-500 nm and 600 -700 nm. The ImageJ program was used to collect the pixel intensity per cell from images.

4.3. Results and Discussion

4.3.1. Design of AuNCs-based sandwich structured ratiometric fluorescent probe

The low fluorescence quantum yield of AuNCs results in a low fluorescence signal that limits sensitivity and reliability when they are used as a fluorescent probe for sensing and imaging analytes. To overcome these challenges in our design, instead of detecting AuNCs by an absolute fluorescence signal, we employed a ratiometric assay by measuring the decrease of AuNCs fluorescence signal in comparison to a constant signal from an internal reference fluorophore. In this way, small changes in the AuNC signal could be reliably calibrated to achieve sensitive determination of trace amounts of target analytes. Key to this design is the internal reference fluorophore which ensures measurement accuracy by proving a consistent refence signal. Therefore, the selection of a suitable reference fluorescence probe is critical for achieving the goal. Excellent photostability and strong fluorescence are the two most important characteristics required for the reference fluorophore. In this regard, conjugated polymer nanoparticles (CPNs) are a strong choice due to their high brightness, excellent photostability, low toxicity, and good

biocompatibility. The third consideration in selection of the specific conjugated polymer should be that its excitation wavelength matches that of AuNCs to obtain high and easily resolved emission signals for each fluorophore. We found out that the polydioctylfluorene (PFO) polymers provide a suitable excitation wavelength. Thus, as shown in Scheme 4.1A, PFO was selected as our starting material for making CPNs (Scheme 4.1A, a).

Another important factor in this nanoprobe design is having a consistent shape and size of the internal reference fluorophore. To better form a spherical-shaped conjugated polydioctylfluorene nanoparticles (PFO CPNs), an amphiphilic block copolymer was needed to change the solvent polarity. Thus, DSPE-PEG-PEI was selected as a co-polymer to assist in the formation of CPNs (Scheme 4.1A, b). As described in section 2.3, DSPE-PEG-PEI and PFO together formed a PFO CPN (Scheme 4.1A, c), which could be used as the reference fluorophore for AuNCs.

Yet another important factor in this nanoprobe design is to limit photobleaching resulting from the energy transfer between PFO and AuNCs. This photobleaching can be avoided by incorporating a spacer between PFO and AuNCs. Because silica nanoparticles (SiO_2) have numerous advances as a spacer material, such as controllable size and easy functionalization, silica was selected as the spacer material and the PFO CPNs were encapsulated inside silica nanoparticles (PFO@SiO_2) (Scheme 4.1A, d). Further, the SiO_2 shell was modified with amine groups for assembling AuNCs. Because -COOH groups on AuNCs surface electrostatically bind with -NH_2 groups on silica surface, a sandwich structure of PFO@SiO_2@AuNCs is formed as the ratiometric fluorescent nanoprobe (Scheme 4.1A, e). This nanoprobe emits at two distinct wavelengths (438 nm and 630 nm) when excited at only wavelength of 380 nm. The ratiometric fluorescent

nanoprobe can be used for the detection of Cu^{2+} as shown in Scheme 4.1B. With the addition of Cu^{2+}, the fluorescence signal of PFO@SiO_2@AuNCs at 630 nm is quickly quenched by coordination between Cu^{2+} and the carboxyl group on the AuNCs, but the emission intensity at 438 nm remains essentially constant. The ratio of the fluorescence intensities of 438 to 630 nm without Cu^{2+} is considered the blank reading, $(I_{438}/I_{630})_0 = F_0$, while ratio of the fluorescence intensities of 438 to 630 nm with Cu^{2+} present, $I_{438}/I_{630} = F$, reflects the quenched reading. By calibrating a ratio of these two readings, $((F - F_0)/F_0)$, to the concentration of Cu^{2+}, the proposed ratiometric fluorescent nanoprobe exhibits excellent sensitivity for the rapid detection of Cu^{2+}. Furthermore, the feasibility of PFO@SiO_2@AuNCs for *in vitro* imaging of Cu^{2+} can be investigated.

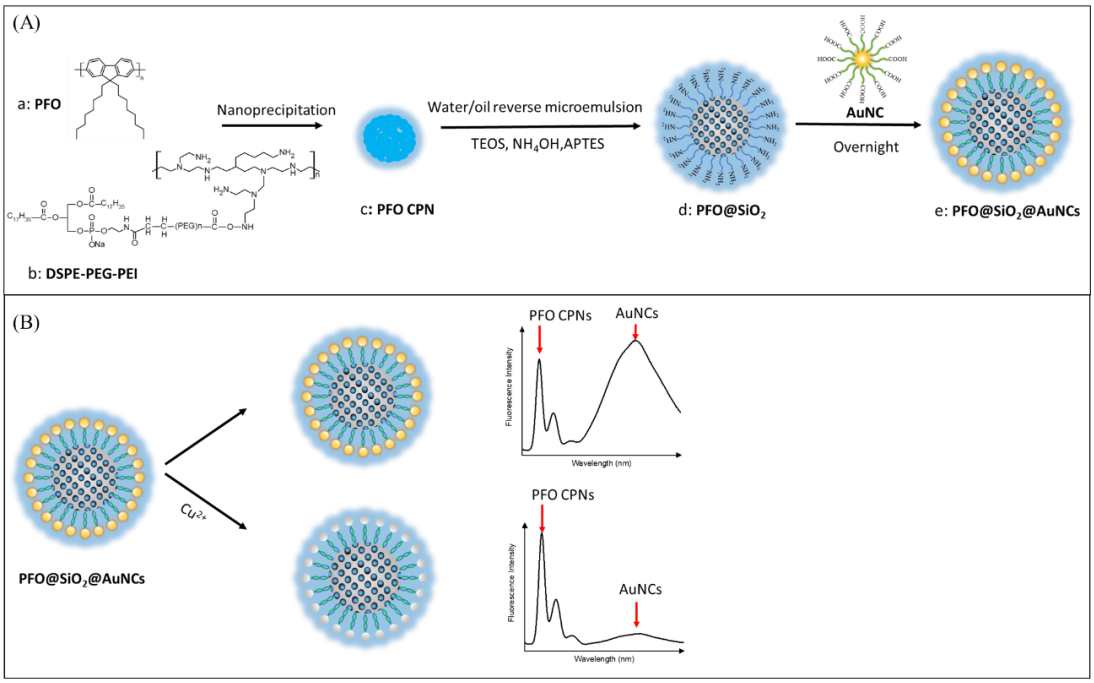

Scheme 4.1. Schematic illustration of (A) the synthesis of PFO@SiO_2@AuNCs and (B) its application for the detection of Cu^{2+}.

4.3.2. Synthesis of sandwich structured PFO@SiO_2@AuNCs

The AuNCs typically have surface -COOH groups due to the specific adsorption of GSH molecules. It was expected that the AuNCs would show negative charge under conditions of neutral solution pH. Meanwhile, the PFO@SiO_2 was post-coated with -NH_2 groups, resulting in a positive surface charge of PFO@SiO_2 under conditions of neutral solution pH. Therefore, we constructed the sandwich structure of the PFO@SiO_2@AuNCs by combining these two nanomaterials through the electrostatic interaction. After purification of PFO@SiO_2@AuNCs, the Zeta potential was measured to determine the surface charge of PFO@SiO_2@AuNCs prepared at various mass ratio of PFO@SiO_2 to AuNCs (Figure 4.1). With increasing amount of AuNCs, the Zeta potential value of PFO@SiO_2@AuNCs decreased. When the mass ratio of PFO@SiO_2 to AuNCs was 1:0.032, the Zeta potential was close to zero, indicating the occurrence of charge-charge interactions between the two oppositely charged nanomaterials and a consequence of the sandwich structured PFO@SiO_2@AuNCs formation. As the ratio of PFO@SiO_2 to AuNCs increased above 1:0.032, the Zeta potential shifted to more negative. These results indicated more AuNCs were interacted with the PFO@SiO_2 to make the PFO@SiO_2@AuNCs.

Determination of analyte was designed to rely on the fluorescence intensity change of AuNCs, which is a “turn-off” process. To achieve a higher detection sensitivity, the mass ratio of PFO@SiO_2 to AuNCs was further optimized to obtain the highest fluorescence intensity ratio of I_{630}/I_{438}. The fluorescence measurements of the PFO@SiO_2@AuNCs were carried out and their fluorescence intensity ratio was measured (Figure 4.2). With the ratio of PFO@SiO_2 to AuNCs increased, the fluorescence intensity ratio increased and then reached a plateau with slight changes afterwards at 1:0.9 of

PFO@SiO_2 to AuNCs. Therefore, the ratio of PFO@SiO_2 to AuNCs was selected at 1: 0.9 during the synthesis of the PFO@SiO_2@AuNCs nanoprobe.

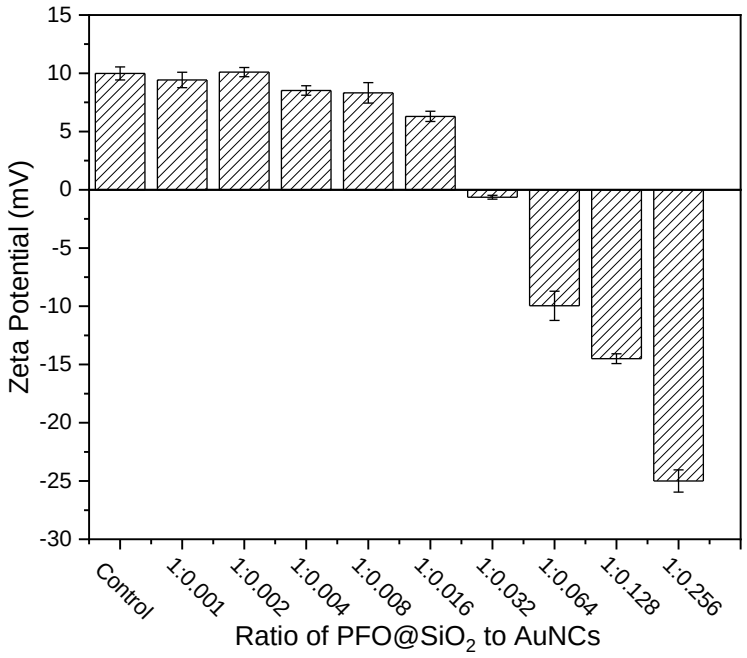

Figure 4.1. Zeta potential measurements of PFO@SiO_2 @AuNCs prepared at different mass ratio of PFO@SiO_2 to AuNCs in 10.0 mM, pH 7.0 HEPES solution. Control: without AuNCs.

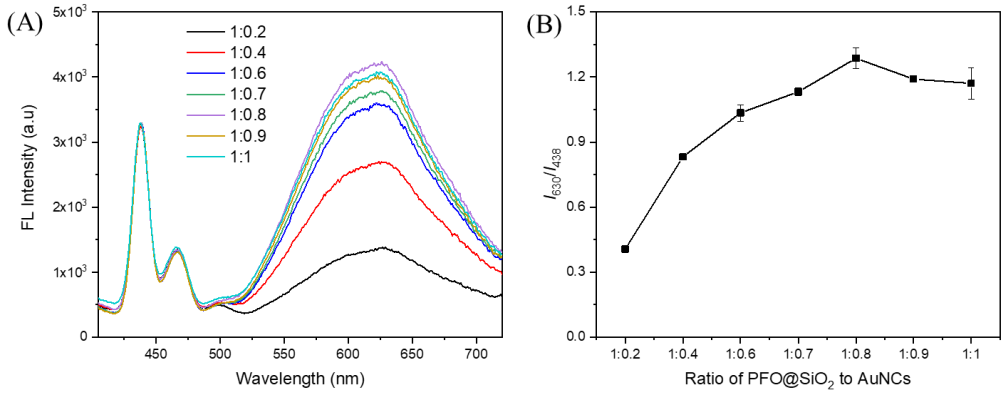

Figure 4.2. (A) Fluorescence spectra and (B) fluorescence intensity ratio (I_{630}/I_{438}) of PFO@SiO_2 @AuNCs prepared with different mass ratio of PFO@SiO_2 to AuNCs. λ_{ex} = 380 nm, $\lambda_{em\text{-}1}$ = 438 nm, $\lambda_{em\text{-}2}$ = 630 nm.

4.3.3. Characterization of sandwich structured PFO@SiO_2@AuNCs

4.3.3.1. Morphology of the nanoprobe

The morphology and size of AuNCs, PFO@SiO_2, and PFO@SiO_2@AuNCs were characterized using HRTEM and TEM (Figure 4.3). The AuNCs with a diameter of 2.0 ± 0.4 nm, spherical PFO@SiO_2 with a diameter of 58 ± 4 nm (Figure 4.3A) and PFO@SiO_2@AuNCs with a diameter of 61 ± 5 nm were observed when 200 individual nanoparticles were measured. The TEM images of PFO@SiO_2 and PFO@SiO_2@AuNCs were compared. Small dots of AuNCs were found on the surface of PFO@SiO_2@AuNCs (Figure 4.3C).

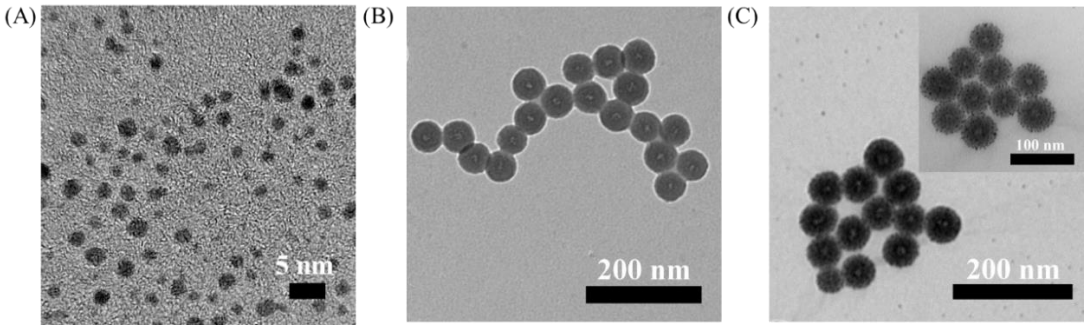

Figure 4.3. HRTEM image of (A) AuNCs and TEM images of (B) PFO@SiO_2 and (C) PFO@SiO_2@AuNCs. Insert is the TEM image of PFO@SiO_2@AuNCs with a scale bar of 100 nm.

4.3.3.2. Fluorescence property of PFO CPNs, PFO@SiO_2, and AuNCs

To investigate the optical property of the PFO CPNs and PFO@SiO_2, the fluorescence emission and excitation spectra of PFO CPNs and PFO@SiO_2 were obtained (Figure 4.4). The excitation spectrum of PFO CPNs exhibited a strong absorption at 380 nm wavelength. With the excitation wavelength at 380 nm, the transparent PFO CPNs showed a blue fluorescence emission peak at 438 nm. These features were consistent with characteristics reported in the literature[135] and demonstrated that the PFO CPNs were successfully prepared by the nanoprecipitation method.

To ensure the stability of PFO CPNs as a reference fluorophore, the PFO CPNs were encapsulated by the silica nanoparticles with water in oil reverse microemulsion method. The core shell structure of PFO@SiO_2 also showed a blue emission peak at 438 nm wavelength due to the existence of PFO CPNs in the silica nanoparticles.

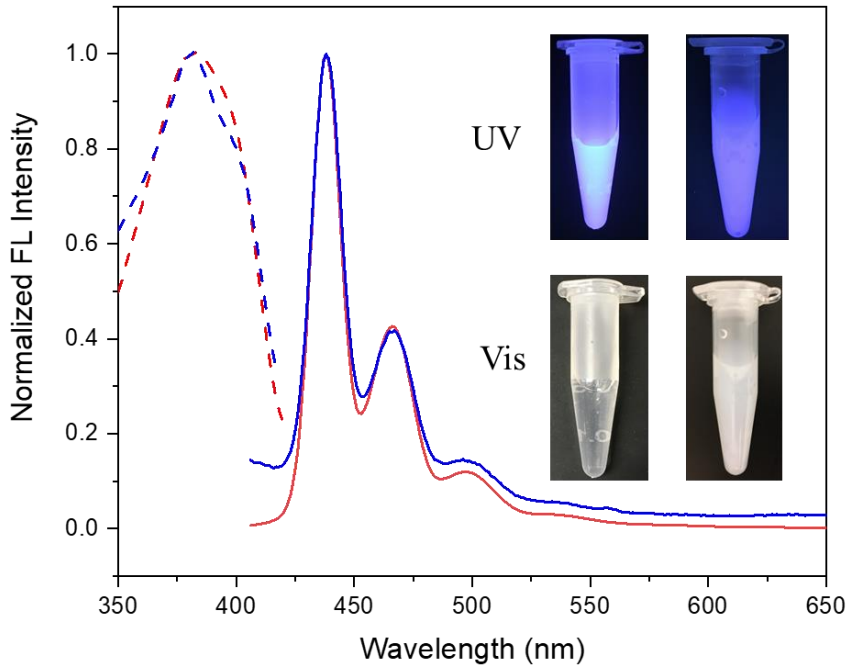

Figure 4.4. Fluorescence excitation (dashed line) and emission (solid line) spectra of (A) 0.5 μg/mL PFO CPNs (red color) and (B) 30 μg/mL PFO@SiO_2 (blue color) in 10 .0 mM, pH 7.0 HEPES solution. (λ_{ex} = 380 nm, λ_{em} = 438 nm). Insert is photographs of PFO CPNs (left side) and PFO@SiO_2 (right side) excited under 365 nm UV light (UV, top) and visible light (Vis, down).

We also investigated the fluorescence property of pure AuNCs (Figure 4.5). These AuNCs exhibited a typical broad absorption at around 380 nm wavelength and a broad emission peak at 630 nm, in the red end of the vosible spectrim. The results were also consistent with literature results with AuNCs syntheized with GSH.[136, 137]

To evaluate the colloidal stability of synthesized AuNCs, the fluorescence intensity of AuNCs at 630 nm under different solution pH values and saline (NaCl) concentrations were examined (Figure 4.6). The fluorescence intensity of AuNCs gradually increased when the pH increased to 6 and did not change much above pH 6 (Figure 4.6A). In addition, the fluoresence intensity of AuNCs exposed to various concentraions of NaCl (Figure 4.6B) showed very little change, demonstrating that salt concentration had little impact on the fluorescence intensity of AuNCs below an ionic strengths of 0.50 M. These results showed that the prepared AuNCs had good pH and saline stability; well within the normal biological range. They also demonstrated why AuNCs are promising fluorescent nanomaterials for bioanalysis and bioimaging.

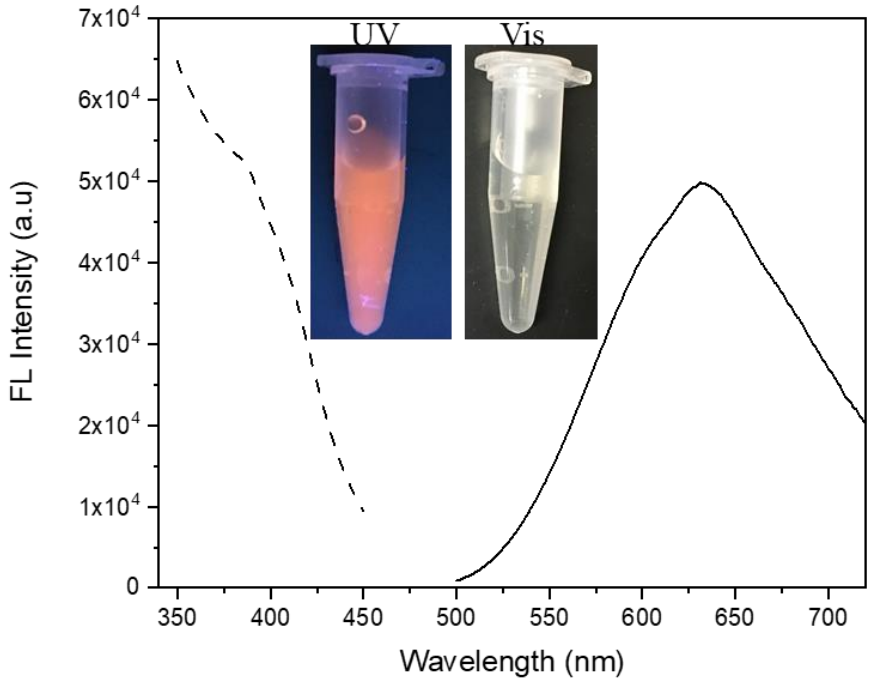

Figure 4.5. Fluorescence emission (solid line) and excitation (dashed line) spectra of 0.5 mg/mL of pure AuNCs in 10 .0 mM, pH 7.0 HEPES solution. λ_{ex} = 380 nm, λ_{em} = 630 nm. Insert is photographs of pure AuNCs solution excited under 365 nm UV light (UV) and visible light (Vis).

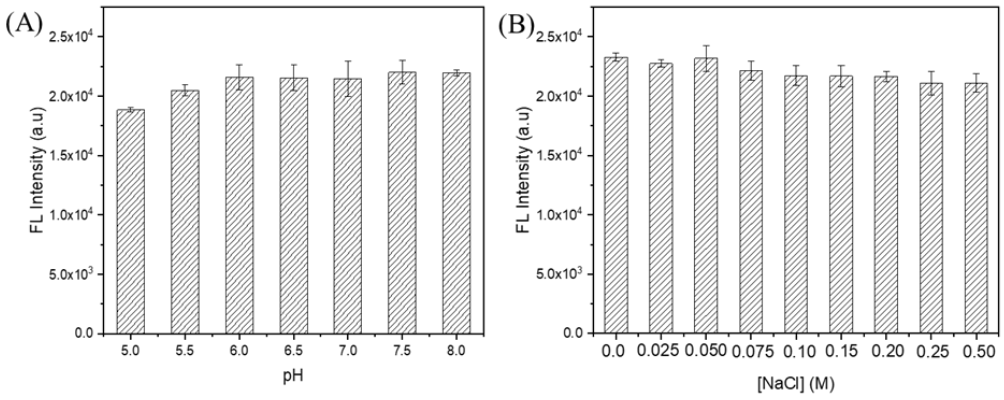

Figure 4.6. (A) Effects of pH on the fluorescence intensity of AuNCs. (B) Effects of ionic strength on the fluorescence intensity of AuNCs. AuNCs: 0.2 mg/mL, λ_{ex} = 380 nm, λ_{em} = 630 nm.

4.3.3.3. Effectiveness of the silica spacer in the nanoprobe

In the nanoprobe design, a silica spacer was placed between the PFO@SiO_2 and AuNCs to avoid Förster resonance energy transfer. To exam the effectiveness of the silica spacer, the time-resolved luminescence decays of PFO@SiO_2 and PFO@SiO_2@AuNCs with emission peak at 438 nm were measured (Figure 4.7). The lifetime for PFO@SiO_2 without AuNCs and PFO@SiO_2@AuNCs made with two different amounts of AuNCs were determined by fitting the curves with one exponential decay function, resulting in average lifetimes 0.15 ± 0.01, 0.15 ± 0.01, and 0.15 ± 0.08 ns. No significant difference was observed between the lifetime of PFO@SiO_2 without AuNCs and PFO@SiO_2@AuNCs made with AuNCs. Therefore, there was no Förster resonance energy transfer occurred in the assembled PFO@SiO_2@AuNCs.

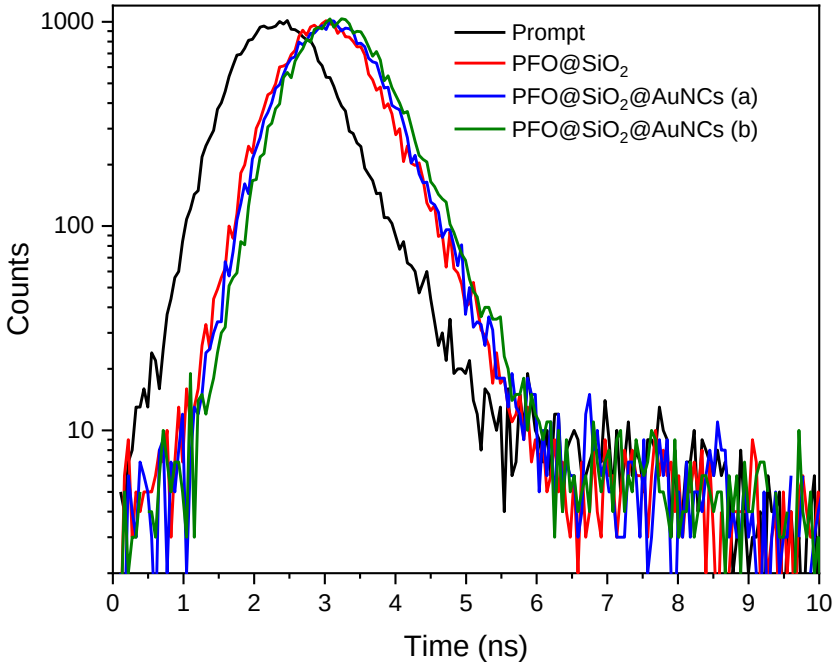

Figure 4.7. Time-resolved luminescence decays of PFO@SiO_2 and PFO @ SiO_2 @ AuNCs assembled with two different ratios of PFO @ SiO_2 to AuNCs (a,1:0.064; b,1:0.128). λ_{ex} = 380 nm, λ_{em} = 438 nm.

4.3.4. Cu^{2+} detection using PFO@SiO_2@AuNCs

Copper ion (Cu^{2+}) plays pivotal role in many biochemical and physiological processes. It is involved in the functions of organs and metabolic.[138, 139] However, both the overload and deficiency of Cu^{2+} can happen in biological systems. These syndromes can cause damage of biological organs and neurologic disorders, such as cancer,[140] Menkes disease,[141] and Wilson's disease.[142] To establish safety guidelines for the public, the United States Environmental Protection Agency (EPA) has set a maximum contaminate level for Cu^{2+} in drinking water at 20 μM (1.3 mg L^{-1}).[143] To date, various analytical techniques have been developed to determine concentration of Cu^{2+}.[143-147] Among these reported methods, fluorescence spectroscopy has been considered a good one to detect Cu^{2+} due to

its low cost, simple operation, and limited sample treatment. Furthermore, to eliminate the environmental interference and improve the accuracy of measurement with luminescent method, ratiometric fluorescent sensors to detect Cu^{2+} have been designed. However, there are notable problems associated with this ratiometric probes such as high toxicity and poor stability. Therefore, it is worthwhile to develop a new ratiometric fluorescent strategy for the fast sensing and imaging Cu^{2+} in biological systems.

To achieve better detection of Cu^{2+} using the ratiometric PFO@SiO_2@AuNCs nanoprobe, the effect of pH, probe concentration, and the incubation time on the change of fluorescence intensity ratio $((F - F_0)/F_0)$ were each investigated (Figure 4.8). The fluorescence intensity ratio in the absence and presence of Cu^{2+} were expressed as $(I_{438}/I_{630})_0 = F_0$ and $(I_{438}/I_{630}) = F$, respectively. Optimum conditions for Cu^{2+} detection were established from the maximum value of the fluorescence intensity ratio. Figure 4.8A indicated the nanoprobe in the presence of 1000 nM Cu^{2+} had a slightly lower fluorescence intensity ratio value in the acidic condition (pH 5.0), while the fluorescence intensity ratio was essentially constant above a pH of 5.5. Therefore, to better detect the Cu^{2+} in a biological system, the detection of Cu^{2+} using PFO@SiO_2@AuNCs were programmed at neutral condition (pH 7.0).

Similarly, the fluorescence intensity ratio of PFO@SiO_2@AuNCs at different concentrations in the addition of 1000 nM Cu^{2+} was measured (Figure 4.8B). With increase the probe concentration from 5 μg/mL to 25 μg/mL, the fluorescence intensity ratio increased and then decreased when the probe concentration increased from 25 μg/mL to 100 μg/mL. A maximum fluorescence intensity ratio value was obtained at 25 μg/mL of

PFO@SiO_2@AuNCs, indicating the optimized probe concentration at 25 μg/mL was used for quantifying Cu^{2+} in the following experiments.

The reaction time between Cu^{2+} and nanoprobes was also investigated (Figure 4.8C). In addition of Cu^{2+}, the fluorescence intensity ratio rapidly increased within 1 min and then reached a plateau after 5 min. Because the GSH molecules on the surface of AuNPs contain -COOH groups and is a high affinity chelating agent towards Cu^{2+},[148] resulting in a quick response. A 5 min period was selected as the optimized incubation time in the following experiments.

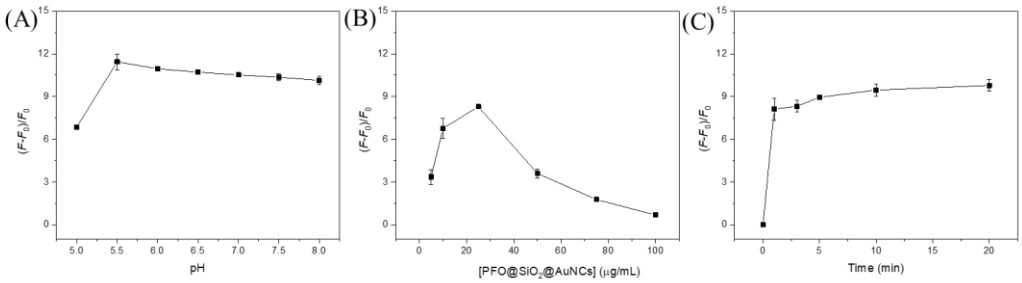

Figure 4.8. (A) Optimization of pH value in Cu^{2+} detection in 10 mM HEPES solution. (B) Optimization of concentration of PFO@SiO_2@AuNCs in Cu^{2+} detection. (C) Optimization of Cu^{2+} incubation time in PFO@SiO_2@AuNCs. Cu^{2+}: 1000.0 nM. λ_{ex} = 380 nm, λ_{em-1} = 438 nm, λ_{em-2} = 630 nm.

The sensitivity of ratiometric nanoprobe for Cu^{2+} detection was investigated under the optimized conditions. Various concentrations of Cu^{2+} were incubated with 25 μg/mL of PFO@SiO_2@AuNCs in pH 7.0, 10 mM HEPES solution for 5 min, followed by the detection of their fluorescence intensity (Figure 4.9A). With increased concentrations of Cu^{2+} from 0.0 nM to 3,000 nM, the emission peak located at 438 nm remained unchanged, while the fluorescence signal at 630 nm was quickly quenched due to the coordination between Cu^{2+} and carboxyl coated AuNCs.[148, 149] The fluorescence intensity ratio were determined in Figure 10B. The dynamic range was from 0.0 nM to 3000 nM, with a linear

relationship between 0.0 nM to 200 nM (Figure 4.9B insert) and a correction coefficient of 0.993. The limit of detection was calculated to be 10.5 nM by the 3σ rule, where σ is the standard deviation of three blank signals. These results indicated the designed dual-emission nanoprobe is better and comparable with most of those works for sensing Cu^{2+}.[134, 148, 150]

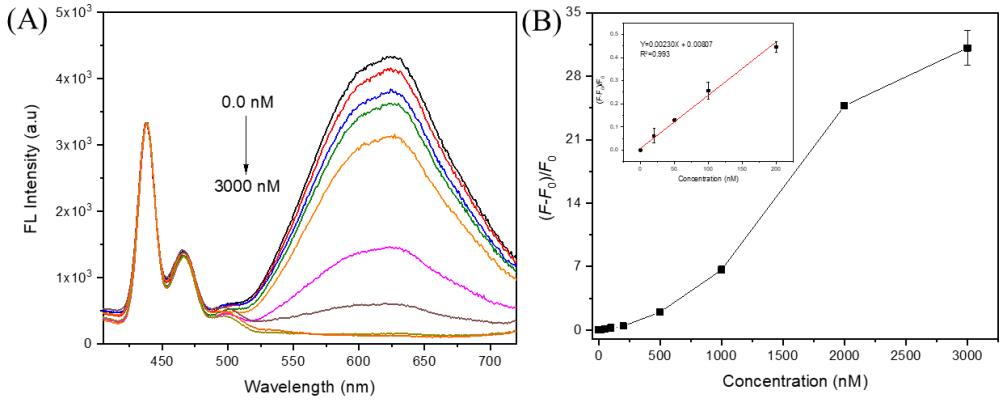

Figure 4.9. (A) Fluorescence spectra and (B) plot of related fluorescence intensity ratio of 25 μg/mL PFO@SiO_2@AuNCs with addition of different concentrations of Cu^{2+} ranging from 0.0 nM to 3000 nM. λ_{ex} = 380 nm, λ_{em-1} = 438 nm, λ_{em-2} = 630 nm.

4.3.5. Selectivity for Cu^{2+} detection

The selectivity of PFO@SiO_2@AuNCs for the screening Cu^{2+} was evaluated. Several common metal ions existing in biosystem were investigated under the same conditions with the ratiometric nanoprobe. As shown in Figure 4.10, a series of metal ions including Cu^{2+} at concentration of 1000 nM were incubated with PFO@SiO_2@AuNCs. The result showed the designed ratiometric probe possessed high selectivity toward Cu^{2+} while other metal ions had no change or slightly impact on the related fluorescence intensity ratio, which was expected by using the statement of the Irving-Williams serials that the primary chelation and presence of higher stability complex between -COOH groups and Cu^{2+} than interaction of -COOH groups with other transition metal ions and

other literature.[149, 151] Hence, the developed dual-emission nanoprobe had high sensitivity and excellent selectivity to monitor Cu^{2+}.

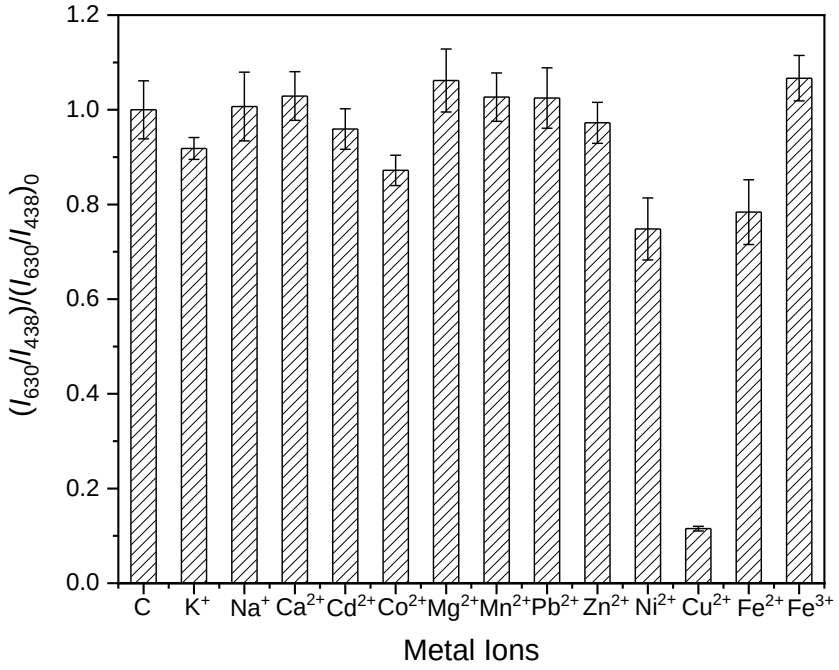

Figure 4.10. Selectivity investigation of the ratiometric probe for Cu^{2+} over other metal ions. C: control, without any mental ion. concentration of all metal ions are1000 nM. λ_{ex} = 380 nm, λ_{em-1} = 438 nm, λ_{em-2} = 630 nm.

4.3.6. *in vitro* imaging Cu^{2+}using PFO@SiO_2@AuNCs

To see if the PFO@SiO2@AuNCs nanoprobe could be used for *in vitro* imaging, we conducted a demonstration experiment of monitoring added Cu^{2+} in living cells. Before applying PFO@SiO_2@AuNCs to image Cu levels living cells, the cytotoxicity of the PFO@SiO_2@AuNCs to HeLa cells was investigated (Figure 4. 11). With increase the concentration of PFO@SiO_2@AuNCs, no obvious change in the viability of HeLa cells was observed in the range of 0 μg/mL to 500 μg/mL after incubation of 24 h. The results indicated that the PFO@SiO_2@AuNCs has low toxicity and excellent biocompatibility,

ensuring its applications in bioimaging and biosensing. Then, PFO@SiO_2@AuNCs were incubated with HeLa cells for 3 h and imaged by confocal fluorescence microscopy. As shown in Figure 4.12, the cells showed strong fluorescence signals of PFO@SiO_2@AuNCs. In comparison, the fluorescence intensity was significantly reduced in the cells in the presence of 1000 μM Cu^{2+}, indicating quenching of PFO@SiO_2@AuNCs by Cu^{2+}. The results demonstrated feasibility of screening of Cu^{2+} in *vitro*.

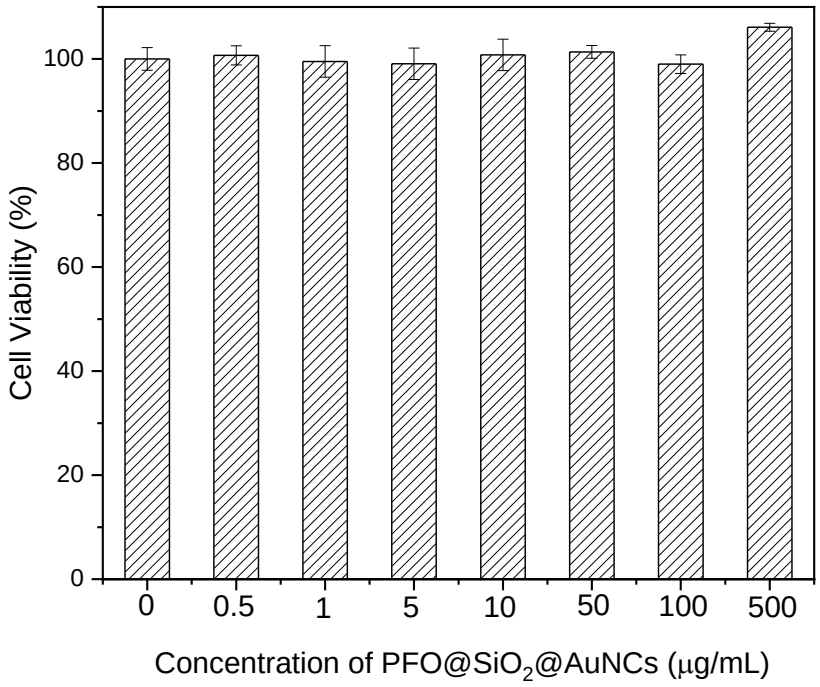

Figure 4.11. The viability of Hela cells incubated with varied concentrations of PFO@SiO_2@AuNCs ranging from 0 μg/mL to 500 μg/mL at 37 ℃ for 24 h.

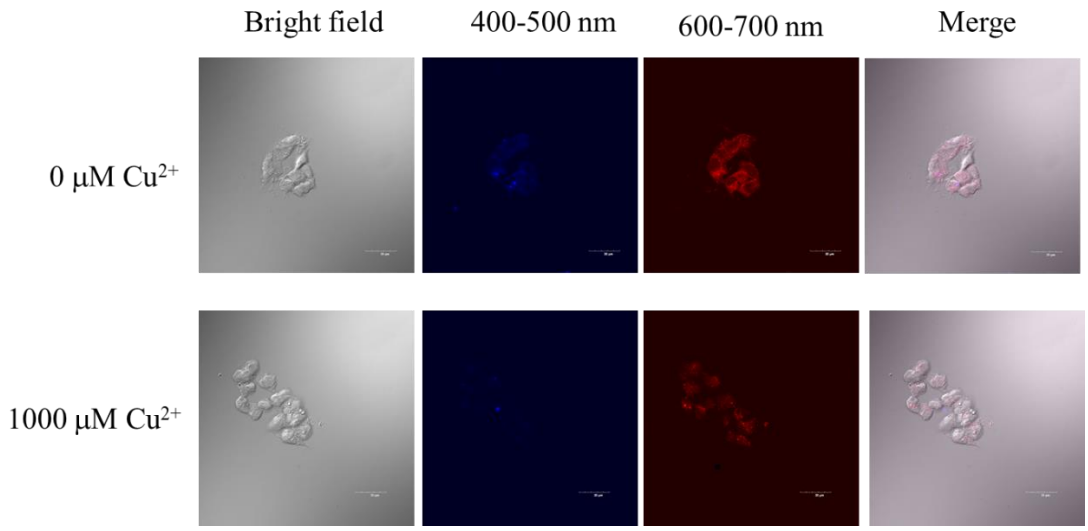

Figure 4.12. Fluorescence images of HeLa cells incubated with 50 μg/mL of PFO@SiO_2@AuNCs in the absence and presence of 1000 μM Cu^{2+} at 37 ℃ for 3 h. λ_{ex} = 405 nm, λ_{em-1} = 400-500 nm, λ_{em-2} = 600-700 nm. Scale bar: 50 μm.

4.4. Conclusions

In conclusion, by preparing a sandwich structure of ratiometric fluorescent probe PFO@SiO_2@AuNCs, we have developed a new strategy to determine Cu^{2+} based on the fluorescence quenching caused by the chelation between Cu^{2+} and -COOH groups on the AuNCs. The optimized assay provided a linear range from 0 nM to 500 nM and a detection limit of 10.5 nM. Moreover, the assembled PFO@SiO_2@AuNCs showed low cytotoxicity and excellent biocompatibility, providing feasibility for application of the sandwich structure in bioimaging of Cu^{2+} in living cells. Overall, this work offers important insights into the development of fluorescent AuNCs using CPNs, which may facilitate potential application of nanocluster materials to biosensing and bioimaging.

CHAPTER V

A FLUORESCENCE RESONANCE ENERGY TRANSFER BASED RATIOMETRIC NANOHYBRID USING GOLD NANOCLUSTERS AND CONJUGATED POLYMERS NANOPARTICLES FOR CYSTEINE DETECTION

5.1. Introduction

Gold nanoclusters (AuNCs) have attracted attention because of their excellent physicochemical properties, low toxicity, good biocompatibility, and stable luminescence.[152, 153] However, the negative surface charge of the initially synthesized nanoclusters and the short oligomeric motifs in the nanomaterial cause low fluorescence quantum yield which limits their application in biological systems.[154, 155] Three strategies have been developed to overcome these issues; capping the metal core surface with different types of ligands,[156] doping the core with other metal atoms,[157] and/or constructing hybrid nanoclusters that contain another fluorophore.[158, 159] Among these strategies, much work has been focused on construction of hybrid AuNCs that enhance quantum yield through the Frörster resonance energy transfer (FRET) between an energy donor and acceptor pair.[126, 160]

A number of fluorescence materials have been chosen as the FRET donor in hybrid AuNCs, including carbon dots[126, 134, 161, 162] and semiconductor quantum dots[163, 164]. However, application of these materials in biosensing has been constrained because of poor intrinsic properties, such as instability (carbon dots)[165] and cytotoxicity from release of heavy metal ions (semiconductor quantum dots).[166, 167]

An alternative FRET donor candidate without these drawbacks is the class of conjugated polymer nanoparticles (CPNs). These polymer nanoparticles are emerging as multifunctional fluorescent nanomaterials with good light-harvesting ability, low toxicity,

good stability, and excellent biocompatibility.[168, 169] For example, the Xu group has developed a highly stable CPN with resistance to organic solvents and used it as a multi-responsive (combined chemo/photothermal) cancer therapy agent with high therapeutic efficiency.[170] In another example, the Xiu group designed CPNs with a three donor-acceptor structure and used them as a photoacoustic contrast agent for brain vascular imaging.[171] The fast intra- and interchain energy transfer characteristic of CPNs also gives them great potential as a FRET donor for transferring energy to AuNCs;[172] however, no work has so far documented the enhanced quantum yield of hybrid AuNCs through FRET with CPNs.

Cysteine is an amino acid containing a thiol group and it plays significant roles in numerous biochemical and physiological processes.[173] Abnormal levels of cysteine can cause Parkinson's disease, skin damage, and hair discoloration, and can lead to stress and psychological disorders in humans.[174-176] Numerous methods have been developed to detect cysteine including spectrophotometry,[177] capillary electrophoresis,[178] and electrochemical methods.[179] Among these methods, fluorescence spectrophotometry offers significant advantages, including intrinsically high sensitivity, low instrument costs, fast response, and simple operation. Although the combination of these advantages with the noteworthy properties of AuNCs, such as low toxicity, low cost, broad spectral emission, good biocompatibility, and ease of conjugation might suggest that AuNCs are ideal probes for the determination of cysteine, many limitations have been reported. This main limitations for single-signal AuNC probes include poor accuracy and reliability due to the interference with the sample matrix. For multiple-signal AuNC, the limitations include

poor stability and high cytotoxicity resulting from a second fluorophore contained in the hybrid AuNCs.

To avoid problems associated with both the single- and multiple-signal AuNCs used to date for cystine determination, we have developed a class of FRET hybrid AuNCs containing chemically bound CPNs that also enhance quantum yield. In the nanohybrid, the CPNs were chosen as the FRET donor to transfer their energy to the as-prepared AuNCs. The AuNCs accept the energy and then emit a stronger fluorescence signal. When cysteine interacts with this FRET ratiometric fluorescence probe, the fluorescence emission at 630 nm from AuNCs is quenched due to changes to the gold core caused by formation of Au(I)-thiolate bonds. Simultaneously, the fluorescence emission at 385 nm from the CNPs remains essentially constant to serve as an internal refence signal. The FRET hybrid exhibits excellent sensitivity and selectivity to detect the cysteine and an assay was developed for the screening of biomolecules, like cystine. The method was evaluated as cysteine spike recovery from the fetal bovine serum with satisfactory results.

5.2. Experimental Section

5.2.1. Materials

The1,2-distearoyl-sn-glycero-3-phosphoethanolamine conjugated polyethylene glycol with active succinimidyl ester (DSPE-PEG-NHS, MW 3500) was obtained from Nanocs Inc. (New York, NY, USA). The 1-ethyl-3-(3-dimethylaminopropyl) carbodiimide hydrochloride (EDC) was purchased from Thermo Fisher Scientific (Waltham, MA, USA). The L-glutathione in the reduced form (GSH, >=98.0 %), polyethylenimine (PEI, branched, <= 1 % water), poly(9-vinylcarbazole) (PVK), *N*-hydroxysuccinimide (NSH), fetal calf serum, 4-(2-hydroxyethyl)-1-piperazineethanesulfonic acid (HEPES, >=99.5 %

), cysteine (97 %), alanine (>= 99.5 %), arginine (>= 98 %), glycine (99.0 %), glutamine (>= 99 %), histidine (>= 99 %), methionine (>= 98 %), phenylalanine (>= 98 %), proline (>= 99 %), tryptophan (>= 98 %), tyrosine (>= 98 %), and valine (>= 98 %) were obtained from Sigma-Aldrich (St. Louis, MO, USA). Hydrogen tetrachloroaurate trihydrate ($HAuCl_4$, 99.99 %) was provided by Alfa Aesar (Tewksbury, MA, USA). Stock standard solution of 100 mg/L ionic gold in nitric acid was purchased from Inorganic Ventures (Christiansburg, VA, USA) and used to make working standards between 0.02–5.0 µg/L (serial dilution with 2 % nitric acid) for ICP-MS calibration. Grade 4.8 liquid argon and Grade 5 helium in ICP-MS were used for instrument operation and an inert collision gas under kinetic energy discrimination mode to measure the gold concentration. Deionized water (18.2 MΩ•cm) produced from Millipore Synergy purification system (Burlington, MA, USA) was used for all sample preparation and analysis in this work.

5.2.2. Instruments

A JEOL JEM-2100 high-resolution transmission electron microscope (HRTEM) (JEOL Ltd., Tokyo, Japan) was used at 200 kV to take transmission electron microscope (TEM) images of PVK PNs and AuNCs. A Zetasizer Nano (Malvern Panalytical, UK) was used to measure the Zeta potential and hydrodynamic diameter of PVK PNs and AuNCs suspended in 10 mM, pH 7.0 HEPES solutions. A PerkinElmer Lambda 1050 UV/VIS/NIR spectrometer (Santa Clara, CA, USA) was used to obtain the absorption spectra of PVK PNs, AuNCs, PVK@AuNCs, and the mixture of PVK@AuNCs and various amount of cysteine for investigations of the fluorescence quenching mechanism. A Thermo Scientific iCAP Qc inductively coupled plasma mass spectrometer (Waltham, MA, USA) operated with Qtegra^{TM} software (version 2.8.2944.202) was used to determine

the gold content in pure AuNCs and AuNCs-based hybrid suspensions. The THERMO-4AREV standard was run daily to perform instrument tuning for a maximum ^{59}Co, ^{238}U and minimum $^{140}Ce^{16}O/^{140}Ce$ oxide signal. The target isotope ^{197}Au as well as the internal standards isotopes (^{74}Ge and ^{209}Bi) signals were monitored in the ICP-MS measurements.

A Jobin Yvon Horiba Fluorolog spectrofluorometer (Horiba, NJ, USA) was applied for the time resolved luminescence decay measurements of PVK PNs, AuNCs, and PVK@AuNCs in 10 mM, pH 7.0 HEPES solution. Fluorescence measurements were carried out using a RF-6000 fluorophotometer (SHIMADZU, Kyoto, Japan). When the excitation wavelength was set to 342 nm, the fluorescence intensities at 385 nm and 630 nm were collected to evaluate performance for determination of cysteine. Widths of both the excitation and emission slits were 10.0 nm. The measurements of relative quantum yield for pure AuNCs and hybrid AuNCs were also performed on the RF-6000 fluorophotometer (SHIMADZU, Kyoto, Japan). To limit reabsorption effects, samples where diluted to ensure that light absorbances at the excitation wavelength were below 0.1 AU. All the measurements in this work were carried out at room temperature.

5.2.3. Synthesis of PVK polymer nanoparticles (PVK PNs)

The conjugated poly(9-vinylcarbazole) polymers nanoparticles (PVK PNs) were synthesized by the nanoprecipitation method with only slight changes from the literature.[135] A 10.0 mg portion of PVK polymer was dispersed in 10.0 mL THF to make a 1.0 mg/mL of PVK stock solution. Meanwhile, the block copolymer 1,2-distearoyl-sn-glycero-3-phosphoethanolamine-polyethylene glycol-polyetherimide (DSPE-PEG-PEI) was formed by mixing 200 μL of 5.0 mg/mL 1,2-distearoyl-sn-glycero-3-phosphoethanolamine conjugated polyethylene glycol with active succinimidyl ester (DSPE-PEG-NSH) and 800

μL of 10.0 mg/mL polyethylenimine (PEI) in THF with constant shaking for 12 h at room temperature. Then, 100 μL of 1.0 mg/mL PVK stock solution and 50 μL of 1.0 mg/mL DSPE-PEG-PEI solution were added into 850 μL THF. Afterwards, the mixture was quickly injected into 5.00 mL of deionized water under vigorous sonication in an ice-bath ultrasonicate for 2 min. The THF was removed by heating the solution at 80 ℃ with nitrogen gas for 15 min. The prepared PVK PNs with a final concentration of 15.0 μg/mL was ready for further characterization and application.

5.2.4. Synthesis of gold nanoclusters (AuNCs)

The preparation of AuNCs was produced according to the reported literature.[133] The $HAuCl_4$ (0.50 mL, 20 mM) was added to 3.75 mL of deionized water at 25 °C. Following by addition of L-glutathione (GSH, 0.75 mL, 20 mM) with constantly stirring for 30 min. The mixture was heated at 70 °C under gentle stirring for 24 h. An aqueous solution of orange color AuNCs was produced. The AuNCs with concentration of 1.5 mg/mL could be stored at 4 °C for their further application.

5.2.5. Construction of PVK@AuNCs nanohybrid

Preparation of the nanohybrid using PVK PNs and AuNCs was only slightly changed from the reported literature.[180] AuNCs (2.7 mL, 1.5 mg/mL) were dispersed into HEPES solution (3.5 mL, 20 mM, pH 7.4) under gentle stirring. Then, an aliquot of EDC solution (100 μL, 100 mM) was added into the mixture for 30 min to active the carboxyl groups on the surface of AuNCs. followed by addition of the NSH solution (100 μL, 100 mM) with stirring for another 30 min. Afterwards, an aliquot of PVK PNs (300 μL, 15.0 μg/mL) was added and the mixture was incubated for 12 h at room temperature. Finally, the PVK@AuNCs nanohybrid was collected and washed twice with deionized water by

centrifugation under 10,000 rpm for 20 min. The purified nanohybrid was dispersed in 500 mL of deionized water for further applications.

5.2.6. Determination of cysteine using PVK@AuNCs

The assay of cysteine using PVK@AuNCs was performed under optimized conditions. A 20 μL aliquot of 1.0 mg/mL stock hybrid was mixed with different amounts of cysteine ranging from 0.5 μM to 600 μM in 10.0 mM HEPES solution (pH=11.0). After incubation for 360 min at room temperature, the fluorescence emission spectra of the mixture were recorded and the emission intensities at 385 nm and 630 nm were collected for the quantitative analysis. Selectivity of the cysteine determination was investigated by addition of different interferent molecules including alanine, arginine, glycine, glutamine, histidine, methionine, phenylalanine, proline, tryptophan, tyrosine, and valine. Operational conditions were the same as the previous experiments. Spike-recovery samples were evaluated by addition of 1 μM and 100 μM of cysteine into the diluted fetal calf serum.

5.3. Results and Discussion

5.3.1. Design of the FRET-based ratiometric nanoprobe

A FRET-based nanohybrid was developed to improve the quantum yield of ordinary AuNCs. The nanohybrid was then used for cysteine determination through a fluorescence quenching process. One design feature was a close distance between the donor and accept sites in FRET nanohybrid (< 10 nm). This feature would allow transfer energy from much higher number photons to the acceptor of AuNCs and thereby yield a stronger fluorescence emission at 630 nm than a direct excitation of AuNCs at 385 nm. To achieve this higher quantum yield, a conjugated polymer nanoparticle (CPN) with excellent light-harvesting capacity was selected as the FRET donor and the AuNC acted as acceptor.

Based on the literature,[134, 181] hybrid AuNCs accept energy more efficiently via this FRET process than pure AuNCs do by direct excitation. Besides improving quantum yield of AuNCs, the conjugated polymer nanoparticles have excellent photostability, low toxicity, and fast energy transfer

Because the excitation wavelength of the AuNC acceptor should overlap with the fluorescence emission of the donor to produce a strong FRET, the low-toxic poly(9-vinylcarbazole) polymer (PVK) with a fluorescence emission peak at 385 nm was chosen as the FRET donor as shown in Scheme 5.1A. To produce a spherical nanoparticle from this conjugated polymer, a simple nanoprecipitation method was used that blended hydrophobic PVK with an amphiphilic block-copolymer (DSPE-PEG-PEI) in the water. The nanoprecipation of DSPE-PEG-PEI and PVK formed the polyvinylcarbazole polymer nanoparticles (PVK PNs) as shown in Scheme 5.1A.

FRET efficiency is highest when the distance between donor and acceptor centers is short, so covalent crosslinking between –COOH groups on AuCNs and $-NH_2$ groups on PVK PNs was employed to ensure close contact between the conjugated polymer nanoparticles and AuNCs. The $-NH_2$ groups of the DSPE-PEG-PEI's served perfectly on this regard. Also, EDC and NSH were used to assist in the interaction between –COOH groups and $-NH_2$ groups as shown in Scheme 5.1A. Overall, the final hybrid nanoprobe of this synthesis yielded fluorescence emissions at 385 nm and 630 nm, when excited at 342 nm because energy of the PVK PNs was efficiently transferred to the AuNCs.

To demonstrate the nanohybrid's application in bioanalysis, the biomolecule cystine was selected as the target analyte. Scheme 5.1B shows how the FRET dual-emission nanohybrid was used as a fluorescence ratiometric probe for sensing cysteine. In

the presence of cysteine, the signal intensity at 385 nm from PVK PNs remained constant as a convenient internal reference, but the signal intensity at 630 nm from AuNCs decreased significantly due to adsorption cysteine through formation of Au (I)-thiolate bonds under basic conditions and simultaneous disruption of the gold core gold cluster.[182] To relate these intensity changes to the concentration of cystine, a ratio approach was used. The ratio of the fluorescence intensities of 385 to 630 nm in the absence of cysteine, $(I_{385}/I_{630})_0 = F_0$, was used as a blank reading. The ratio of the fluorescence intensities of 385 to 630 nm in the presence of cysteine, was referred as $(I_{385}/I_{630}) = F$. The ratio of $(F - F_0)/F_0$ was related to the concentration of cysteine.

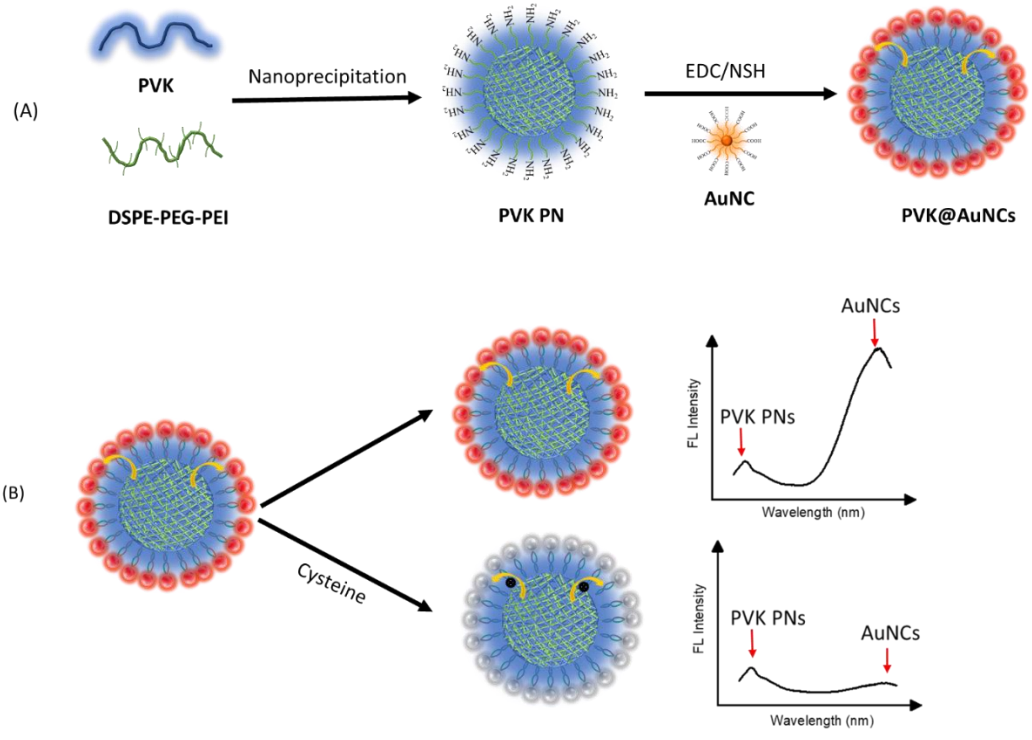

Scheme 5.1. Schematic illustration of (A) the construction of PVK@AuNCs and (B) its application for cysteine detection.

5.3.2. Characterization of AuNCs and PVK PNs

The morphology and size of the AuNCs and PVK PNs were characterized using HRTEM. The small dots of AuNCs with diameters at around 2 nm and excellent mono-dispersity were observed in the HRTEM images (Figure 5.1A). The hydrodynamic diameter of AuNCs was measured to be 4 ± 1 nm by DLS (Insert Figure 5.1A). Meanwhile, the monodispersed PVK PNs were observed to be spherical with a diameter of 35 ± 6 nm in HRTEM images (Figure 5.1B). The hydrodynamic diameter measured by DLS was to be 47 ± 1 nm (Insert Figure 5.1B), which was slight larger than that measured by high-resolution TEM.

Zeta potential of these two materials were also measured in 10 mM HEPES buffer solution under neutral pH condition and found to be -15 ± 3 mV and 26 ± 3 mV (Figure 5.1C), respectively. Such negative charge of AuNCs and positive charge of PVK PNs under neutral pH condition provided the supportive information on the existence of –COOH groups on AuNCs and $–NH_2$ groups on PVK PNs.

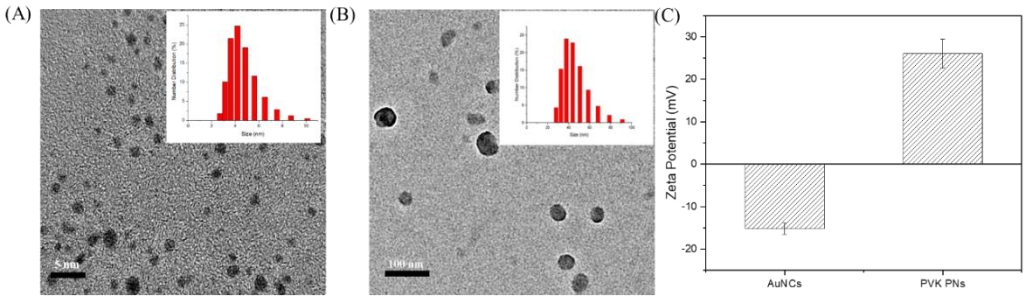

Figure 5.1. (A) HRTEM image of AuNCs. Insert, the size distribution of AuNCs by DLS. (B) HRTEM image of PVK PNs. Insert, the size distribution of PVK PNs by DLS. (C) Zeta potential of AuNCs and PVK PNs in HEPES buffer solution (10 mM, pH=7.0).

5.3.3. Optical properties of AuNCs and PVK PNs

Optical properties of acceptor and donor moieties are very important to assessing FRET interactions, so the optical properties of AuNCs (acceptors) and PVK PNs (donors)

were investigated in 10 mM, pH 7.0 HEPES buffer solution (Figure 5.2). When the AuNCs are excited at 385nm wavelength, a fluorescence emission peak at 630 nm is observed. These properties are complimentary to the PVK PNs which have a fluorescence emission peak at 385 nm with an excitation wavelength at 342 nm. Because the emission wavelengths of the PVK PNs overlap with excitation wavelengths of the AuNCs, a highly efficient FRET occurs between the PVK PNs and AuNCs.

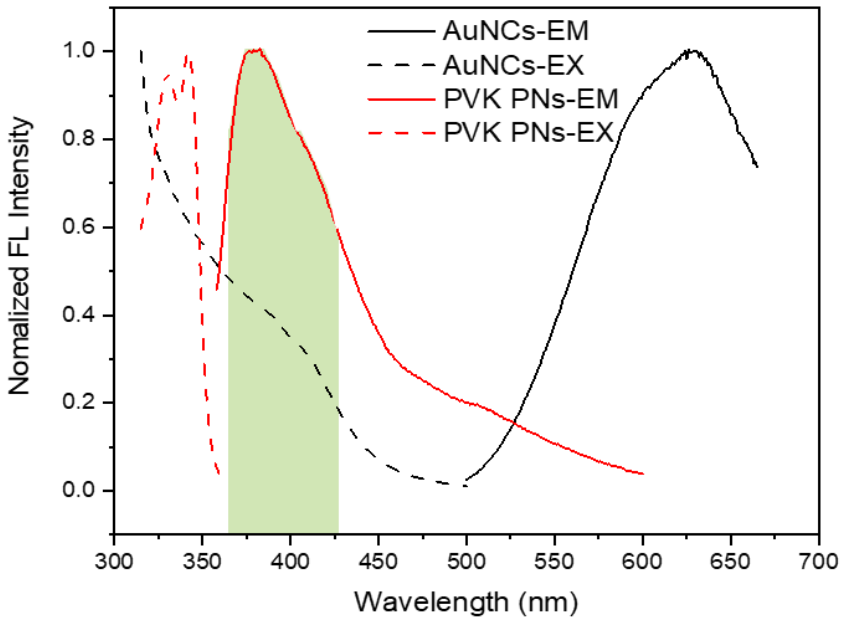

Figure 5.2. Fluorescence emission and excitation spectra of AuNCs (black lines) and PVK PNs (red lines) in 10 mM, pH 7.0 HEPES buffer solution. AuNCs, λ_{ex} = 385 nm, λ_{em} = 630 nm; PVK PNs, λ_{ex} = 342 nm, λ_{em} = 385 nm.

To more fully understand the fluorescence properties of the AuNCs and PVK PNs, they were investigated over a range of pH (Figure 5.3). The fluorescence emissions of AuNCs (630 nm) and PVK PNs (385 nm) both increased slowly when pH increased from 3 to 9 and had no change at pH 11. These results indicated that both materials were more efficient emitters under basic conditions and that deprotonation of carboxylic groups on

AuNCs and amine groups on PVK PNs favored excited-state electron transfer that enhanced luminescence intensity.[183] Overall, this result indicated that the combination of AuNCs and PVK PNs to construct a FRET assembly would present stronger fluorescence signals under basic condition.

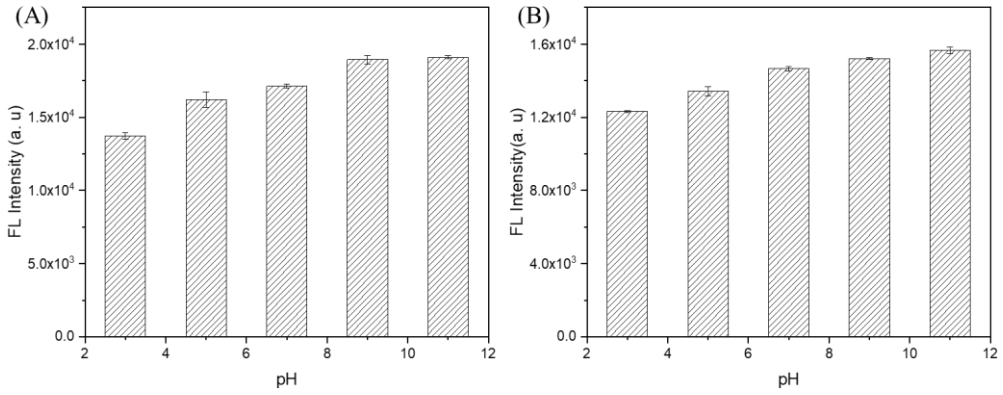

Figure 5.3. Effects of pH on the fluorescence intensity of (A) 0.2 mg/mL AuNCs at 630 nm and (B) 0.5 mg/mL PVK PNs at 385 nm at different pH values. AuNCs, λ_{ex} = 385 nm, λ_{em} = 630 nm; PVK PNs, λ_{ex} = 342 nm, λ_{em} = 385nm.

5.3.4. Optimization of AuNCs-PVK PNs hybrid

The FRET-based hybrid was synthesized by chemically binding AuNCs and PVK PNs using the traditional protein coupling reagents EDC and NSH. The stoichiometric ratio of PVK PNs to AuNCs was optimized (Figure 5.4) to obtain the best FRET-based hybrid. Figure 5.4A shows the fluorescence emission of PVK PNs at 385 nm declined and had no obvious change when the volume ratio of PVK PNs to AuNCs was above 1:8. Therefore, the ratio of fluorescence signal intensity at 385 nm of PVK PNs in the absence (I_{385-0}) and presence (I_{385}) of AuNCs, referred as (I_{385-0}/I_{385}), were also calculated (Figure 5.4B). The ratio of fluorescence intensity of PVK PNs increased and reached a plateau when the volume ratio of PVK PNs and AuNCs was up to 1:8, indicating the maximum energy were

transferred from PVK PNs to the acceptor AuNCs. Therefore, the hybrid was obtained under the optimized volume ratio of 1:9.

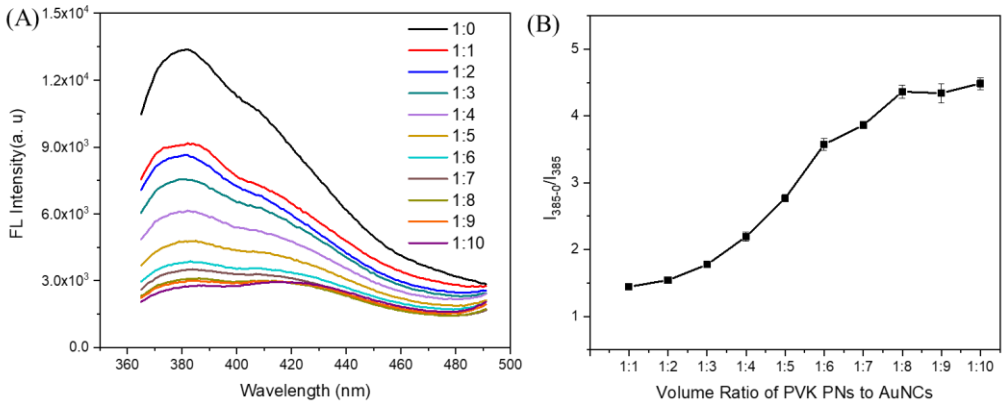

Figure 5.4. (A) Fluorescence spectra of PVK PNs at different ratios of PVK PNs to AuNCs. (B) Ratio of fluorescence intensity at 385 nm of PVK PNs at different ratios of PVK PNs to AuNCs (I_{385}). λ_{ex} = 342 nm, λ_{em} = 385 nm

5.3.5. Characterization of the nanohybrid

5.3.5.1. Size, charge and optical properties of the nanohybrid

The PVK@AuNCs described in this section were prepared under the optimized volume ratio of PVK PNs and AuNCs. The hydrodynamic diameter of the hybrid was measured by DLS and found to be 65 ± 2 nm. These hybrids showed a negative charge of -18 ± 4 mV under neutral pH condition, indicating good mono-dispersity in the solution. To better understand the fluorescent nanohybrid, its optical properties were also investigated. As shown in Figure 5.5A, the pale yellow PVK@AuNCs had two fluorescence emission peaks when it was excited at 342 nm. Because one peak was at 385 nm (from PVK PNs) and the other was at 630 nm (from AuNCs), it was clear that the assembly was successfully synthesized. Moreover, the results showed that fluorescence of the AuNCs in hybrid (at 630 nm) was significantly enhanced. When fluorescence

intensities at 630 nm were compared for hybrid and pure AuNC samples containing the same 50 mM of Au atoms (as shown in Figure 5.5A), the fluorescence intensity of the hybrid AuNCs was more than 2.5-fold higher. This fluorescence enhancement indicated that FRET occurred between the PVK PNs and AuNCs of the nanohybrid. A visual indication of tis FRET enhancement also evident in the photographs of Figure 5.5B which show that the hybrid emission is brighter than the solitary AuNCs under ultra-visible light and visible light.

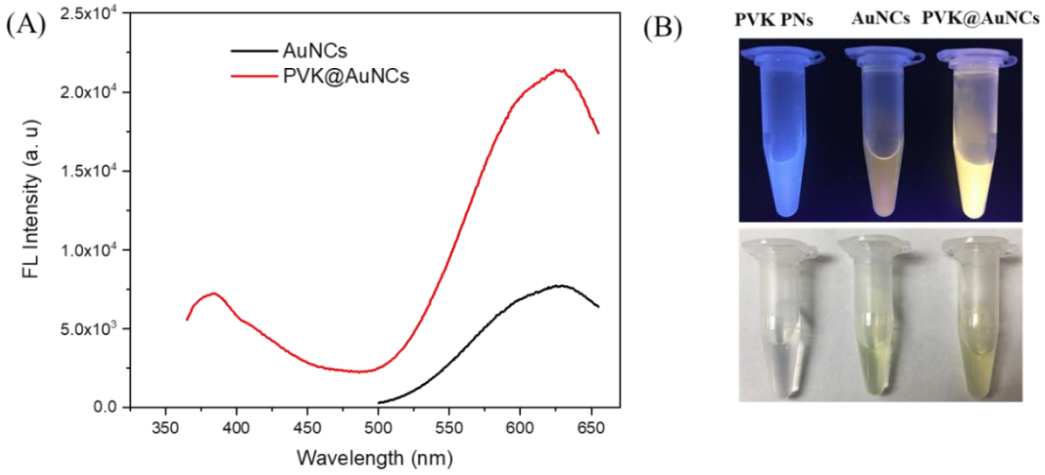

Figure 5.5. Fluorescence spectra of AuNCs and PVK@AuNCs that containing 0.05 mM Au atoms, λ_{ex} = 342 nm. (B) Photographs of PVK PNs, AuNCs, and PVK@AuNCs under 365 nm UV light (top) and visible light (down).

5.3.5.2. FRET efficiency of the nanohybrid

Luminescence lifetime decay measurements of the PVK PNs, AuNCs, and PVK@AuNCs were carried out (Figure 5.6) to evaluate FRET efficiency of the nanohybrid. Two parameters, lifetime of fluorophores and transfer efficiency, were both used for the evaluation.

Fluorophore lifetimes of PVK PNs and AuNCs samples alone were found to be 113 ps and 30 ps, respectively, when the decay curves were fitted with an exponential decay function. By comparison, decay lifetimes of PVK PNs and AuNCs in the hybrid (46 ps, and 145 ps, respectively) were significantly different from the pure components. Specifically, lifetime of PVK PNs in the hybrid was shorted, while the lifetime of AuNCs in hybrid was prolonged. This behavior strongly indicates energy transfer from PVK PNs to AuNCs in the hybrid.

Transfer efficiency (φ) was calculated by using the lifetime of the FRET donor PVK PNs in the absence (τ_D, ps) and presence of FRET acceptor AuNCs (τ_{DA}, ps), as shown in Eq. 5-1.[132, 184]

$$\varphi = 1 - \frac{\tau_{DA}}{\tau_D} \times 100\ \% \tag{5-1}$$

The FRET efficiency of PVK PNs in the hybrid was around 59 %. After accepting the energy from PVK PNs, the lifetime of AuNCs in hybrid was lengthened, which was confirmed by the above lifetime decay measurement results.

Moreover, the relative quantum yield of pure AuNCs and AuNCs in hybrid were measured by using the standard Rhodamine 101 in ethanol with 0.01 % HCl. Their quantum yield (Φ_x) was determined by using the quantum yield of standard (Φ_{st}=1 at 597 nm), refractive index of ethanol with 0.01 % HCl (η_{st}, 1.36) and HEPES solution (η_x, 1.33), the linear slope of the integrated fluorescence intensity *versus* absorbance of standard Rhodamine 101(m_{st}) and pure AuNCs or AuNCs in hybrid (m_x) in Eq. 5-2.[149]

$$\Phi_x = \Phi_{st}\left(\frac{m_x}{m_{st}}\right)\left(\frac{{\eta_x}^2}{{\eta_{st}}^2}\right) \tag{5-2}$$

The quantum yield of pure AuNCs and AuNCs in hybrid was determined to be 1 % and 3 %, indicating successful and significant enhancement of quantum yield of AuNCs by covalently coupling them to the PVK PNs.

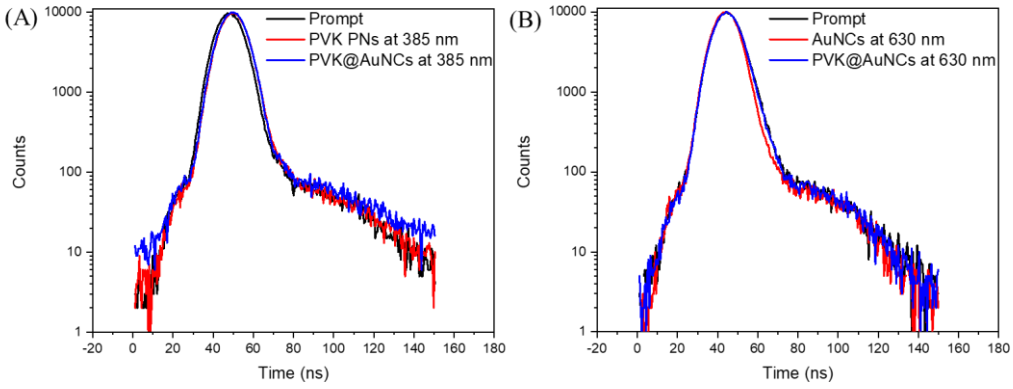

Figure 5.6. (A) Fluorescence lifetime decay curves at 385 nm of PVK PNs and PVK@AuNCs. (B) Fluorescence lifetime decay curves at 630 nm of AuNCs and PVK@AuNCs.

5.3.6. Cysteine determination using PVK@AuNCs

To examine the feasibility of cysteine determination using the PVK@AuNCs, fluorescence spectra of AuNCs, PVK PNs, and PVK@AuNCs in the absence and present of 200 uM cysteine were measured in basic (pH 11.0) 10 mM HEPES solutions (Figure 5.7A). In the presence of 200 uM cysteine, fluorescence intensity at 630 nm of both pure AuNCs and PVK@AuNCs decreased by 97 % and 73 %, respectively, but fluorescence intensity at 385 nm of both pure PVK PNs and PVK@AuNCs had no obvious change. These results demonstrated that the FRET ratiometric nanohybrid was a promising fluorescence sensing nanoprobe for the detection of cysteine.

To better understand the fluorescence quenching process occurring between cystine and the PVK@AuNCs, UV-vis spectra of PVK@AuNCs in the presence of increasing amounts of cysteine (0, 5, 10, 100, and 200 μM) were evaluated (Figure 5.7B). In the

absence of cysteine, the spectrum of PVK@AuNCs showed two absorption peaks at 345 and 400 nm which corresponded to the PVK PNs and AuNCs in the hybrid, respectively. The peak at 345 nm remained consistent with additions of 0, 5, 10, 100, and 200 μM cysteine but the peak at around 400 nm gradually declined, indicating the decrease of electron energy at around 400 nm. It has been reported that the -SH groups in the cysteine interacte with the gold atoms and etch the gold core to Au(I) which quenches the fluorescence signal of AuNCs.[182]

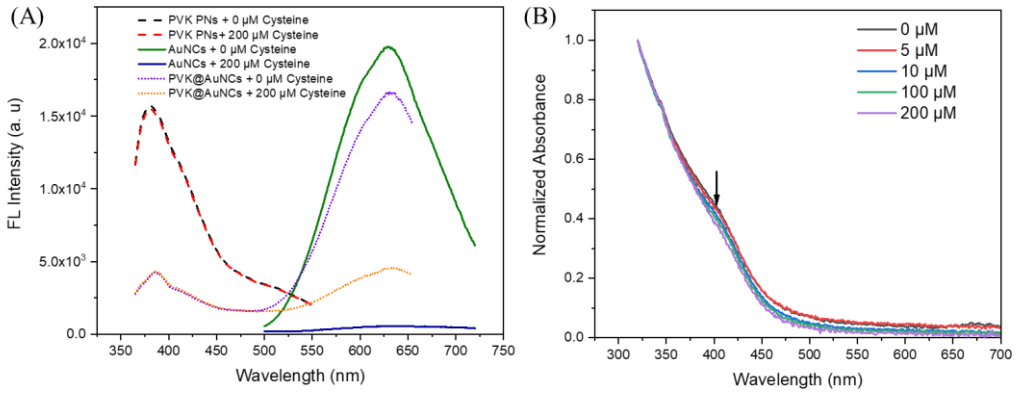

Figure 5.7. (A) Fluorescence spectra of AuNCs, PVK PNs, and PVK@AuNCs with or without the addition of 200 uM Cysteine in 10 mM, pH 11.0 HEPES solution. (B) The UV-vis spectra of 20 μg/ mL PVK@AuNCs in the presence of different amounts of cysteine including 0.0, 5, 10, 100, and 200 μM.

5.3.7. Determination of cysteine

To obtain the lowest limit of detection for cysteine using the FRET-based ratiometric nanohybrid, the reaction conditions for sensing 200 μM cysteine including the pH, concentration of probe, and incubation time were optimized. Figure 5.8 shows the overall ratio of fluorescence intensity $((F - F_0)/F_0)$ of PVK@AuNCs in the presence of cysteine under different conditions.

Below pH 7 the fluorescence intensity ratio of the hybrid changed very little but it increased significantly under basic conditions. Although pH 11 falls well outside the physiological range of most biological systems, this was the optimal pH for detection of cysteine.

Optimizations of the sensing probe concentration and incubation time are shown in Figure 5.8B and 5.8C. As the hybrid concentration was increased from 0 to 20 μg/mL, the fluorescence intensity ratio of the hybrid reached a maximum and then decreased. Accordingly, an optimum concentration of 20 μg/mL of hybrid was chosen for subsequence incubation experiments. Incubation time has a profound effect on quenching the fluorescence signal of hybrid by cysteine (Figure 5.8C), presumably because of a slow gold-thiol reaction. Incubation of the solution mixture for longer periods yielded greater quenching up to a limit 300 min, after which signal quenching reached a plateau. Accordingly, an incubation time of 360 min (6 hours) was chosen as optimum to ensure that the quenching reaction was complete for all samples.

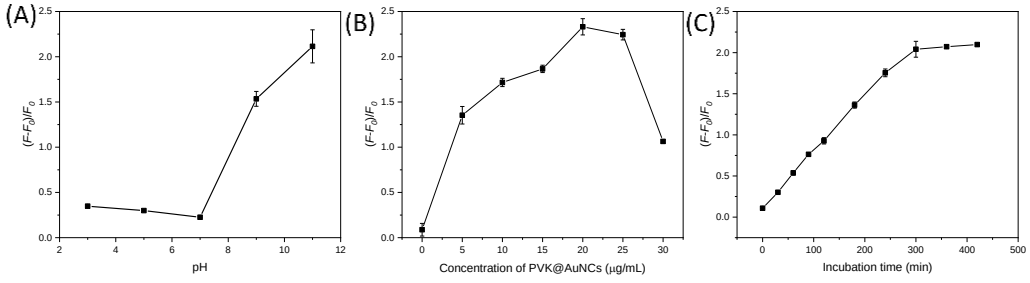

Figure 5.8. Fluorescence intensity ratio of the PVK@AuNCs in the absence and presence of 200 μM cysteine under different conditions. (A), pH. (B), amount of PVK@AuNCs. (C), incubation time. λ_{ex} = 342 nm, λ_{em1} = 385nm, λ_{em2} = 630 nm.

The sensitivity of the nanoprobe for cystine was evaluated under the optimum reaction conditions established above. Different concentrations of cysteine were incubated

with the FRET-based nanohybrid for the proscribed incubation time, followed by fluorescence spectra measurement (Figure 5.9A). The fluorescence intensity at 385 nm remained almost constant while the emission at 630 nm decreased with cystine concentration until it showed no further change above 550 μM. A calibration plot of the overall fluorescence intensity ratio ((F-F_0)/F) versus concentration of cysteine is shown in Figure 5.9B. Two linear regions are clear from this plot; one at the lowest cystine concentrations between 0.5 μM to 10 μM (inear correlation 0.995) and at higher cystine concentration between 20 μM to 550 μM (linear correlation 0.996). The lower range demonstrated the highest sensitivity (i.e., greatest slope) and the limit of detection (LOD) determined from this linear region was 0.18 μM. This LOD was lower than other methods using conventional AuNC as nanoprobes for cysteine.[180, 185, 186]

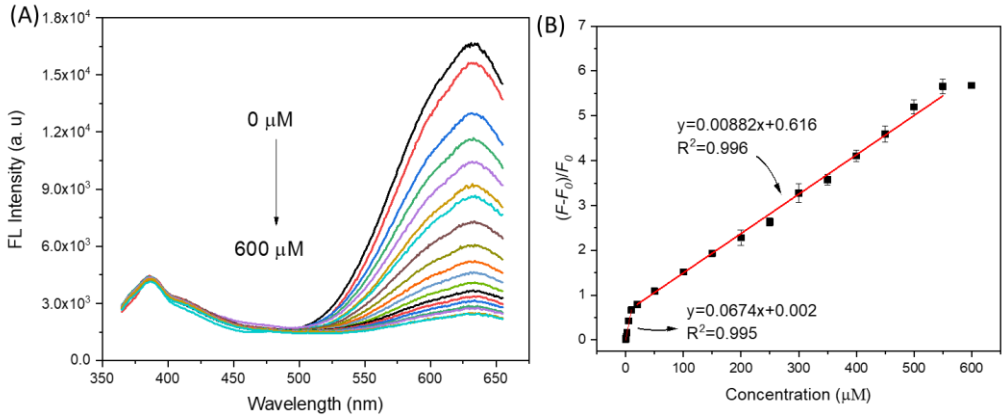

Figure 5.9. (A) Fluorescence spectra of PVK@AuNCs in the presence of various amount of cysteine in 10 mM, pH 11.0 HEPES solution. (B) The plot of the ratio of fluorescence intensity of PVK@AuNCs at varied cysteine concentrations. λ_{ex} = 342 nm, λ_{em1} = 385nm, λ_{em2} = 630 nm.

5.3.8. Selectivity of cysteine determination

Selectivity of the cysteine assay was also evaluated (Figure 5.10) by separately combining the AuNCs-based nanohybrid with cysteine or other types of amino acid

interferences present at a concentration of 100 μM. Fluorescence intensity ratio of the hybrid increased in the presence of cysteine because the -SH groups were available to etch gold atoms in AuNCs in the nanoprobe. occurrence of etching gold atoms in AuNC by cysteine containing -SH groups.[187] However, the fluorescence intensity ratio of hybrid remained almost unchanged when combined with many other potential interferences, indicating that the assembled FRET nanoprobe could detect the cysteine with high selectivity.

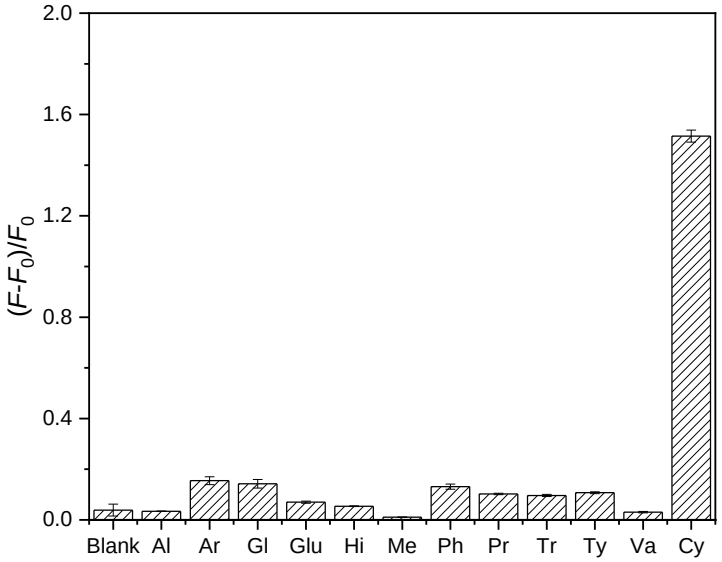

Figure 5.10. Specific responses of PVK@AuNCs to cysteine over a common interference of 100 μM. λ_{ex} = 342. From left to right is for Blank, Alanine, Arginine, Glycine, Glutamine, Histidine, Methionine, Phenylalanine, Proline, Tryptophan, Tyrosine, Valine, and Cysteine, being abbreviated as Blank, Al, Ar, Gl, Glu, Hi, Me, Ph, Po, Tr, Ty, Va, and Cy, respectively.

5.3.9. Detection of cysteine in fetal calf serum

To examine the applicability of the assembled FRET probe to determine cysteine in a biological sample, a fixed concentration of nanohybrid was used to detect different

concentrations of cysteine (1 μM and 100 μM) in fetal calf serum diluted with HEPES buffer solution. The spiked recovery results from this assay are summarized in Table 5.1. The recoveries obtained with these samples were 98 % for 1 μM cystine and 109 % for 100 μM cystine. These results demonstrate that the constructed nanohybrid has the potential for quantitative determination of cysteine in biological media.

Table 5.1. Parameters for the application of PVK@AuNCs to the cysteine determination in the fetal bovine serum (10 mM HEPES buffer solution, pH = 11).

Sample	n	Spiked (μM)	Found (μM)	Recovery (%)
1	3	1.0	0.98 ± 0.02	98 ± 2
2	3	100.0	108.8 ± 6.67	109 ± 7

5.4. Conclusion

In sum, we have developed a well-behaved FRET ratiometric nanohybrid using AuNCs and PVK PNs through chemical binding. The PVK PNs of this nanohybrid participate as a FRET donor and successfully transfer their energy with a 59 % efficiency to the acceptor AuNCs and demonstrate a quantum yield increase from 1 % to 3 %. The nanohybrid shows a strong response to the biomolecule cysteine in basic HEPES solutions due to etching the gold core of the AuNCs in the hybrid. The optimized assay shows excellent calibration sensitivity for cysteine with a LOD of 0.18 μM over a linear range from 0.5 μM to 10 μM and satisfactory spike recoveries of cystine from biological media.

CHAPTER VI

CONCLUSIONS

The overall objective of this dissertation was to further the development of MCPs by improving their fundamental characterization and by creating new applications for biosensing and bioimaging. Chapter 2 of this work focused on the optimization of single particle inductively coupled plasma mass spectrometry (spICP-MS) for accurate analysis of metallic particles larger than 100 nm. This method offers significant advantages in comparison with the transmission electron microscopy (TEM) and conventional inductively coupled plasma mass spectrometry (ICP-MS) because it is capable of providing accurate metal concentration per particle for thousands of particles in a short period of time

Chapter 3 demonstrated just how useful spICP-MS can be for routine characterization of metal distribution in MCP samples. Silica nanoparticles doped with tris(2,2'-bipyridyl)ruthenium(II) (Ru-SiO_2 NPs) using a water-in-oil microemulsion method were used as a MCP model to investigate per-particle concentrations of metal dopant as measured by spICP-MS. The results showed the *average* concentration of metal-dopant measured per-particle by spICP-MS is consistent with the bulk-sample methods over a range of dopant levels. However, the concentration of dopant measured per particle is not homogeneous and does not adhere to a simple Gaussian-like distribution encountered with simple one-component NPs, such as gold, silver, or TiO_2. Instead, the amount of dopant has an unprecedented geometric distribution regardless of doping level. This demonstrates that a complex distribution mechanism is taking place during the microemulsion synthesis of these nanocoposites. More importantly, it illustrates that per-particle analysis should be routine part of nanocomposites characterization to ensure that

the common assumption of homogeneous dopant distribution is valid.

Chapters 4 and 5 describe the development of small size MCPs for application of biosensing and bioimaging. The methods highlighted in both chapters rely on gold nanoclusters (AuNCs) assembled with conjugated polymer nanoparticles (CPNs) to construct very different ratiometric fluorescence nanoprobes.

Chapter 4 describes the development of a sandwich structured nanoprobe that was constructed by using conjugated polydioctylfluorene polymer dots (PFO CPNs) doped silica nanoparticles and AuNCs. In the presence of Cu^{2+}, the fluorescence emission from AuNCs of the nanoprobe at 630 nm is quenched in contrast to the constant florescence emission from the reference PFO CPNs. The nanoprobe showed excellent sensitivity and selectivity for quantitative analysis of Cu^{2+} with a detection limit of 10.5 nM and excellent potential for imaging application with biological systems.

Finally, Chapter 5 expands the ratiometric sensing applications of AuNCs by combining them with conjugated polyvinylcarbazole polymer nanoparticles (PVK PNs) to develop a very different nanohybrid. In this case the nanohybrid demonstrates a strong fluorescence resonance energy transfer (FRET) that can be used to determine cysteine concentration in biological media over a dynamic range of 0.5 μM to 600 μM.

REFERENCES

1. Gogotsi, Y., *Nanomaterials handbook*. CRC press,Inc.:Boca Raton, FL; **2017.**

2. Li, Y. F.; Chen, C., Fate and Toxicity of Metallic and Metal-Containing Nanoparticles for Biomedical Applications. *Small* **2011,** *7* (21), 2965-2980.

3. Xiong, T.; Dumat, C.; Dappe, V.; Vezin, H.; Schreck, E.; Shahid, M.; Pierart, A.; Sobanska, S., Copper Oxide Nanoparticle Foliar Uptake, Phytotoxicity, and Consequences for Sustainable Urban Agriculture. *Environ. Sci. Technol.* **2017,** *51* (9), 5242-5251.

4. Chen, H., Metal Based Nanoparticles in Agricultural System: Behavior, Transport, and Interaction with Plants. *Chem. Speciat. Bioavailab.* **2018,** *30* (1), 123-134.

5. Miazek, K.; Iwanek, W.; Remacle, C.; Richel, A.; Goffin, D., Effect of Metals, Metalloids and Metallic Nanoparticles on Microalgae Growth and Industrial Product Biosynthesis: a review. *Int. J. Mol. Sci.* **2015,** *16* (10), 23929-23969.

6. Leopold, K.; Philippe, A.; Wörle, K.; Schaumann, G. E., Analytical Strategies to the Determination of Metal-Containing Nanoparticles in Environmental Waters. *TrAC Trends Anal. Chem.* **2016,** *84*, 107-120.

7. Tou, F.; Yang, Y.; Feng, J.; Niu, Z.; Pan, H.; Qin, Y.; Guo, X.; Meng, X.; Liu, M.; Hochella, M. F., Environmental Risk Implications of Metals in Sludges from Waste Water Treatment Plants: the Discovery of Vast Stores of Metal-Containing Nanoparticles. *Environ. Sci. Technol.* **2017,** *51* (9), 4831-4840.

8. Li, M.; Liu, W.; Slaveykova, V. I., Effects of Mixtures of Engineered Nanoparticles and Metallic Pollutants on Aquatic Organisms. *Environments* **2020,** *7* (4), 27.

9. Sun, Y.; Zheng, L.; Yang, Y.; Qian, X.; Fu, T.; Li, X.; Yang, Z.; Yan, H.; Cui, C.; Tan, W., Metal–Organic Framework Nanocarriers for Drug Delivery in Biomedical Applications. *Nano-Micro Lett.* **2020,** *12* (1), 1-29.

10. Trigueros, S.; B Domènech, E.; Toulis, V.; Marfany, G., In Vitro Gene Delivery in Retinal Pigment Epithelium Cells by Plasmid DNA-Wrapped Gold Nanoparticles. *Genes* **2019,** *10* (4), 289.

11. Kanagamani, K.; Muthukrishnan, P.; Saravanakumar, K.; Shankar, K.; Kathiresan, A., Photocatalytic Degradation of Environmental Perilous Gentian Violet Dye Using

Leucaena-Mediated Zinc Oxide Nanoparticle and Its Anticancer Activity. *Rare Met.* **2019,** *38* (4), 277-286.

12. Yan, N.; Tang, B. Z.; Wang, W. X., In Vivo Bioimaging of Silver Nanoparticle Ddissolution in the Gut Environment of Zooplankton. *ACS nano* **2018,** *12* (12), 12212-12223.

13. Kokkinos, C.; Economou, A., Emerging Trends in Biosensing Using Stripping Voltammetric Detection of Metal-Containing Nanolabels–A Review. *Anal. Chim. Acta* **2017,** *961*, 12-32.

14. Tan, H. L.; Teow, S. Y.; Pushpamalar, J., Application of Metal Nanoparticle–Hydrogel Composites in Tissue Regeneration. *Bioengineering* **2019,** *6* (1), 17.

15. Jin, R.; Zeng, C.; Zhou, M.; Chen, Y., Atomically Precise Colloidal Metal Nanoclusters and Nanoparticles: Fundamentals and Opportunities. *Chem. Rev.* **2016,** *116* (18), 10346-10413.

16. Wu, Z.; Yao, Q.; Chai, O. J. H.; Ding, N.; Xu, W.; Zang, S.; Xie, J., Unraveling the Impact of Gold(I)–Thiolate Motifs on the Aggregation-Induced Emission of Gold Nanoclusters. *Angew. Chem. Int. Ed.* **2020,** *59* (25), 9934-9939.

17. Wu, Z.; Yao, Q.; Zang, S.; Xie, J., Directed Self-Assembly of Ultrasmall Metal Nanoclusters. *ACS Materials Lett.* **2019,** *1* (2), 237-248.

18. Li, Z.; Abroshan, H.; Liu, C.; Li, G., A Critical Review on the Catalytic Applications of Non-metallic Gold Nanoclusters: Selective Oxidation, Hydrogenation, and Coupling Reactions. *Curr. Org. Chem.* **2017,** *21* (6), 476-488.

19. Zhang, X.; Wu, F. G.; Liu, P.; Wang, H. Y.; Gu, N.; Chen, Z., Synthesis of Ultrastable and Multifunctional Gold Nanoclusters with Enhanced Fluorescence and Potential Anticancer Drug Delivery Application. *J. Colloid Interface Sci.* **2015,** *455*, 6-15.

20. Song, X.; Zhu, W.; Ge, X.; Li, R.; Li, S.; Chen, X.; Song, J.; Xie, J.; Chen, X.; Yang, H., A New Class of NIR-II Gold Nanocluster-Based Protein Biolabels for In Vivo Tumor-Targeted Imaging. *Angew. Chem. Int. Ed.* **2021,** *60* (3), 1306-1312.

21. Dal Forno, S.; Ranno, L.; Lischner, J., Material, Size, and Environment Dependence of Plasmon-Induced Hot Carriers in Metallic Nanoparticles. *J. Phys. Chem. C* **2018,** *122* (15), 8517-8527.

22. Ovais, M.; Khalil, A. T.; Islam, N. U.; Ahmad, I.; Ayaz, M.; Saravanan, M.; Shinwari, Z. K.; Mukherjee, S., Role of Plant Phytochemicals and Microbial Enzymes in Biosynthesis of Metallic Nanoparticles. *Appl. Microbiol. Biotechnol.* **2018,** *102* (16), 6799-6814.

23. Soldevila-Barreda, J. J.; Metzler-Nolte, N., Intracellular Catalysis with Selected Metal Complexes and Metallic Nanoparticles: Advances Toward the Development of Catalytic Metallodrugs. *Chem. Rev.* **2019,** *119* (2), 829-869.

24. Ding, Q.; Li, R.; Chen, M.; Sun, M., Ag nanoparticles-TiO_2 Film Hybrid for Plasmon-Exciton Co-Driven Surface Catalytic Reactions. *Appl. Mater. Today* **2017,** *9*, 251-258.

25. GK, P.; Prashanth, P.; Singh, P.; Nagabhushana, B.; Shivakumara, C.; GM, K.; Nagendra, H.; Sathyananda, H.; Chaturvedi, V., Effect of Doping (with Cobalt or Nickel) and UV Exposure on the Antibacterial, Anticancer, and ROS Generation Activities of Zinc Oxide Nanoparticles. *J. Asian Ceram. Soc.* **2020,** *8* (4), 1175-1187.

26. Carofiglio, M.; Barui, S.; Cauda, V.; Laurenti, M., Doped Zinc Oxide Nanoparticles: Synthesis, Characterization and Potential Use in Nanomedicine. *Appl. Sci.* **2020,** *10* (15), 5194.

27. Cai, L.; Chen, Z.-Z.; Chen, M.-Y.; Tang, H. W.; Pang, D. W., MUC-1 Aptamer-Conjugated Dye-Doped Silica Nanoparticles for MCF-7 Cells Detection. *Biomaterials* **2013,** *34* (2), 371-381.

28. Liu, Y.; Lou, C.; Yang, H.; Shi, M.; Miyoshi, H., Silica Nanoparticles as Promising Drug/Gene Delivery Carriers and Fluorescent Nano-Probes: Recent Advances. *Curr. Cancer Drug Targets* **2011,** *11* (2), 156-163.

29. Montalti, M.; Prodi, L.; Rampazzo, E.; Zaccheroni, N., Dye-doped Silica Nanoparticles as Luminescent Organized Systems for Nanomedicine. *Chem. Soc. Rev.* **2014,** *43* (12), 4243-4268.

30. Mafuné, F.; Kohno, J. Y.; Takeda, Y.; Kondow, T.; Sawabe, H., Formation of Gold Nanoparticles by Laser Ablation in Aqueous Solution of Surfactant. *J. Phys. Chem. B* **2001,** *105* (22), 5114-5120.

31. Amendola, V.; Polizzi, S.; Meneghetti, M., Laser Ablation Synthesis of Gold Nanoparticles in Organic Solvents. *J. Phys. Chem. B* **2006,** *110* (14), 7232-7237.

32. Menéndez-Manjón, A.; Chichkov, B. N.; Barcikowski, S., Influence of Water Temperature on the Hydrodynamic Diameter of Gold Nanoparticles from Laser Ablation. *J. Phys. Chem. C* **2010,** *114* (6), 2499-2504.

33. Fuentes-García, J. A.; Santoyo-Salzar, J.; Rangel-Cortes, E.; Goya, G. F.; Cardozo-Mata, V.; Pescador-Rojas, J. A., Effect of Ultrasonic Irradiation Power on Sonochemical Synthesis of Gold Nanoparticles. *Ultrasonics Sonochem.* **2021,** *70*, 105274.

34. Yasuda, K.; Sato, T.; Asakura, Y., Size-Controlled Synthesis of Gold Nanoparticles by Ultrafine Bubbles and Pulsed Ultrasound. *Chem. Eng. Sci.* **2020,** *217*, 115527.

35. Cho, W. S.; Cho, M.; Jeong, J.; Choi, M.; Cho, H. Y.; Han, B. S.; Kim, S. H.; Kim, H. O.; Lim, Y. T.; Chung, B. H.; Jeong, J., Acute Toxicity and Pharmacokinetics of 13 nm-Sized PEG-Coated Gold Nanoparticles. *Toxicol Appl. Pharmacol.* **2009,** *236* (1), 16-24.

36. Jana, N. R.; Gearheart, L.; Murphy, C. J., Seed-Mediated Growth Approach for Shape-Controlled Synthesis of Spheroidal and Rod-like Gold Nanoparticles Using a Surfactant Template. *Adv. Mater.* **2001,** *13* (18), 1389-1393.

37. Barrientos, L.; Yutronic, N.; del Monte, F.; Gutiérrez, M. C.; Jara, P., Ordered Arrangement of Gold Nanoparticles on An α-Cyclodextrin–Dodecanethiol Inclusion Compound Produced by Magnetron Sputtering. *New J. Chem.* **2007,** *31* (8), 1400-1402.

38. Ashkarran, A. A.; Iraji zad, A.; Mahdavi, S. M.; Ahadian, M. M.; Hormozi Nezhad, M. R., Rapid and Efficient Synthesis of Colloidal Gold Nanoparticles by Arc Discharge method. *Appl. Phys. A* **2009,** *96* (2), 423-428.

39. Lapresta-Fernández, A.; Salinas-Castillo, A.; Anderson De La Llana, S.; Costa-Fernández, J. M.; Domínguez-Meister, S.; Cecchini, R.; Capitán-Vallvey, L.; Moreno-Bondi, M.; Marco, M.-P.; Sánchez-López, J. C., A General Perspective of the Characterization and Quantification of Nanoparticles: Imaging, Spectroscopic, and Separation Techniques. *Crit. Rev. Solid State* **2014,** *39* (6), 423-458.

40. Brar, S. K.; Verma, M., Measurement of Nanoparticles by Light-Scattering Techniques. *TrAC Trends Anal. Chem.* **2011,** *30* (1), 4-17.

41. Krystek, P.; Ulrich, A.; Garcia, C. C.; Manohar, S.; Ritsema, R., Application of plasma spectrometry for the analysis of engineered nanoparticles in suspensions and products. *J. Anal. At. Spectrom.* **2011,** *26* (9), 1701-1721.

42. Lue, J. T., A Review of Characterization and Physical Property Studies of Metallic Nanoparticles. *J. Phys. Chem. Solids* **2001,** *62* (9), 1599-1612.

43. Sanderson, P.; Delgado-Saborit, J. M.; Harrison, R. M., A Review of Chemical and Physical Characterisation of Atmospheric Metallic Nanoparticles. *Atmos. Environ.* **2014,** *94*, 353-365.

44. Han, Y.; Xu, H.; Su, Y.; Xu, Z. L.; Wang, K.; Wang, W., Noble metal (Pt, Au@Pd) Nanoparticles Supported on Metal Organic Framework (MOF-74) Nanoshuttles as High-Selectivity CO_2 Conversion Catalysts. *J. Catal.* **2019,** *370*, 70-78.

45. Hernández Mejía, C.; van Deelen, T. W.; de Jong, K. P., Activity Enhancement of Cobalt Catalysts by Tuning Metal-Support Interactions. *Nat. Commun.* **2018,** *9* (1), 4459.

46. Kobayashi, H.; Mitsuka, Y.; Kitagawa, H. Metal Nanoparticles Covered with a Metal–Organic Framework: From One-Pot Synthetic Methods to Synergistic Energy Storage and Conversion Functions. *Inorg. Chem.* **2016,** *55* (15), 7301-7310.

47. de Souza, M. B. C.; Fernández, P. S.; Solla-Gullón, J., Adatom Decorated Shape-Controlled Metal Nanoparticles: Advanced Electrocatalysts for Energy Conversion. *Curr. Opin. Electrochem.* **2018,** *9*, 121-128.

48. Rai, M.; Ingle, A. P.; Gupta, I.; Brandelli, A., Bioactivity of Noble Metal Nanoparticles Decorated with Biopolymers and Their Application in Drug Delivery. *Int. J. Pharm.* **2015,** *496* (2), 159-172.

49. Mirzaei, H.; Darroudi, M., Zinc Oxide Nanoparticles: Biological Synthesis and Biomedical Applications. *Ceram. Int.* **2017,** *43* (1, Part B), 907-914.

50. Niska, K.; Zielinska, E.; Radomski, M. W.; Inkielewicz-Stepniak, I., Metal Nanoparticles in Dermatology and Cosmetology: Interactions with Human Skin Cells. *Chem. Biol. Interact.* **2018,** *295*, 38-51.

51. Zhang, X. F.; Shen, W.; Gurunathan, S., Silver Nanoparticle-Mediated Cellular Responses in Various Cell Lines: An in Vitro Model. *Int. J. Mol. Sci.* **2016,** *17* (10), 1603.

52. Shi, M.; Kwon, H. S.; Peng, Z.; Elder, A.; Yang, H., Effects of Surface Chemistry on the Generation of Reactive Oxygen Species by Copper Nanoparticles. *ACS Nano* **2012,** *6* (3), 2157-2164.

53. Saha, K.; Agasti, S. S.; Kim, C.; Li, X.; Rotello, V. M., Gold Nanoparticles in Chemical and Biological Sensing. *Chem. Rev.* **2012,** *112* (5), 2739-2779.

54. Warheit, D. B.; Sayes, C. M.; Reed, K. L.; Swain, K. A., Health Effects Related to Nanoparticle Exposures: Environmental, Health and Safety Considerations for Assessing Hazards and Risks. *Pharmacol. Ther.* **2008,** *120* (1), 35-42.

55. Bessa, M. J.; Brandão, F.; Viana, M.; Gomes, J. F.; Monfort, E.; Cassee, F. R.; Fraga, S.; Teixeira, J. P., Nanoparticle Exposure and Hazard in the Ceramic Industry: an Overview of Potential Sources, Toxicity and Health Effects. *Environ. Res.* **2020,** *184*, 109297.

56. Jalink, K.; Cheng, S. S. Y.; Ben Ireland, S.; Louise Meunier, M. A. F., Silver Nanoparticle Uptake in the Human Lung Assessed Through In-Vitro and In-Silico Methods. *Environ. Pollut.* **2020,** *259*, 113880.

57. van den Berg, R.; Elkjaer, C. F.; Gommes, C. J.; Chorkendorff, I.; Sehested, J.; de Jongh, P. E.; de Jong, K. P.; Helveg, S., Revealing the Formation of Copper Nanoparticles from a Homogeneous Solid Precursor by Electron Microscopy. *J. Am. Chem.l Soc.* **2016,** *138* (10), 3433-3442.

58. Luo, K.; Jung, S.; Park, K. H.; Kim, Y. R., Microbial Biosynthesis of Silver Nanoparticles in Different Culture Media. *J. Agric. Food Chem.* **2018,** *66* (4), 957-962.

59. Silmore, K. S.; Gong, X.; Strano, M. S.; Swan, J. W., High-Resolution Nanoparticle Sizing with Maximum A Posteriori Nanoparticle Tracking Analysis. *ACS Nano* **2019,** *13* (4), 3940-3952.

60. Amendola, V.; Meneghetti, M., Size Evaluation of Gold Nanoparticles by UV−vis Spectroscopy. *J. Phys. Chem. C* **2009,** *113* (11), 4277-4285.

61. Laborda, F.; Bolea, E.; Cepriá, G.; Gómez, M. T.; Jiménez, M. S.; Pérez-Arantegui, J.; Castillo, J. R., Detection, Characterization and Quantification of Inorganic Engineered Nanomaterials: A Review of Techniques and Methodological Approaches for the Analysis of Complex Samples. *Anal. Chim. Acta* **2016,** *904*, 10-32.

62. Pace, H. E.; Rogers, N. J.; Jarolimek, C.; Coleman, V. A.; Gray, E. P.; Higgins, C. P.; Ranville, J. F., Single Particle Inductively Coupled Plasma-Mass Spectrometry: A Performance Evaluation and Method Comparison in the Determination of Nanoparticle Size. *Environ. Sci. Technol.* **2012,** *46* (22), 12272-12280.

63. Montaño, M. D.; Majestic, B. J.; Jämting, Å. K.; Westerhoff, P.; Ranville, J. F., Methods for the Detection and Characterization of Silica Colloids by Microsecond spICP-MS. *Anal. Chem.* **2016,** *88* (9), 4733-4741.

64. Pace, H. E.; Rogers, N. J.; Jarolimek, C.; Coleman, V. A.; Higgins, C. P.; Ranville, J. F., Determining Transport Efficiency for the Purpose of Counting and Sizing Nanoparticles via Single Particle Inductively Coupled Plasma Mass Spectrometry. *Anal. Chem.* **2011,** *83* (24), 9361-9369.

65. Reed, R. B.; Higgins, C. P.; Westerhoff, P.; Tadjiki, S.; Ranville, J. F., Overcoming Challenges in Analysis of Polydisperse Metal-Containing Nanoparticles by Single Particle Inductively Coupled Plasma Mass Spectrometry. *J. Anal. At. Spectrom.* **2012,** *27* (7), 1093-1100.

66. Lee, S.; Bi, X.; Reed, R. B.; Ranville, J. F.; Herckes, P.; Westerhoff, P., Nanoparticle Size Detection Limits by Single Particle ICP-MS for 40 Elements. *Environ. Sci. Technol.* **2014,** *48* (17), 10291-10300.

67. Schwertfeger, D. M.; Velicogna, J. R.; Jesmer, A. H.; Saatcioglu, S.; McShane, H.; Scroggins, R. P.; Princz, J. I., Extracting Metallic Nanoparticles from Soils for Quantitative Analysis: Method Development Using Engineered Silver Nanoparticles and SP-ICP-MS. *Anal. Chem.* **2017,** *89* (4), 2505-2513.

68. Mackevica, A.; Olsson, M. E.; Hansen, S. F., Quantitative Characterization of TiO_2 Nanoparticle Release from Textiles by Conventional and Single Particle ICP-MS. *J. Nanoparticle Res.* **2017,** *20* (1), 6.

69. Donovan, A. R.; Adams, C. D.; Ma, Y.; Stephan, C.; Eichholz, T.; Shi, H., Fate of Nanoparticles During Alum and Ferric Coagulation Monitored Using Single Particle ICP-MS. *Chemosphere* **2018,** *195*, 531-541.

70. Venkatesan, A. K.; Reed, R. B.; Lee, S.; Bi, X.; Hanigan, D.; Yang, Y.; Ranville, J. F.; Herckes, P.; Westerhoff, P., Detection and Sizing of Ti-Containing Particles in Recreational Waters Using Single Particle ICP-MS. *Bull. Environ. Contam. Toxicol.* **2017**.

71. Azodi, M.; Sultan, Y.; Ghoshal, S., Dissolution Behavior of Silver Nanoparticles and Formation of Secondary Silver Nanoparticles in Municipal Wastewater by Single-Particle ICP-MS. *Environ. Sci. Technol.* **2016,** *50* (24), 13318-13327.

72. Zhang, S.; Han, G.; Xing, Z.; Zhang, S.; Zhang, X., Multiplex DNA Assay Based on Nanoparticle Probes by Single Particle Inductively Coupled Plasma Mass Spectrometry. *Anal. Chem.* **2014,** *86* (7), 3541-3547.

73. Hu, S.; Liu, R.; Zhang, S.; Huang, Z.; Xing, Z.; Zhang, X., A new strategy for highly sensitive immunoassay based on single-particle mode detection by inductively coupled plasma mass spectrometry. *J. Am. Soc. Mass Spectr.* **2009,** *20* (6), 1096-1103.

74. Han, G.; Xing, Z.; Dong, Y.; Zhang, S.; Zhang, X., One-Step Homogeneous DNA Assay with Single-Nanoparticle Detection. *Angew. Chem. Int. Ed.* **2011,** *50* (15), 3462-3465.

75. Degueldre, C.; Favarger, P. Y.; Wold, S., Gold Colloid Analysis by Inductively Coupled Plasma-Mass Spectrometry in a Single Particle Mode. *Anal. Chim. Acta* **2006,** *555* (2), 263-268.

76. Jokar, M.; Correia, M.; Loeschner, K., Behavior of Silver Nanoparticles and Ions in Food Simulants and Low Fat Cow Milk Under Migration Conditions. *Food Control* **2018,** *89*, 77-85.

77. Peters, R. J. B.; Rivera, Z. H.; van Bemmel, G.; Marvin, H. J. P.; Weigel, S.; Bouwmeester, H., Development and Validation of Single Particle ICP-MS for Sizing and Quantitative Determination of Nano-Silver in Chicken Meat. *Anal Bioanal. Chem.* **2014,** *406* (16), 3875-3885.

78. Laborda, F.; Jiménez-Lamana, J.; Bolea, E.; Castillo, J. R., Critical Considerations for the Determination of Nanoparticle Number Concentrations, Size and Number Size Distributions by Single Particle ICP-MS. *J. Am. Soc. Mass Spectr.* **2013,** *28* (8), 1220-1232.

79. Mitrano, D. M.; Barber, A.; Bednar, A.; Westerhoff, P.; Higgins, C. P.; Ranville, J. F., Silver Nanoparticle Characterization Using Single Particle ICP-MS (SP-ICP-MS) and Asymmetrical Flow Field Flow Fractionation ICP-MS (AF4-ICP-MS). *J. Am. Soc. Mass Spectr.* **2012,** *27* (7), 1131-1142.

80. Montaño, M. D.; Badiei, H. R.; Bazargan, S.; Ranville, J. F., Improvements in the Detection and Characterization of Engineered Nanoparticles Using spICP-MS with Microsecond Dwell times. *Environ. Sci. Nano* **2014,** *1* (4), 338-346.

81. Kińska, K.; Jiménez-Lamana, J.; Kowalska, J.; Krasnodębska-Ostręga, B.; Szpunar, J., Study of the Uptake and Bioaccumulation of Palladium Nanoparticles by Sinapis Alba Using Single Particle ICP-MS. *Sci. Total Environ.* **2018,** *615*, 1078-1085.

82. Montoro Bustos, A. R.; Purushotham, K. P.; Possolo, A.; Farkas, N.; Vladár, A. E.; Murphy, K. E.; Winchester, M. R., Validation of Single Particle ICP-MS for Routine Measurements of Nanoparticle Size and Number Size Distribution. *Anal. Chem.* **2018,** *90* (24), 14376-14386.

83. Boyd;, R. D.; Cuenat;, A.; Meli;, F.; Klein;, T.; Frase;, C. G.; Gleber;, G.; Krumrey;, M.; Duta;, A.; Duta;, S.; Hogstrom;, R.; Prieto;, E., Good Practice Guide No. 119: Good Practice Guide for the Determination of the Size and Size Distribution of Spherical Nanoparticle samples. Laboratory, N. P., Ed. 2011.

84.Safety, R. I. O. F., Nanopaticle Suspensions-Counting and Sizing Nanoparticles via Sizing Particle Inductively Coupled Plasma Mass Spectrometetry. 2013.

85. Begley, I. S.; Sharp, B. L., Occurrence and Reduction of Noise in Inductively Coupled Plasma Mass Spectrometry for Enhanced Precision in Isotope Ratio Measurement. *J. Am. Soc. Mass Spectr.* **1994,** *9* (3), 171-176.

86. Yin, S. H.; Yang, J.; Han, Y.; Li, G.; Wan, L. Y.; Chen, Y. H.; Chen, C.; Qu, X. M.; Jiang, Y. X.; Sun, S. G., Construction of Highly Active Metal-Containing Nanoparticles and FeCo-N4 Composite Sites for the Acidic Oxygen Reduction Reaction. *Angew. Chem.* **2020,** *132* (49), 22160-22163.

87. Feng, Y.; Chen, X.; Wang, H.; Li, X.; Huang, H.; Liu, Y.; Li, H., Durable and High Performing Ti Supported Ni0.4Cu0.6Co2O4 Nanoleaf-Like Array Catalysts for Hydrogen Production. *Renew. Energy* **2021,** *169*, 660-669.

88. Gupta, L. K.; Kumar, K.; Yadav, B. C.; Yadav, T. P.; Dzhardimalieva, G. I.; Uflyand, I. E.; Shripal, Comparative Study on Humidity Sensing Abilities of Synthesized Mono and Poly Rhodium Acryl Amide Tin Oxide (RhAAm/SnO2) nanocomposites. *Sens. Actuators A* **2021,** *330*, 112839.

89. Wu, J.; Tou, F.; Yang, Y.; Liu, C.; Hower, J. C.; Baalousha, M.; Wang, G.; Liu, M.; Hochella, M. F., Metal-Containing Nanoparticles in Low-Rank Coal-Derived Fly Ash from China: Characterization and Implications toward Human Lung Toxicity. *Environ. Sci. Technol.* **2021,** *55* (10), 6644-6654.

90. Gallego-Urrea, J. A.; Tuoriniemi, J.; Hassellöv, M., Applications of particle-tracking analysis to the determination of size distributions and concentrations of nanoparticles in

environmental, biological and food samples. *TrAC Trends Anal. Chem.* **2011,** *30* (3), 473-483.

91. Howard, A. G., On the Challenge of Quantifying Man-Made Nanoparticles in the Aquatic Environment. *J. Environ. Monit.* **2010,** *12* (1), 135-142.

92. Liu, J.; Murphy, K. E.; MacCuspie, R. I.; Winchester, M. R., Capabilities of Single Particle Inductively Coupled Plasma Mass Spectrometry for the Size Measurement of Nanoparticles: A Case Study on Gold Nanoparticles. *Anal. Chem.* **2014,** *86* (7), 3405-3414.

93. Álvarez-Fernández García, R.; Fernández-Iglesias, N.; López-Chaves, C.; Sánchez-González, C.; Llopis, J.; Montes-Bayón, M.; Bettmer, J., Complementary Techniques (spICP-MS, TEM, and HPLC-ICP-MS) Reveal the Degradation of 40 nm Citrate-Stabilized Au Nanoparticles in Rat Liver After Intraperitoneal Injection. *J. Trace Elem. Med. Biol.* **2019,** *55*, 1-5.

94. Geertsen, V.; Barruet, E.; Gobeaux, F.; Lacour, J.-L.; Taché, O., Contribution to Accurate Spherical Gold Nanoparticle Size Determination by Single-Particle Inductively Coupled Mass Spectrometry: A Comparison with Small-Angle X-ray Scattering. *Anal. Chem.* **2018,** *90* (16), 9742-9750.

95. Minelli, C.; Bartczak, D.; Peters, R.; Rissler, J.; Undas, A.; Sikora, A.; Sjöström, E.; Goenaga-Infante, H.; Shard, A. G., Sticky Measurement Problem: Number Concentration of Agglomerated Nanoparticles. *Langmuir* **2019,** *35* (14), 4927-4935.

96. Tadjiki, S.; Montaño, M. D.; Assemi, S.; Barber, A.; Ranville, J.; Beckett, R., Measurement of the Density of Engineered Silver Nanoparticles Using Centrifugal FFF-TEM and Single Particle ICP-MS. *Anal. Chem.* **2017,** *89* (11), 6056-6064.

97. Xing, Y.; Han, J.; Wu, X.; Pierce, D. T.; Zhao, J. X., Aggregation-Based Determination of Mercury(II) Using DNA-Modified Single Gold Nanoparticle, T-Hg(II)-T Interaction, and Single-Particle ICP-MS. *Microchim. Acta* **2019,** *187* (1), 56.

98. Rua-Ibarz, A.; Bolea-Fernandez, E.; Pozo, G.; Dominguez-Benetton, X.; Vanhaecke, F.; Tirez, K., Characterization of Iron Oxide Nanoparticles by Means of Single-Particle ICP-mass Spectrometry (SP-ICP-MS) – Chemical Versus Physical Resolution to Overcome Spectral Overlap. *J. Am. Soc. Mass Spectr.* **2020,** *35* (9), 2023-2032.

99. Bocca, B.; Battistini, B.; Petrucci, F., Silver and Gold Nanoparticles Characterization by SP-ICP-MS and AF4-FFF-MALS-UV-ICP-MS in Human Samples Used for Biomonitoring. *Talanta* **2020,** *220*, 121404.

100. Mestek, O.; Loula, M.; Kaňa, A.; Vosmanská, M., Can ultrafast single-particle analysis using ICP-MS affect the detection limit? Case study: Silver nanoparticles. *Talanta* **2020,** *210*, 120665.

101. Loula, M.; Kaňa, A.; Koplík, R.; Hanuš, J.; Vosmanská, M.; Mestek, O., Analysis of Silver Nanoparticles Using Single-Particle Inductively Coupled Plasma – Mass Spectrometry (ICP-MS): Parameters Affecting the Quality of Results. *Anal. Lett.* **2019,** *52* (2), 288-307.

102. Liu, X.; Han, J.; Wu, X.; Pierce, D.; Zhao, J. X., Eu-Coordinated Semiconducting Polymer Nanoparticles as a Novel Nanoprobe with Two Detection Method Signals for Determination of Copper(II) Ions. *Sensors and Actuators B* **2021,** *344*, 130194.

103. Mansor, M.; Drabesch, S.; Bayer, T.; Van Le, A.; Chauhan, A.; Schmidtmann, J.; Peiffer, S.; Kappler, A., Application of Single-Particle ICP-MS to Determine the Mass Distribution and Number Concentrations of Environmental Nanoparticles and Colloids. *Environ. Sci. Technol. Lett.* **2021**.

104. Bagwe, R. P.; Yang, C.; Hilliard, L. R.; Tan, W., Optimization of Dye-Doped Silica Nanoparticles Prepared Using a Reverse Microemulsion Method. *Langmuir* **2004,** *20* (19), 8336-8342.

105. Bray, D. J.; Dittanet, P.; Guild, F. J.; Kinloch, A. J.; Masania, K.; Pearson, R. A.; Taylor, A. C., The Modelling of the Toughening of Epoxy Polymers via Silica Nanoparticles: The Effects of Volume Fraction and Particle Size. *Polymer* **2013,** *54* (26), 7022-7032.

106. Zhao, X.; Tapec-Dytioco, R.; Tan, W., Ultrasensitive DNA Detection Using Highly Fluorescent Bioconjugated Nanoparticles. *J. Am. Chem. Soc.* **2003,** *125* (38), 11474-11475.

107. Bagwe, R. P.; Hilliard, L. R.; Tan, W., Surface Modification of Silica Nanoparticles to Reduce Aggregation and Nonspecific Binding. *Langmuir* **2006,** *22* (9), 4357-4362.

108. Jin, Y.; Lohstreter, S.; Pierce, D. T.; Parisien, J.; Wu, M.; Hall, C.; Zhao, J. X., Silica Nanoparticles with Continuously Tunable Sizes: Synthesis and Size Effects on Cellular Contrast Imaging. *Chem. Mater.* **2008,** *20* (13), 4411-4419.

109. Jin, Y.; Kannan, S.; Wu, M.; Zhao, J. X., Toxicity of Luminescent Silica Nanoparticles to Living Cells. *Chem. Res. in Toxicol.* **2007,** *20* (8), 1126-1133.

110. Hunter, T. F., The Distribution of Solubilisate Molecules in Micellar Assemblies. *Chem. Phys. Lett.* **1980,** *75* (1), 152-155.

111. Jin, R.; Qian, H.; Wu, Z.; Zhu, Y.; Zhu, M.; Mohanty, A.; Garg, N., Size Focusing: A Methodology for Synthesizing Atomically Precise Gold Nanoclusters. *J. Phys. Chem. Lett.* **2010,** *1* (19), 2903-2910.

112. Qian, H.; Zhu, M.; Wu, Z.; Jin, R., Quantum Sized Gold Nanoclusters with Atomic Precision. *Acc. Chem. Res.* **2012,** *45* (9), 1470-1479.

113. Pramanik, G.; Humpolickova, J.; Valenta, J.; Kundu, P.; Bals, S.; Bour, P.; Dracinsky, M.; Cigler, P., Gold Nanoclusters with Bright Near-infrared Photoluminescence. *Nanoscale* **2018,** *10* (8), 3792-3798.

114. Yangzhouyun, X.; Yong, L.; Junchuan, Y.; Yuan, L.; Fupin, H.; Kui, Z.; Xingyu, J., Gold Nanoclusters for Targeting Methicillin-Resistant Staphylococcus Aureus In Vivo. *Angew. Chem. Int. Ed.* **2018,** *57* (15), 3958-3962.

115. Nath, P.; Chatterjee, M.; Chanda, N., Dithiothreitol-Facilitated Synthesis of Bovine Serum Albumin–Gold Nanoclusters for Pb(II) Ion Detection on Paper Substrates and in Live Cells. *ACS Appl. Nano Mater.* **2018,** *1* (9), 5108-5118.

116. Huang, Y.; Gao, L.; Cui, H., Assembly of Multifunctionalized Gold Nanoparticles with Chemiluminescent, Catalytic, and Immune Activity for Label-Free Immunoassays. *ACS Appl. Mater. Interfaces* **2018,** *10* (20), 17040-17046.

117. Feng, W.; Wee Beng, T.; Yong, Z.; Xianping, F.; Minquan, W., Luminescent Nanomaterials for Biological Labelling. *Nanotechnology* **2006,** *17* (1), R1.

118. Luo, M.; Di, J.; Li, L.; Tu, Y.; Yan, J., Copper Ion Detection With Improved Sensitivity Through Catalytic Quenching of Gold Nanocluster Fluorescence. *Talanta* **2018,** *187*, 231-236.

119. Chen, Y.; Li, W.; Wang, Y.; Yang, X.; Chen, J.; Jiang, Y.; Yu, C.; Lin, Q., Cysteine-directed Fluorescent Gold Nanoclusters for the Sensing of Pyrophosphate and Alkaline Phosphatase. *J. Mater. Chem. C* **2014,** *2* (20), 4080-4085.

120. Cui, M.-L.; Liu, J.-M.; Wang, X.-X.; Lin, L. P.; Jiao, L.; Zhang, L.-H.; Zheng, Z.-Y.; Lin, S.-Q., Selective Determination of Cysteine Using BSA-stabilized Gold Nanoclusters with Red Emission. *Analyst* **2012,** *137* (22), 5346-5351.

121. Couleaud, P.; Adan-Bermudez, S.; Aires, A.; Mejías, S. H.; Sot, B.; Somoza, A.; Cortajarena, A. L., Designed Modular Proteins as Scaffolds To Stabilize Fluorescent Nanoclusters. *Biomacromolecules* **2015,** *16* (12), 3836-3844.

122. Sun, J.; Yue, Y.; Wang, P.; He, H.; Jin, Y., Facile and Rapid Synthesis of Water-Soluble Fluorescent Gold Nanoclusters for Sensitive and Selective Detection of Ag^{+}. *J. Mater. Chem. C* **2013,** *1* (5), 908-913.

123. Kim, H. N.; Ren, W. X.; Kim, J. S.; Yoon, J., Fluorescent and Colorimetric Sensors for Detection of Lead, Cadmium, and Mercury Ions. *Chem. Soc. Rev.* **2012,** *41* (8), 3210-3244.

124. Chen, X.; Zhou, Y.; Peng, X.; Yoon, J., Fluorescent and Colorimetric Probes for Detection of Thiols. *Chem. Soc. Rev.* **2010,** *39* (6), 2120-2135.

125. Yu, L.; Zhang, L.; Ren, G.; Li, S.; Zhu, B.; Chai, F.; Qu, F.; Wang, C.; Su, Z., Multicolorful Fluorescent-nanoprobe Composed of Au Nanocluster and Carbon Dots for Colorimetric and Fluorescent Sensing Hg^{2+} and Cr^{6+}. *Sensor and Actuators B* **2018,** *262*, 678-686.

126. Yu, X.; Zhang, C.-X.; Zhang, L.; Xue, Y. R.; Li, H.-W.; Wu, Y., The Construction of a FRET Assembly by Using Gold Nanoclusters and Carbon Dots and Their Application as a Ratiometric Probe for Cysteine Detection. *Sensor and Actuators B* **2018,** *263*, 327-335.

127.Wang, L.L.; Qiao, J.; Liu, H. H.; Hao, J.; Qi, L.; Zhou, X. P.; Li, D.; Nie, Z. X.; Mao, L.-Q., Ratiometric Fluorescent Probe Based on Gold Nanoclusters and Alizarin Red-Boronic Acid for Monitoring Glucose in Brain Microdialysate. *Anal. Chem.* **2014,** *86* (19), 9758-9764.

128. Wu, C.; Peng, H.; Jiang, Y.; McNeill, J., Energy Transfer Mediated Fluorescence from Blended Conjugated Polymer Nanoparticles. *J. Phys. Chem. B.* **2006,** *110* (29), 14148-14154.

129. Koralli, P.; D. Nega, A.; Vagiaki, L. E.; Pavlou, A.; Siskos, M. G.; Dimitrakopoulou-Strauss, A.; Gregoriou, V. G.; Chochos, C. L., New Conjugated Polymer Nanoparticles with High Photoluminescence Quantum Yields for Far-red and Near Infrared Fluorescence Bioimaging. *Mater. Chem. Front.* **2020,** *4* (8), 2357-2369.

130. Wang, Q. B.; Zhang, C. J.; Yu, H.; Zhang, X.; Lu, Q.; Yao, J. S.; Zhao, H., The sensitive "Turn-on" Fluorescence Platform of Ascorbic Acid Based on Conjugated Polymer Nanoparticles. *Anal. Chim. Acta* **2020,** *1097*, 153-160.

131. Feng, L.; Zhu, C.; Yuan, H.; Liu, L.; Lv, F.; Wang, S., Conjugated Polymer Nanoparticles: Preparation, Properties, Functionalization and Biological Applications. *Chem. Soc. Rev.* **2013,** *42* (16), 6620-6633.

132. Karstens, T.; Kobs, K., Rhodamine B and Rhodamine 101 as Reference Substances for Fluorescence Quantum Yield Measurements. *J. Phys. Chem. A* **1980,** *84* (14), 1871-1872.

133. Luo, Z.; Yuan, X.; Yu, Y.; Zhang, Q.; Leong, D. T.; Lee, J. Y.; Xie, J., From Aggregation-Induced Emission of Au(I)–Thiolate Complexes to Ultrabright Au(0)@Au(I)–Thiolate Core–Shell Nanoclusters. *J. Am. Chem. Soc.* **2012,** *134* (40), 16662-16670.

134. Wang, L.; Cao, H. X.; He, Y. S.; Pan, C. G.; Sun, T. K.; Zhang, X. Y.; Wang, C. Y.; Liang, G. X., Facile Preparation of Amino-carbon Dots/gold Nanoclusters FRET Ratiometric Fluorescent Probe for Sensing of Pb^{2+}/Cu^{2+}. *Sensor and Actuators B* **2019,** *282*, 78-84.

135. Wu, C.; Bull, B.; Szymanski, C.; Christensen, K.; McNeill, J., Multicolor Conjugated Polymer Dots for Biological Fluorescence Imaging. *ACS Nano* **2008,** *2* (11), 2415-2423.

136. Zheng, C. L.; Ji, Z. X.; Zhang, J.; Ding, S. N., A Fluorescent Sensor to Detect Sodium Dodecyl Sulfate Based on the Glutathione-stabilized Gold Nanoclusters/poly Diallyldimethylammonium Chloride System. *Analyst* **2014,** *139* (13), 3476-3480.

137. Bhunia, S.; Kumar, S.; Purkayastha, P., Gold Nanocluster-Grafted Cyclodextrin Suprastructures: Formation of Nanospheres to Nanocubes with Intriguing Photophysics. *ACS Omega* **2018,** *3* (2), 1492-1497.

138. Bulcke, F.; Dringen, R.; Scheiber, I. F., Neurotoxicity of Copper. In *Neurotoxicity of Metals*, Aschner, M.; Costa, L. G., Eds. Springer International Publishing: Cham, 2017; pp 313-343.

139. Navarro, J. A.; Schneuwly, S., Copper and Zinc Homeostasis: Lessons from Drosophila Melanogaster. *Front. Genet.* **2017,** *8* (223).

140. Nasulewicz, A.; Mazur, A.; Opolski, A., Role of Copper in Tumour Angiogenesis—Clinical Implications. *J. Trace Elem Med. Biol.* **2004,** *18* (1), 1-8.

141. Strausak, D.; Mercer, J. F. B.; Dieter, H. H.; Stremmel, W.; Multhaup, G., Copper in Disorders with Neurological Symptoms: Alzheimer's, Menkes, and Wilson Diseases. *Brain Res. Bull.* **2001,** *55* (2), 175-185.

142. Lee, S.; Barin, G.; Ackerman, C. M.; Muchenditsi, A.; Xu, J.; Reimer, J. A.; Lutsenko, S.; Long, J. R.; Chang, C. J., Copper Capture in a Thioether-Functionalized Porous Polymer Applied to the Detection of Wilson's Disease. *J. Am. Chem. Soc.* **2016,** *138* (24), 7603-7609.

143. Ding, Y.; Shen, S. Z.; Sun, H.; Sun, K.; Liu, F., Synthesis of l-glutathione-capped-ZnSe Quantum Dots for the Sensitive and Selective Determination of Copper Ion in Aqueous Solutions. *Sens. Actuators B Chem.* **2014,** *203*, 35-43.

144. Becker, J. S.; Matusch, A.; Depboylu, C.; Dobrowolska, J.; Zoriy, M. V., Quantitative Imaging of Selenium, Copper, and Zinc in Thin Sections of Biological Tissues (Slugs−Genus Arion) Measured by Laser Ablation Inductively Coupled Plasma Mass Spectrometry. *Anal. Chem.* **2007,** *79* (16), 6074-6080.

145. Dobrowolska, J.; Dehnhardt, M.; Matusch, A.; Zoriy, M.; Palomero-Gallagher, N.; Koscielniak, P.; Zilles, K.; Becker, J. S., Quantitative Imaging of Zinc, Copper and Lead in Three Distinct Regions of the Human Brain by Laser Ablation Inductively Coupled Plasma Mass Spectrometry. *Talanta* **2008,** *74* (4), 717-723.

146. Zhang, W.; Fan, S.; Li, X.; Liu, S.; Duan, D.; Leng, L.; Cui, C.; Zhang, Y.; Qu, L., Electrochemical Determination of Lead(II) and Copper(II) by Using Phytic Acid and Polypyrrole Functionalized Metal-organic Frameworks. *Microchim. Acta* **2019,** *187* (1), 69.

147. Kaur, I.; Sharma, M.; Kaur, S.; Kaur, A., Ultra-sensitive Electrochemical Sensors Based on Self-assembled Chelating Dithiol on Gold Electrode for Trace Level Detection of Copper(II) ions. *Sen. Actuators B Chem.* **2020,** *312*, 127935.

148. Zhang, G.; Li, Y.; Xu, J.; Zhang, C.; Shuang, S.; Dong, C.; Choi, M. M. F., Glutathione-protected Fluorescent Gold Nanoclusters for Sensitive and Selective Detection of Cu^{2+}. *Sens. Actuators B Chem.* **2013,** *183*, 583-588.
149. Liu, X.; Han, J.; Hou, X.; Altincicek, F.; Oncel, N.; Pierce, D.; Wu, X.; Zhao, J. X., One-pot Synthesis of Graphene Quantum Dots Using Humic Acid and its Application for Copper (II) Ion Detection. *J. Mater. Sci.* **2021,** *56* (8), 4991-5005.

150. Li, B. R.; Tang, H.; Yu, R. Q.; Jiang, J. H., Single-Nanoparticle ICPMS DNA Assay Based on Hybridization-Chain-Reaction-Mediated Spherical Nucleic Acid Assembly. *Anal. Chem.* **2020,** *92* (3), 2379-2382.

151. Atkins, P.; Overton, T., *Shriver and Atkins' Inorganic Chemistry*. Oxford University Press, USA: 2010.

152. Zheng, Y.; Lai, L.; Liu, W.; Jiang, H.; Wang, X., Recent Advances in Biomedical Applications of Fluorescent Gold Nanoclusters. *Adv. Colloid Interface Sci.* **2017,** *242*, 1-16.

153. Zhu, S.; Wang, X.; Cong, Y.; Li, L., Regulating the Optical Properties of Gold Nanoclusters for Biological Applications. *ACS Omega* **2020,** *5* (36), 22702-22707.

154. Jiang, J.; Conroy, C. V.; Kvetny, M. M.; Lake, G. J.; Padelford, J. W.; Ahuja, T.; Wang, G., Oxidation at the Core–Ligand Interface of Au Lipoic Acid Nanoclusters That Enhances the Near-IR Luminescence. *J. Phys. Chem. C* **2014,** *118* (35), 20680-20687.

155. Das, A.; Li, T.; Li, G.; Nobusada, K.; Zeng, C.; Rosi, N. L.; Jin, R., Crystal Structure and Electronic Properties of a Thiolate-protected Au24 Nanocluster. *Nanoscale* **2014,** *6* (12), 6458-6462.

156. Wu, Z.; Jin, R., On the Ligand's Role in the Fluorescence of Gold Nanoclusters. *Nano Letters* **2010,** *10* (7), 2568-2573.

157. Wang, S.; Meng, X.; Das, A.; Li, T.; Song, Y.; Cao, T.; Zhu, X.; Zhu, M.; Jin, R., A 200-fold Quantum Yield Boost in the Photoluminescence of Silver-Doped AgxAu25−x Nanoclusters: The 13 th Silver Atom Matters. *Angew. Chem. Int. Ed.* **2014,** *53* (9), 2376-2380.

158. Deng, H. H.; Peng, H.-P.; Huang, K. Y.; He, S. B.; Yuan, Q. F.; Lin, Z.; Chen, R. T.; Xia, X. H.; Chen, W., Self-Referenced Ratiometric Detection of Sulfatase Activity with Dual-Emissive Urease-Encapsulated Gold Nanoclusters. *ACS Sensors* **2019,** *4* (2), 344-352.

159. Wang, P.; Yuan, L. T.; Huang, X.; Chen, W. J.; Jia, K.; Liu, X. B., Tuning of Polyarylene Ether Nitrile Emission Profile by Using Red-emitting Gold Nanoclusters via Fluorescence Resonance Energy Transfer. *RSC Advances* **2014,** *4* (87), 46541-46544.

160. Bhunia, S.; Gangopadhyay, K.; Ghosh, A.; Seth, S. K.; Das, R.; Purkayastha, P., Arginine-Modified Fluorescent Gold Nanoclusters for Förster Resonance Energy Transfer with a Hemicyanine Dye: A Biofriendly Approach. *ACS Appl. Nano Mater.* **2021,** *4* (1), 305-312.

161. He, Y. S.; Pan, C. G.; Cao, H. X.; Yue, M. Z.; Wang, L.; Liang, G. X., Highly Sensitive and Selective Dual-emission Ratiometric Fluorescence Detection of Dopamine Based on Carbon Dots-gold Nanoclusters Hybrid. *Sens. Actuators B Chem.* **2018,** *265*, 371-377.

162. Dong, W.; Wang, R.; Gong, X.; Dong, C., An Efficient Turn-on Fluorescence Biosensor for the Detection of Glutathione Based on FRET Between N,S Dual-doped Carbon Dots and Gold Nanoparticles. *Anal. Bioanal. Chem.* **2019,** *411* (25), 6687-6695.

163. Bhandari, S.; Pramanik, S.; Khandelia, R.; Chattopadhyay, A., Gold Nanocluster and Quantum Dot Complex in Protein for Biofriendly White-Light-Emitting Material. *ACS Appl. Mater. Interfaces* **2016,** *8* (3), 1600-1605.

164. Aldeek, F.; Ji, X.; Mattoussi, H., Quenching of Quantum Dot Emission by Fluorescent Gold Clusters: What It Does and Does Not Share with the Förster Formalism. *J. Phys. Chem. C* . **2013,** *117* (29), 15429-15437.

165. Himaja, A. L.; Karthik, P. S.; Singh, S. P., Carbon Dots: The Newest Member of the Carbon Nanomaterials Family. *Chem. Rec.* **2015,** *15* (3), 595-615.

166. Ye, L.; Hu, R.; Liu, L.; Liu, J.; Liu, J.; Chen, H.; Hu, Y.; Liu, Y.; Liu, X.; Liu, C.; Tng, D. J. H.; Meng, Y.; Qu, J.; Swihart, M. T.; Yong, K.-T., Comparing Semiconductor Nanocrystal Toxicity in Pregnant Mice and Non-Human Primates. *Nanotheranostics* **2019,** *3* (1), 54-65.

167. Khoshkam, M.; Baghdadchi, Y.; Arezumand, R.; Ramazani, A., Synthesis, Characterization and in Vivo Evaluation of Cadmium Telluride Quantum Dots Toxicity in Mice by Toxicometabolomics Approach. *Toxicol. Mech. Methods* **2018,** *28* (7), 539-546.

168. Zhou, X.; Zeng, Y.; Tang, Y.; Huang, Y.; Lv, F.; Liu, L.; Wang, S., Artificial Regulation of State Transition for Augmenting Plant Photosynthesis Using Synthetic Light-harvesting Polymer Materials. *Sci. Adv.* **2020,** *6* (35), eabc5237.

169. Sarkar, S.; Levi-Polyachenko, N., Conjugated Polymer Nano-systems for Hyperthermia, Imaging and Drug Delivery. *Adv. Drug Deliv. Rev.* **2020,** *163-164*, 40-64.

170. Xu, Y.; Zhai, X.; Su, P.; Liu, T.; Zhou, L.; Zhang, J.; Bao, B.; Wang, L., Highly Stable Semiconducting Polymer Nanoparticles for Multi-responsive Chemo/photothermal Combined Cancer Therapy. *Theranostics* **2020,** *10* (13), 5966-5978.

171. Liu, J.; Cai, X.; Pan, H.-C.; Bandla, A.; Chuan, C. K.; Wang, S.; Thakor, N.; Liao, L.-D.; Liu, B., Molecular Engineering of Photoacoustic Performance by Chalcogenide Variation in Conjugated Polymer Nanoparticles for Brain Vascular Imaging. *Small* **2018,** *14* (13), 1703732.

172. Jiang, Y.; McNeill, J., Light-Harvesting and Amplified Energy Transfer in Conjugated Polymer Nanoparticles. *Chem. Rev.* **2017,** *117* (2), 838-859.

173. Miller, W. L.; Auchus, R. J., The Molecular Biology, Biochemistry, and Physiology of Human Steroidogenesis and Its Disorders. *Endocr. Rev.* **2011,** *32* (1), 81-151.

174. Van Meurs, J. B. J.; Dhonukshe-Rutten, R. A. M.; Pluijm, S. M. F.; van der Klift, M.; de Jonge, R.; Lindemans, J.; de Groot, L. C. P. G. M.; Hofman, A.; Witteman, J. C. M.; van Leeuwen, J. P. T. M.; Breteler, M. M. B.; Lips, P.; Pols, H. A. P.; Uitterlinden, A. G., Homocysteine Levels and the Risk of Osteoporotic Fracture. *N. Engl. J. Med.* **2004,** *350* (20), 2033-2041.

175. Goodman, M. T.; McDuffie, K.; Hernandez, B.; Wilkens, L. R.; Selhub, J., Case-control Study of Plasma Folate, Homocysteine, Vitamin B12, and Cysteine as Markers of Cervical Dysplasia. *Cancer* **2000,** *89* (2), 376-382.

176. Niu, Y.; Ding, T.; Liu, J.; Zhang, G.; Tong, L.; Cheng, X.; Yang, Y.; Chen, Z.; Tang, B., Fluorescence Switch of Gold Nanoclusters Stabilized with Bovine Serum Albumin for Efficient and Sensitive Detection of Cysteine and Copper Ion in Mice with Alzheimer's Disease. *Talanta* **2021,** *223*, 121745.

177. Bamdad, F.; Khorram, F.; Samet, M.; Bamdad, K.; Sangi, M. R.; Allahbakhshi, F., Spectrophotometric Determination of l-cysteine by Using Polyvinylpyrrolidone-Stabilized Silver Nanoparticles in the Presence of Barium Ions. *Spectrochim. Acta A* **2016,** *161*, 52-57.

178. Bayle, C.; Caussé, E.; Couderc, F., Determination of Aminothiols in Body Fluids, Cells, and Tissues by Capillary Electrophoresis. *Electrophoresis* **2004,** *25* (10-11), 1457-1472.

179. Vladislavić, N.; Rončević, I. Š.; Buzuk, M.; Buljac, M.; Drventić, I., Electrochemical/chemical Synthesis of Hydroxyapatite on Glassy Carbon Electrode for Electroanalytical Determination of Cysteine. *J. Solid State Chem.* **2021,** *25* (3), 841-857.

180. Xu, N.; Yuan, Y.; Lan, C.; Wei, W.; Meng, L.; Fan, L., A Novel Dual-emission Fluorescent Nanohybrid Containing Silica Nanoparticles and Gold Nanoclusters for

Ratiometric Determination of Cysteine Based on Turn-on Fluorescence Strategy. *New J Chem.* **2018,** *42* (12), 10092-10099.

181. Yang, Y.; Xing, X.; Zou, T.; Wang, Z.; Zhao, R.; Hong, P.; Peng, S.; Zhang, X.; Wang, Y., A Novel and Sensitive Ratiometric Fluorescence Assay for Carbendazim Based on N-doped Carbon Quantum Dots and Gold Nanocluster Nanohybrid. *J. Hazard. Mater.* **2020,** *386*, 121958.

182. Wang, J.; Lin, X.; Su, L.; Yin, J.; Shu, T.; Zhang, X., Chemical Etching of pH-Sensitive Aggregation-induced Emission-active Gold Nanoclusters for Ultra-sensitive Detection of Cysteine. *Nanoscale* **2019,** *11* (1), 294-300.

183. Yahia-Ammar, A.; Sierra, D.; Mérola, F.; Hildebrandt, N.; Le Guével, X., Self-Assembled Gold Nanoclusters for Bright Fluorescence Imaging and Enhanced Drug Delivery. *ACS Nano* **2016,** *10* (2), 2591-2599.

184. Medintz, I. L.; Hildebrandt, N., *FRET-Förster Resonance Energy Transfer: from Theory to Applications*. John Wiley & Sons: 2013.

185. Zhang, Y.; Xu, H.; Chen, Y.; You, X.; Pu, Y.; Xu, W.; Liao, X., High-sensitivity Detection of Cysteine and Glutathione Using Au Nanoclusters Based on Aggregation-induced Emission. *J. Fluoresc.* **2020,** *30* (6), 1491-1498.

186. Feng, T.; Chen, Y.; Feng, B.; Yan, J.; Di, J., Fluorescence Red-shift of Gold-Silver Nanoclusters upon Interaction with Cysteine and its Application. *Spectrochim. Acta A* **2019,** *206*, 97-103.

187. Li, J. J.; Qiao, D.; Yang, S. Z.; Weng, G. J.; Zhu, J.; Zhao, J. W., Colorimetric Determination of Cysteine Based on Inhibition of GSH-Au/Pt NCs as Peroxidase Mimic. *Spectrochim. Acta A* **2021,** *248*, 119257.